Fast optical *in situ* spectroscopy in III-V MOVPE

vorgelegt von
Diplom-Physiker
Christian Kaspari
aus Berlin

Von der Fakultät II – Mathematik und Naturwissenschaften
der Technischen Universität Berlin

zur Erlangung des akademischen Grades
Doktor der Naturwissenschaften
Dr. rer. nat.

genehmigte Dissertation

Promotionsausschuss:

Vorsitzender:	Prof. Dr. Hans Joachim Eichler
Berichter:	Prof. Dr. Wolfgang Richter
Berichter:	Prof. Dr. Norbert Esser

Tag der wissenschaftlichen Aussprache: 23. März 2007

Berlin 2007

D 83

Contents

1. Introduction

The application of *in situ* monitoring tools has revolutionised our understanding of crystal growth and the structure of the growing surface. While the classical electron-based surface science techniques like e.g. LEED, RHEED and AES were available for decades for UHV-based growth, metal-organic vapour phase epitaxy (MOVPE), the "working horse" of device production, was for a long time a trial-and-error growth method that relied on *ex situ* analysis.

Optical *in situ* monitoring opened up a way to obtain information about the growing sample in gaseous (MOVPE) or even liquid (LPE) ambient, while still being applicable to UHV.

In this work, the focus lies on two linear optical *in situ* techniques and their application to III-V MOVPE: Reflectance Anisotropy Spectroscopy (RAS) and Spectroscopic Ellipsometry (SE). RAS is a very sensitive technique that delivers information about the state of the surface (reconstruction, termination, morphology) and the surface-near region (buried interfaces, doping). SE allows to determine layer thicknesses, chemical composition and surface morphology (roughness). While SE is still a method that is only used in research MOVPE machines, RAS can already be found in some production MOVPE systems.

Since RAS becomes more and more important, the limitations of "classical" RAS, where a monochromator is used for the scanning of the spectral range of interest, become more and more apparent. For fast and irreversible processes – like the self-organised formation of quantum dots – it is only possible to gain anisotropy information at a fixed wavelength, because a full spectral scan would take too much time (order of 10^2 s while 10^{-1} s temporal resolution is required). The spectral information – the whole picture – can only be measured for static conditions.

These limitations led to the idea of building a RAS setup that is capable of measuring spectra within fractions of a second. A large part of this work is concerned with the construction, testing and application of this special RAS setup, the so-called *multichannel* RAS.

Connected with the development of a multichannel RAS, this work is concerned with the application of (multichannel) RAS and SE to the growth and processing of binary III-V semiconductors (GaAs, InP, InAs and GaP). Key topics are the measurement of doping concentration with RAS and the study of thermal oxide desorption prior to growth with RAS and SE.

Special emphasis is put on the recently discovered phenomenon of thickness oscillations in RAS that can be observed during growth of doped layers.

This thesis can be outlined as follows: After revising briefly the basics of MOVPE growth, the optical *in situ* measurement techniques Spectroscopic Ellipsometry (SE) and Reflectance Anisotropy Spectroscopy (RAS) are explained in chapter 2. The details of RAS, its systematic errors and two procedures of calibration are described afterwards.

The following chapter 3 explains in detail the design and setup of the multichannel RAS. After the instrumentation the system is benchmarked with three different experiments against existing conventional RAS systems in chapter 4.

Chapter 5 is concerned with the question why the doping level of III-V semiconductors can be sensed by RAS and how this effect can be understood in the framework of the linear electro-optic effect (LEO). It also demonstrates how multichannel RAS can be used to determine the doping concentration.

The next chapter is closely connected to the one before because it describes an only recently found effect: the occurence of oscillations in the RAS signal during growth of doped layers. This effect can be exploited to determine the growth rate in homoepitaxy *in situ*, which is also very interesting from a technologist's point of view.

The last chapter contains a study about a very basic but in literature often neglected topic of semiconductor growth: the thermal deoxidation of the substrate material. This process is investigated *in situ* with SE and RAS.

2. Growth and in situ techniques

2.1 Metal organic vapour phase epitaxy

The *in situ* studies of this work were all performed in metal organic vapour phase epitaxy (MOVPE), also known as organo-metal vapour phase epitaxy (OMVPE) or metal organic chemical vapour deposition (MOCVD). Since MOVPE is a standard technique whose development started more than 40 years ago [1, 2], it will not be discussed in great detail. Good introductions to MOVPE can be found in [3, 4].

The MOVPE setup used in this work is a prototype of the Aixtron-200 research reactor. It is designed for the growth of III-V semiconductors. A schematic diagram is shown in figure 2.1. It is a horizontal reactor made of quartz glass, with a liner tube and a graphite susceptor (cold wall-type). The sample on the susceptor is heated by three

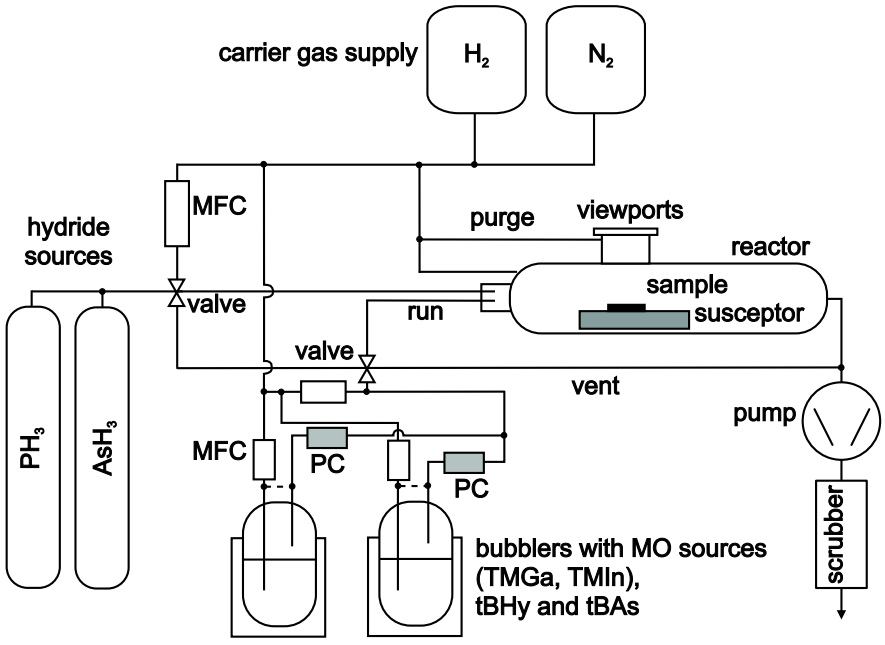

Figure 2.1: *Schematic diagram of the MOVPE system used in this work (picture courtesy of Kolja Haberland, [5]). The MOVPE growth technique allows a precise control of layer thickness (up to fractions of a monolayer), chemical composition and doping by means of a sophisticated arrangement of mass flow controllers (MFC) and pressure controllers (PC).*

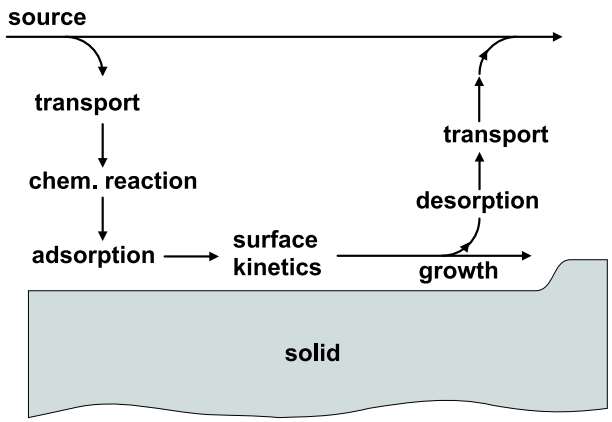

Figure 2.2: *Schematic description of the MOVPE growth process (after [6]).*

tungsten lamps from below. The temperature can reach ≈ 900°C and is controlled by a thermocouple.

The system runs at a total pressure of 100 mbar and a total gas flux of 3 ℓ/min. Possible carrier gases are H_2 and N_2. The carrier gas is necessary to transport the precursors to the sample and to remove the adducts.

Metal-organic precursors are trimethylgallium (TMGa), trimethylindium (TMIn), trimethylaluminium (TMAl) and triethylgallium (TEGa). The available hydrides are arsine (AsH_3), phosphine (PH_3) and silane (SiH_4, for doping). Alternative group V-precursors are tertiary butyl arsine (tBAs) and tertiary butyl hydrazine (tBHy). An dimethylzinc (DMZn) source is used for doping. If not stated otherwise, the standard values for the group V partial pressure were 100 Pa AsH_3 and 200 Pa PH_3.

The growth of a III-V-semiconductor is the result of a gross reaction like

$$\mathrm{III-R_3\ (g)\ +\ V-H_3\ (g)\ \longrightarrow\ III-V\ (s)\ +\ 3\,R-H\ (g),} \qquad (2.1)$$

where g stands for gaseous and s for solid. R represents metal organic rests (e.g. methyl, ethyl,...). The different mechanisms that take place during growth are shown schematically in figure 2.2.

Prior to growth, the oxide films present on the substrates must be removed thermally. This process is studied in detail in chapter 7. In some cases, the substrates need to be etched before being transferred to the growth reactor. The recipes for etching are given in appendix A.2.

The reactor is especially suitable for optical *in situ* studies because it is equipped with three low-strain optical quartz glass windows – two lateral ones for incidence at 65° (ellipsometry) and one above the sample for perpendicular incidence (RAS). The windows are purged with carrier gas to avoid contamination. The liner tube has 3 small cut-outs for the light paths. A detailed description of the MOVPE setup can be found in [7, 8].

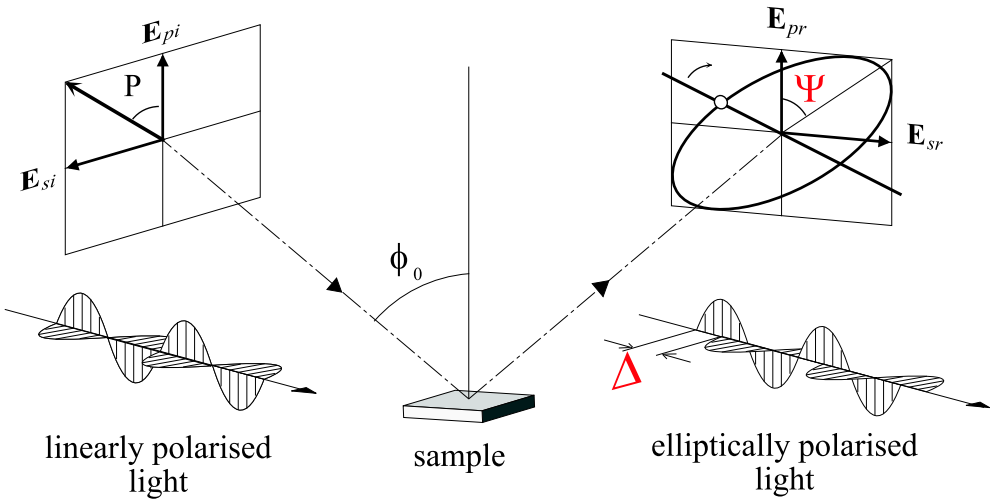

Figure 2.3: *Principle of ellipsometric measurements. Linearly polarised light is shone on a sample under an angle of incidence ϕ_0. The elliptically polarised reflected light is analysed in terms of the phase shift Δ and the tilt angle Ψ of the ellipse.*

2.2 Spectroscopic ellipsometry

Spectroscopic ellipsometry is used in this work to determine the thickness of oxide layers and the morphology of surfaces in chapter 7.

Ellipsometry is a non-invasive and non-destructive optical technique. It was developed from the middle of the 19th century on. A comprehensive textbook about ellipsometry can be found in [9].

Paul Drude was the first researcher to use ellipsometry. In 1889 he determined the optical constants of differently treated metal surfaces. The setup he used corresponds to that of a null ellipsometer. In this work, a rotating polariser ellipsometer (RPE) is used.

Ellipsometry measures the change of polarised light upon reflection at a sample surface (fig. 2.3). The angle of incidence ϕ_0 is chosen near the (quasi-) Brewster angle of the material ($\approx 65°$ for most semiconductors) to achieve a large difference between the reflection coefficients r_p and r_s for light polarised *parallel* and perpendicular (in German: *senkrecht*) to the plane of incidence.

The state of polarisation after reflection is analysed (e.g. by a rotating polarising prism) and the complex reflectance ratio

$$\rho = \frac{r_p}{r_s} = \tan\Psi e^{i\Delta} \tag{2.2}$$

can be determined. The quantities Ψ and Δ are called *ellipsometric angles*. In this work they are determined as a function of wavelength – hence the term Spectroscopic Ellipsometry (SE).

When the angle of incidence ϕ_0 and the complex reflectance ratio ρ are known, the effective dielectric function

$$\langle\epsilon\rangle = \sin^2\phi_0\left(1+\left(\frac{1-\rho}{1+\rho}\right)^2\tan^2\phi_0\right) \tag{2.3}$$

can be calculated. It is important to be aware that the effective dielectric function usually differs from the „material'' (bulk) dielectric function. Only when an atomically flat, semi-infinite and homogenious sample is measured in vacuum, $\langle\epsilon\rangle$ corresponds to the bulk dielectric function ϵ of the material. In all other cases (e.g. multilayer structures, surface roughness, inhomogenious materials) the dielectric function of the bulk or the layers must be determined by an optical modelling process.

This is done by assuming a certain multilayer structure of the sample and then reducing the problem iteratively following well-known multilayer algorithms [10]. The substrate and the adjacent two layers are reduced to a system consisting of only two layers. This process is repeated until one arrives at the three-phase model (ambient, one layer and the semi-infinite substrate). A detailed description can be found in [11, 12].

The angle of incidence has a big influence on the measured values of Ψ and Δ. An exact determination of ϕ_0 is therefore mandatory. Especially for *in situ* measurements, it is often not possible to determine this angle exactly by geometric methods. One has to choose a different approach: a well-known material (e.g. silicon with a thin oxide layer) is measured and the angle of incidence is fitted by comparison to calculated values from a database. The oxide layer thickness d_1 is also a fit parameter, but since the influence of d_1 and ϕ_0 on the ellipsometric angles is wavelength-dependent, an unambiguous determination is possible.

2.3 Reflectance anisotropy spectroscopy

Reflectance Anisotropopy Spectroscopy (RAS), sometimes also termed Reflectance Difference Spectroscopy (RDS), has its roots in ellipsometry. When the angle of incidence of an ellipsometer, usually being in the vicinity of the (quasi-) Brewster angle of the material, is changed from approx. 65° to normal incidence, it is no longer possible to distinguish between r_p and r_s, the components of the reflectivity *parallel* and perpendicular (*senkrecht*) to the plane of incidence. Instead, one measures the complex reflectivities r_x, r_y along two perpendicular directions on the surface.

While SE delivers information about the material and the layer structure, RAS measures the anisotropy of the sample. In fcc semiconductors, where the bulk is optically isotropic, anisotropic contributions are usually induced by interfaces (like the surface) where the symmetry of the bulk is broken. For this reason, RAS is very sensitive for the reconstruction of the surface. Together with electron diffraction techniques like RHEED, typical RAS spectra for different reconstructions can be recorded and later used for a purely optical determination (e.g. in MOVPE). In contrast to electron diffraction, RAS does not require a long-range order on the surface.

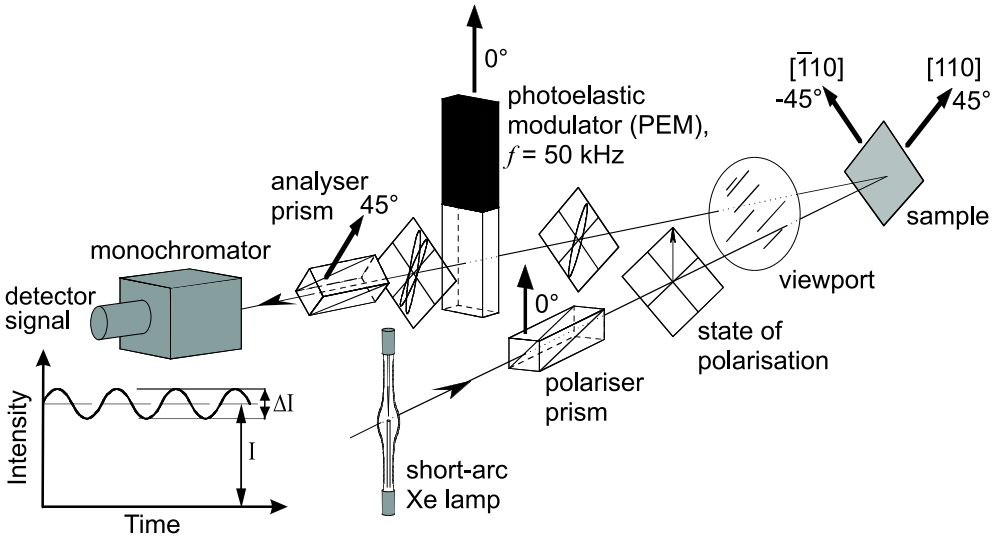

Figure 2.4: *Schematic RAS setup after [13, 14]. Linearly polarised light is shone on a sample under perpendicular incidence. The (elliptically polarised) reflected light runs through a photoelastic modulator (PEM) and a second polarising prism oriented at* 45°. *The modulated intensity is analysed by a combination of a monochromator and a detector. The angle of incidence is exaggerated (typically in the range of* $2-3°$*). The first RAS setups used a rotating sample (for the modulation) and only one polarising prism [15, 16]. Later, the sensitivity was refined by introducing a photoelastic modulator (PEM) and a second polarising prism.*

2.3.1 RAS fundamentals

The RAS signal of the (001) surface of an fcc semiconductor is defined as

$$\frac{\Delta r}{\langle r\rangle} = \frac{r_{[\bar{1}10]} - r_{[110]}}{\frac{1}{2}(r_{[\bar{1}10]} + r_{[110]})} = \mathrm{Re}\left(\frac{\Delta r}{\langle r\rangle}\right) + i\,\mathrm{Im}\left(\frac{\Delta r}{\langle r\rangle}\right) \tag{2.4}$$

where $\Delta r = r_{[\bar{1}10]} - r_{[110]}$ is the anisotropy in reflectance and $\langle r\rangle$ is the isotropic reflectance. A schematic setup is shown in fig. 2.4. Linearly polarised light hits the sample under perpendicular incidence. The reflected light is in general elliptically polarised, because the complex reflection coefficients along two perpendicular directions on the surface (here $r_{[\bar{1}10]}$ and $r_{[110]}$) can be different.

The reflected light runs through a photoelastic modulator (PEM), a device that introduces a periodically varying phase shift to one of the two polarisation components (cf. axis of the PEM). For reasons of detection, this phase modulation is transformed into an amplitude modulation by a second polarising prism oriented at 45°. The modulated intensity is analysed by a combination of a monochromator and a detector. A different approach concerning the detection unit is described in chapter 3.

The resulting signal consists of two components: a large DC component I representing the isotropic reflectance $\langle r\rangle$ and a very small AC component ΔI representing

the anisotropy. The ratio $\Delta I/I$ is typically in the order of 10^{-3} and is a measure for the RAS signal $\Delta r/\langle r\rangle$. The factor 10^{-3} in $\Delta r/\langle r\rangle$ is often called *RAS unit*. The exact calculation using the *Jones matrix formalism* [9] yields [13, 14]:

$$\begin{aligned}\frac{\Delta I}{I} = &\left(-\operatorname{Im}\left(\frac{\Delta r}{\langle r\rangle}\right) + \delta_1\cos 2\theta_1 + \delta_2\cos 2\theta_2 - 2\alpha_P\right) J_1(\delta_{\mathrm{PEM}})\sin\omega_{\mathrm{PEM}}t + \\ &+ 2\left(\operatorname{Re}\left(\frac{\Delta r}{\langle r\rangle}\right) + 2\Delta P + 2\Delta M\right) J_2(\delta_{\mathrm{PEM}})\cos 2\omega_{\mathrm{PEM}}t + \text{higher orders} \quad .\end{aligned} \tag{2.5}$$

The azimuths of polariser and PEM are $(-45° + \Delta P)$ and $(-45° + \Delta M)$, respectively. θ_1, θ_2 and δ_1, δ_2 are the azimuths of and the phase retardations induced by the strain of an optical window in front of the sample (subscript 1 for incident and subscript 2 for reflected light). The imperfection of the polariser is described by α_P. The two Bessel functions J_1, J_2 with the argument δ_{PEM} (the peak modulation of the PEM) have the function of correction factors and are due to the Fourier transform of the signal into frequency components. ω_{PEM} is the modulation frequency of the photoelastic modulator.

If we assume that azimuthal misalignments and window strain are negligible, (2.5) shows that the frequency component ω_{PEM} is proportional to the imaginary part and that the $2\omega_{\mathrm{PEM}}$-component is proportional to the real part of the RAS signal. Although there are higher orders present in the measured signal, it is usually sufficient to restrict oneself to the first two.

For the measurement, the measured signal $\Delta I/I$ is analysed by a lock-in amplifier. Depending on its setting (f or $2f$-mode), the imaginary or real part can be measured. For reasons of systematic errors (sec. 2.3.2) and ease of calibration (sec. 2.3.3) the real part is typically measured. The influence of imperfections of the optical components is stronger in the imaginary than in the real part.

Details of the RAS setup that is used in this work can be found in chapter 3.

2.3.2 Systematic errors

In the previous section in (2.5) a number of error sources is already included. This includes the imperfection of the polariser α_P which is determined by the degree of polarisation the polariser can achieve. Unpolarised or circularly polarised light will appear as additional influences in the RAS signal which cannot be removed easily. Errors of this category become noticeable when a polarising prism of Glan-Air type is used instead of a Rochon-type polariser.

The polariser offset ΔP shifts the baseline of the real part of the RAS signal. Usually the polariser is fixed in a rotary mount with a gear reduction for exact adjustment. Adjusting this polariser during measurement of an isotropic sample can be used to calibrate the setup for zero anisotropy. This property of ΔP can also be employed for calibration procedures (section 2.3.3).

In order to be able to measure *in situ*, in most cases the growth environment must be concealed against room atmosphere. This means that the RAS setup is located outside of the growth apparatus and the access to the sample is made via an optical window.

This optical window is an additional optical element in the light path and influences the measurement. It can absorb light (severe in the UV) and may induce additional

phase shifts through strain birefringence induced by its mount. In first order, the window strain does only influence the imaginary part (linear dependence) and not the real part of the RAS signal (2.5), but since the imaginary and real part are not independent from each other (Kramers-Kronig consistence), such window strain will influence the real part, too.

Using second-order error calculation it can be shown that the window strain appears as an additive correction Δ_{corr} in the real part and can be expressed as

$$\Delta_{\text{corr}} = \sum_{m,n=1}^{2} \frac{1}{2}\left(1 - \frac{1}{2}\hat{\delta}_{mn}\right)\delta_m\delta_n\left(\cos^2\theta_m - \sin^2\theta_m\right)\sin 2\theta_n \quad , \tag{2.6}$$

where $\hat{\delta}_{mn}$ is the Kronecker delta symbol. Since a phase shift δ is proportional to d/λ (d is the thickness of the material), the phase shift is also proportional to the photon energy. We can thus conclude that the phase shift from an optical window is linear in photon energy for the imaginary part and quadratic in photon energy for the real part of the RAS signal.

To eliminate windows strain during the measurement, one should pay special attention to use a low-strain window. It is also possible to search for a position for the light spots on the window where δ_1 and δ_2 cancel each other (at least partially). Another approach is to use a second window with similar strain and to find a position where the phase shifts cancel.

It is always favourable to eliminate the strain during the measurement, but despite the efforts it is often necessary to correct the spectra afterwards. Without additional measurements, the simplest way is to estimate the strain and subtract a linear (Im) or quadratic (Re) baseline from the spectra.

When additional measurements before or after the actual measurement can be made, the so-called *window correction* procedure can be applied. One possibility is to measure the spectrum of an isotropic sample (e.g. Si(001)). Any measured anisotropy is then due to the influence of the window and can be easily subtracted from the other spectra. Without an isotropic sample, two measurements S_{0° and S_{90° of the anisotropic sample are necessary – the second one with the sample rotated by ±90°. The RAS signal of the sample changes sign upon rotation by 90° because the anisotropy axes are interchanged, but the window strain does not:

$$\begin{aligned} S_{\text{window}} &= \frac{1}{2}(S_{0^\circ} + S_{90^\circ}) \\ S_{\text{corr}} = S_{0^\circ} - S_{\text{window}} &= \frac{1}{2}(S_{0^\circ} - S_{90^\circ}) \quad . \end{aligned} \tag{2.7}$$

An example for such a window correction is shown in fig. 2.5. It must be noted that the aforementioned proportionalities of the window effect cannot be found in this example.

A further problem is the calibration of the anisotropy scale. In principle, RAS apparatuses should measure exact anisotropy values. In reality, the detector as well as the amplifying and processing electronics introduce a damping factor to the modulated signal, similarly to the quantity η in ellipsometry [9]. Thus every RAS setup must be calibrated to deliver values that can be compared to those obtained with other setups.

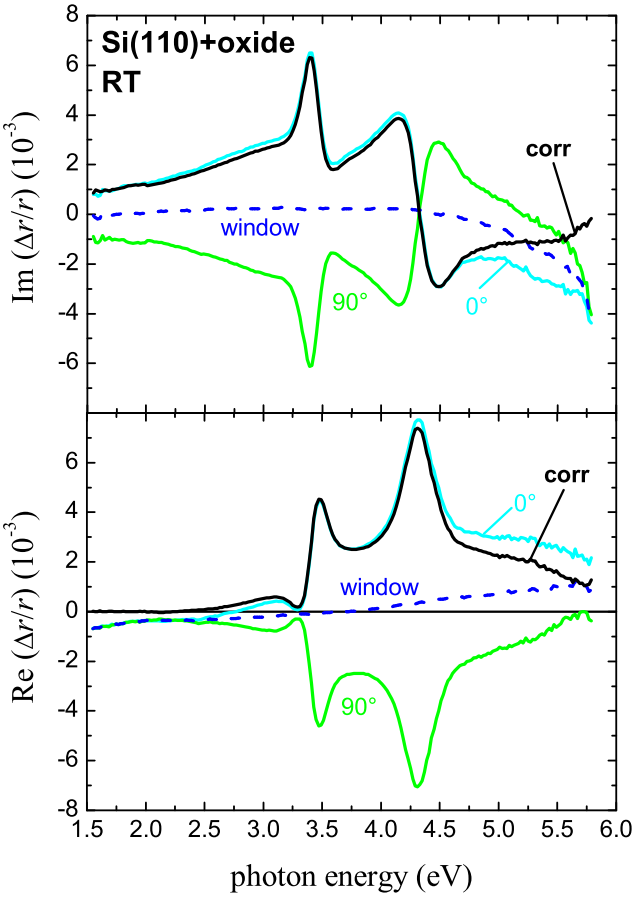

Figure 2.5:
Example for a window correction procedure using Si(110).

2.3.3 Calibration of RAS setups

A quick and simple way to calibrate a RAS apparatus is to measure the spectrum of a cheap standard sample like Si(110) (fig. 2.5) and to adjust the damping factor such that the spectrum agrees with generally accepted values.

There are two drawbacks to this method: (a) the RAS spectrum of Si(110) has sharp peaks, which is disadvantageous for setups with low spectral resolution, and (b) the spectrum cannot be calculated from well-known physical properties of the material, so the generally accepted values are also not necessarily exact.

For these reasons, two other methods of calibration are described here. They can only be used for the real part of the RAS signal.

Calibration with birefringent materials

It is possible to use a uniaxial birefringent material like crystalline quartz (α-quartz, SiO_2) for RAS calibration. This material has two very exactly known indices of refraction, the ordinary n_o and the extraordinary n_e. Crystalline quartz is optically positive in the visible spectral region, i.e. $n_e > n_o$. The refractive indices are given in fig. 2.6. For the calculation of the expected RAS signal, the amplitude reflectances

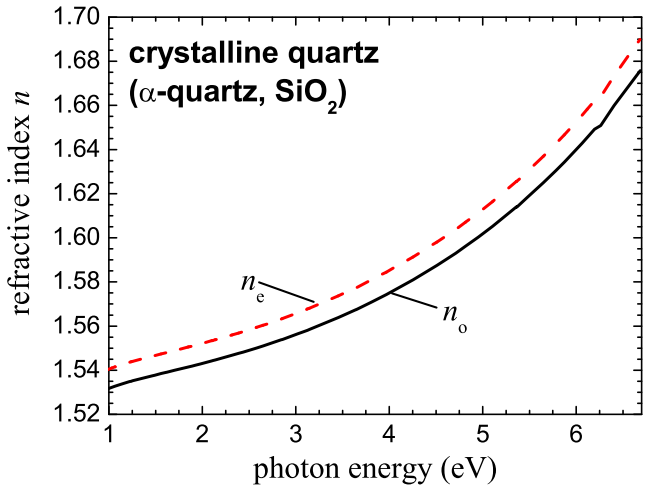

Figure 2.6: *Ordinary and extraordinary index of refraction for crystalline quartz (values taken from [17]). The difference between n_e and n_o varies from 0.0086 at 1 eV to 0.0127 at 6 eV. The extinction coefficients k_o and k_e are practically zero in this range of photon energies.*

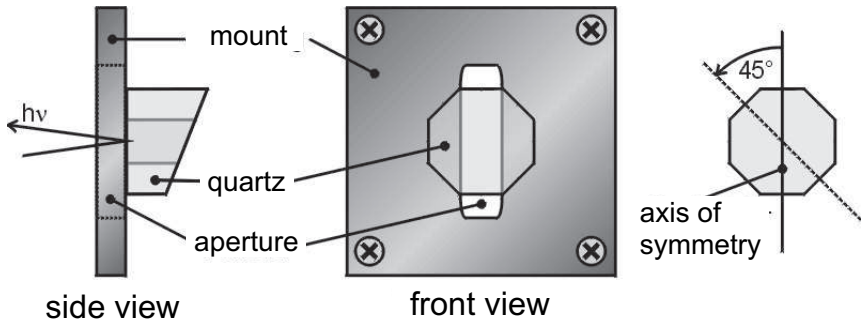

Figure 2.7: *Wedge made from α-quartz for the calibration of RAS setups. The diameter of the octagon is 10 mm. The extraordinary direction runs along the 45° line (rightmost picture).*

$$r_{o,e} = \frac{n_{o,e} - 1}{n_{o,e} + 1} \tag{2.8}$$

are plugged into

$$\frac{\Delta r}{\langle r \rangle} = 2\frac{r_e - r_o}{r_e + r_o} \quad . \tag{2.9}$$

For the measurement it is useful to have a birefringent sample that has a wedge-like geometry to avoid reflections from the back side. A sketch of a quartz wedge that was used in this work for calibration is shown in fig. 2.7. In the leftmost picture, the light

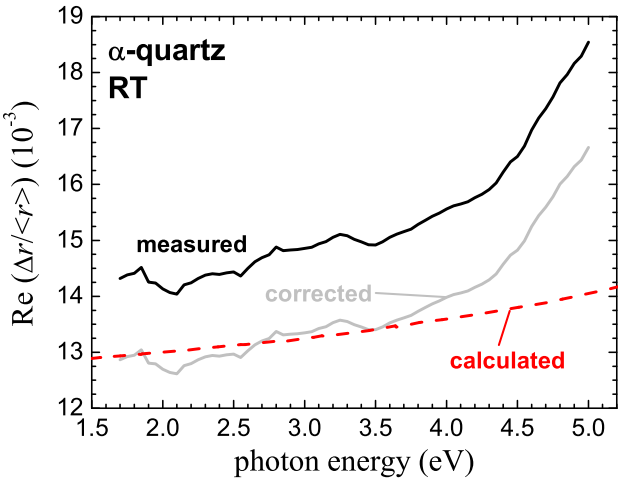

Figure 2.8: *RAS signal of α-quartz at room temperature: measured, calculated using (2.9) and values from [17], and corrected spectrum. The correction factor of 0.898 was obtained by dividing the measured values by the calculated ones and taking the mean value (ignoring photon energies > 4 eV).*

is incident from the left. The incident polarisation must be horizontal or vertical. The reflection from the first surface is measured and the reflection from the (tilted) back side is blocked.

Fig. 2.8 shows an example of an α-quartz measurement, the anisotropy calculated from the refractive indices (fig. 2.6), and the corrected measurement. Even after the correction the values for photon energies > 4 eV strongly deviate from the calculated curve. This is probably due to the small reflectance signal in the UV range. The low reflectivity of transparent materials (quartz: around 5% in the range of interest) is a general limitation of this method.

Other drawbacks are the necessity of having a wedge-like or a very thick sample to get rid of the unwanted reflection from the back side and the complications in mounting this sample (not compatible to standard sample holders). Unfortunately, it is not possible to use this method for the imaginary part.

Calibration by controlled misalignment of the polariser

A different approach for the calibration of $\mathrm{Re}(\Delta r/\langle r\rangle)$ is to use a property of the setup instead of using the property of a sample. One source of error in (2.5) is the misalignment ΔP of the polariser. When measuring an isotropic sample, this can be exploited to calibrate the RAS scale if the angle of misalignment can be controlled properly (e.g. by a stepper motor).

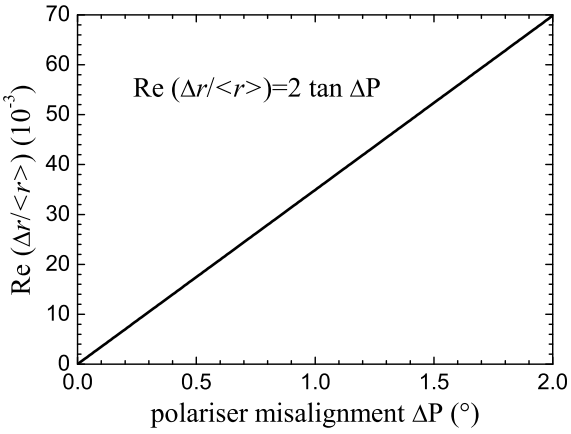

Figure 2.9: *Influence of the polariser misalignment angle ΔP on the RAS signal.*

If we assume that the misalignment ΔP corresponds to a sample with different real parts of r_x and r_y, the RAS signal is

$$\mathrm{Re}\left(\frac{\Delta r}{\langle r\rangle}\right)_{\Delta P} = 2\frac{\sin\left(\frac{\pi}{4}+\Delta P\right)-\cos\left(\frac{\pi}{4}+\Delta P\right)}{\sin\left(\frac{\pi}{4}+\Delta P\right)+\cos\left(\frac{\pi}{4}+\Delta P\right)} = 2\tan\Delta P \quad . \tag{2.10}$$

This function is plotted in fig. 2.9. For small angles ΔP, this can be linearised:

$$\mathrm{Re}\left(\frac{\Delta r}{\langle r\rangle}\right)_{\Delta P} \approx 2\Delta P \quad . \tag{2.11}$$

In this simplified form ΔP appears in (2.5).

When ΔP is given in units of mrad, the relation (2.11) becomes very simple: 1 mrad in ΔP corresponds to 2 RAS units ($= 2 \times 10^{-3}$). When using a scale of degrees, 0.1° corresponds to 3.49 RAS units.

3. Designing a multichannel RAS

The development of RAS setups is closely connected to ellipsometry. The first ellipsometric measurements at normal incidence were reported by Cardona *et al.* in 1966 [18]. Further work in this field was done by Azzam in the late 1970/early 1980's [19, 20].

The very first RAS setup (with rotating sample) was developed by Aspnes and Studna in 1985 [15, 21]. Only months later, a RAS setup with one polarizing prism and a PEM (for phase modulation) was published by Berkovits *et al.* [16]. The type of RAS setups that is mainly used today was developed in 1988 by Aspnes and coworkers [13, 14] and comprises two polarising prisms (instead of one when using a rotating sample) and a photoeleastic modulator (PEM), cf. fig. 2.4. A good review of the current status of RAS can be found in [22]. Other good but older review articles are [11, 23].

The driving force for the development of a multichannel RAS was the unsatisfying temporal resolution of spectral measurements, being of the order of 10^2 s. The formation of quantum dots, for example, happens on a sub-second time scale. The only possibility to gain spectral information of this process with a "traditional" setup (scanning RAS with a monochromator) is to repeat the experiment several times and measure RAS transients at varying photon energies. The data from the transients can be put together after the last measurement to obtain a coarse representation of a spectrum as a function of time.

This approach is not only very time-consuming, but also highly error-prone, because a high level of reproducibility and a low level of drift influences is necessary. The principle of a multichannel RAS overcomes these problems because the anisotropy is measured simultaneously at multiple wavelengths. Virtually all relevant epitaxial processes would benefit from a better temporal resolution of spectral measurements.

3.1 Design considerations

For the design of an optical multichannel RAS different solutions have to be considered, e.g. for the optical setup, the number of spectral channels, the design of the detector and the way the detector signals are processed. For the optical setup I decided to adopt the successful Aspnes design [13, 14]. In practice this arrangement has proven to have a good signal-to-noise ratio (SNR) because the modulation is done without mechanically moving parts and the modulation frequency of several tens of kHz is beyond the frequency of the quite often present mechanical vibrations (pumps etc.).

RAS designs with rotating polarising prisms were not considered because those setups have a signal modulation frequency which is too close to the frequency of mechanical and electrical disturbances, especially for application at growth machines like molecular beam epitaxy (MBE) or metal-organic vapour phase epitaxy (MOVPE) reactors. More important, the SNR is bad because of very few modulation cycles per

data point. On the other hand, multichannel setups comprising a PEM have other disadvantages which have to do with the spectral properties of the PEM (section 3.6).

The detector must have a uniform response in a frequency range of at least $0 - 200\,\mathrm{kHz}$, because ω_{PEM} is typically 50 kHz and the real part of the RAS signal is modulated with $2\omega_{\mathrm{PEM}} = 100\,\mathrm{kHz}$ (cf. section 2.3.1). This constraint rules out most CCD or CMOS devices as possible sensors. Appropriate detectors are photodiodes and photomultipliers. A further problem is the wavelength dependence of δ_{PEM}, which will be discussed in detail in section 3.6.

To process the modulated signal one can either follow the standard approach of using a lock-in amplifier for the demodulation or alternatively digitise the modulated signal directly and perform a Fourier analysis afterwards. Examples for the latter approach are two apparatuses from Jobin Yvon, the phase-modulated ellipsometer [24] and a RAS setup [25], and the "RapidRas" by Harrison et al. [26].

Those setups that directly digitise the modulated signal all make use of a multiplexer unit, which means that they only measure one spectral channel at a certain point in time and the information of all the others is discarded. When such a system is scaled up from single channel to n channels the noise increases by $\sqrt{n}$. One of the principal advantages of multichannel systems, the simultaneous acquisition of data, is lost that way. I therefore decided to use separate lock-in amplifiers for each channel, because the multichannel RAS should be able to resolve very small anisotropies in the order of $10^{-4} \ldots 10^{-5}$ necessary for e.g. the determination of doping levels. Although the costs increase linearly with the number of spectral channels this method requires no high-end A/D converters and the SNR is mainly determined by the quality and the settings of the lock-in amplifiers.

3.2 The dual-RAS setup

The multichannel RAS as discussed here is an extension of an existing conventional scanning RAS system [27]. This dual-RAS setup allows for simultaneous operation of both the scanning RAS (single detector) and the fast multichannel detection system, providing both high spectral resolution and high temporal resolution. This configuration makes benchmarking very simple. Stand-alone operation of both single- and multichannel RAS is also possible. A schematic picture of the optical setup is given in fig. 3.1 (multichannel unit indicated). A photo is shown in fig. 3.2.

The only major change in the optical path of the scanning RAS concerns the analyser prism (ANA in fig. 3.1), a special glan-air prism that has a nondispersive lateral beam exit (fig. 3.3). This additional beam is usually absorbed in standard glan-air prisms but since it contains the same information it can also be used for RAS. This arrangement is more favorable than utilising an additional beam splitter because the intensity in the optical path of the scanning RAS is not reduced. The additional beam from the analysing prism is fed into an optical multichannel analyser (OMA). It consists of a spectrograph (Jobin Yvon CP140-103) and a multichannel detector array. The detector array can be shifted along the image plane of the spectrograph in order to select the spectral range of interest. For the correction of the second order of the spectrograph, a yellow glass filter is installed in front of all detector elements for energies $\leq 2\,\mathrm{eV}$.

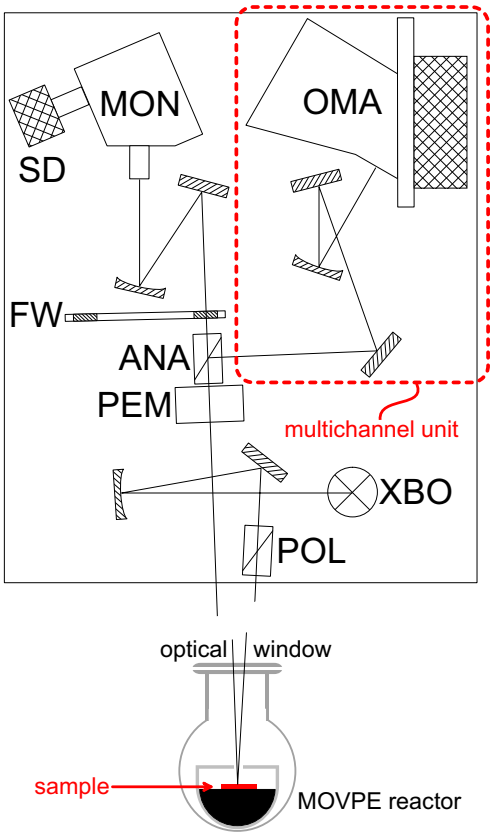

Figure 3.1:
Schematic setup of the dual-RAS system: modified standard RAS with additional multichchannel unit (dashed box). XBO: Xenon short-arc lamp; POL: polariser prism; PEM: photoelastic modulator; OMA: optical multichannel analyser; FW: filter wheel; MON: monochromator; SD: single detector; ANA: analyser prism, details shown in fig. 3.3.

3.3 Detectors

For the detection of the spatially dispersed light either an array of 8 Si photodiodes or a 32 channel photomultiplier was used.

The photodiode detector (fig. 3.4 left) was the first detector that was built for the multichannel RAS. It uses in principle the same detection system as the single channel detectors (also Si photodiodes), which made the Si diode array an ideal system for testing the feasibility of multichannel RAS. This (and the costs of lock-in amplifiers) is the reason why a number of 8 channels was considered sufficient in the beginning. The Si photodiode array consists of 8 non-equidistant Si diodes with pre-amplifiers. It was custom-made by EMM Berlin (Elektronik-Manufaktur Mahlsdorf).

The second detector (fig. 3.4 right) is a self-made sensor consisting of a linear 32-channel photomultiplier array (Hamamatsu H7260-04), a high voltage power supply and 32 operational amplifiers. It was primarily designed to have a higher spectral resolution but is has also other advantages. Only 16 out of the 32 channels were used for measurement. A detailed description of the electronics and the printed circuit board (PCB) can be found in appendix A.3.

Comparing both detector arrays, the photomultiplier has the better overall performance because the amplification level can be adjusted via the high voltage (but only for all channels simultaneously). The damping of 100 kHz-signals is negligible because it has a much higher cut-off frequency than the Si diodes ($\approx$ 1 GHz instead

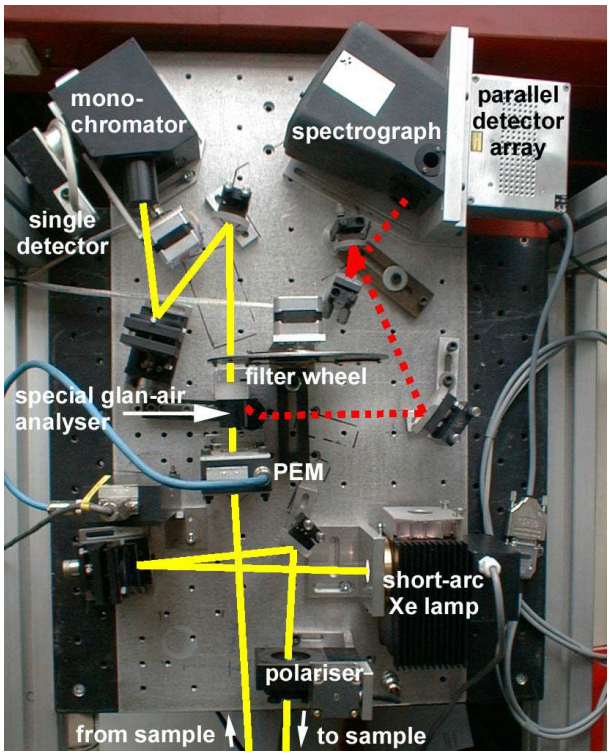

Figure 3.2:
Photo of the dual-RAS system. The continuous line (yellow) shows the light path of the standard RAS with monochromator. The multichannel light path is indicated by a dotted (red) line.

of ≈ 150 kHz). Because of the varying penetration depth, the cut-off frequency of the Si detector strongly depends on the photon energy. Moreover, the photomultiplier has more spectral positions to choose from (without displacing the array!). Only for measurements in the 1.4 – 2 eV range the diode detector has a better SNR because the quantum efficiency drops steeply above 750 nm. With a different window material (borosilicate glass instead of UV glass), the sensitivity in the IR could be enhanced, sacrificing the UV signal. The technical specifications are summarised in tab. 3.3.

3.4 Data acquisition

A schematic diagram of the data acquisition system is given in fig. 3.5. The signal of each channel is demodulated by a separate lock-in amplifier (LIA). To keep the setup

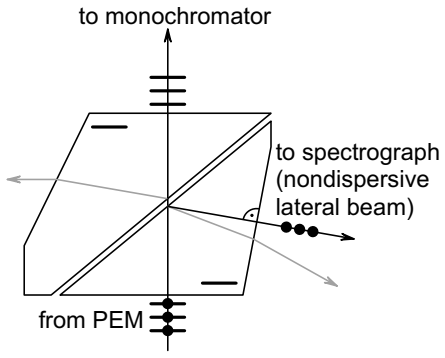

Figure 3.3:
Special glan-air prism made from calcite ($CaCO_3$) from Halle Nachfl. GmbH. It has a nondispersive lateral beam exit from which a phase-shifted signal can be obtained.

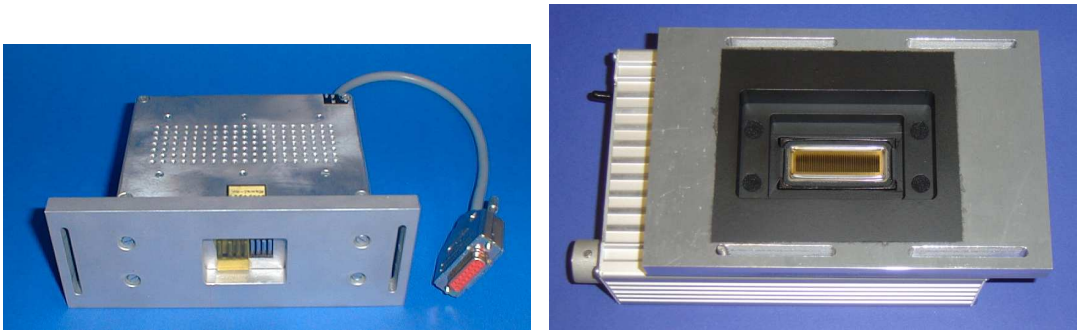

a) b)

Figure 3.4: *Photos of the detector arrays: 8 channel detector with Si photodiodes (a), built by EMM Berlin according to our specifications, and self-made 32 channel detector (b) using a photomultiplier array from Hamamatsu. The second order-filter is only shown in picture (a).*

	Si detector	PMT array
number of available channels	8	32
arrangement of spectral channels	non-equidistant in λ	equidistant in λ
detector spectral range	180 – 1100 nm	185 – 880 nm
usable spectral range	1.4 – 5 eV	1.7 – 5 eV
spectral width per channel	approx. 25 nm	approx. 20 nm

Table 3.1: *Technical specifications of the OMA. Some specifications/ restrictions are due to the combination of the spectrograph and the detector array.*

compact I use 19'' LIA boards from Femto Messtechnik GmbH (LIA-BV-150-H). They are mounted in two 19'' racks (8 LIA boards per rack) so that it is also possible to save space when using only 8 channels.

The output of the LIA, the AC component, and the unprocessed signal V_{DC}, are digitised by A/D converter cards (National Instruments 6025E or 6035E). Each card can digitise up to 16 channels with a sampling rate of 12.5 kHz per channel with 16 bit (6035E) or 12 bit (6025E) resolution. Since two signals per spectral channel have to be processed (AC and DC), 8 spectral channels require one A/D card.

3.5 Software

To control the measurement process and to display the results, a completely new software was written in LabWindows, a C dialect from National Instruments with special extensions for measurement tasks. The program reads the data from the A/D

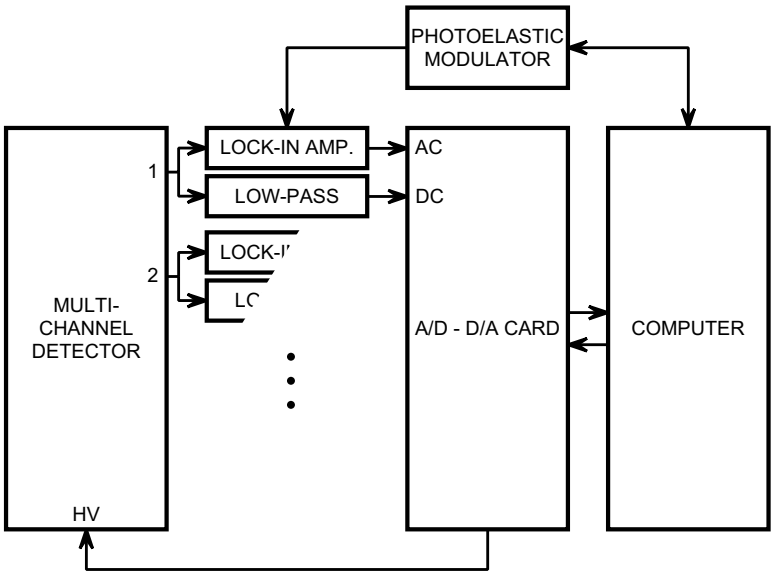

Figure 3.5: *Schematic diagram of the data acquisition system (only multichannel RAS shown). The high voltage (HV) control does only apply to the photomultiplier detector array.*

converter cards (AC values from the lock-in amplifiers and DC values) and calculates the RAS signal for each channel in real time. Additionally, a correction for the fixed PEM is applied (see sec. 3.6).

The program incorporates a module for adjusting and calibrating the channel settings, showing the data of two RAS channels simultaneously for comparison. It is possible to save and restore the settings for different tasks of measurement.

To minimise noise, the program always reads the raw data with the highest possible sample rate of the A/D card (12.5 kHz) and calculates the mean value for each point in time (corresponds to an increase of the time constant). Fig. 3.6 visualises how important the averaging is for the signal-to-noise ratio (SNR). The left graph shows transients without averaging (i.e. one measured datapoint per unit of time), the right one with averaging. Depending on the photon energy, the SNR is improved up to a factor of 3. Moreover, the averaged signal does not show beat artifacts induced by the superposition of A/D sampling frequency and vibrations/jitter of the light source.

The result of a measurement can be displayed as a successive series of spectra (like a movie), as colour-coded transients and as a colour plot. As a guide to the eye, the spectra are interpolated using a cubic spline, which I found to be a good approximation for high-temperature data (broad spectral features). In the transient display, each transient can be enabled and disabled separately to enhance the visibility. A screenshot of the program is shown in fig. 3.7.

It is also possible to perform simple mathematical operations on the measured values (i.e. to correct for a wrong sign of the spectrum). The data is stored in ASCII files with the full set of parameters to facilitate evaluation.

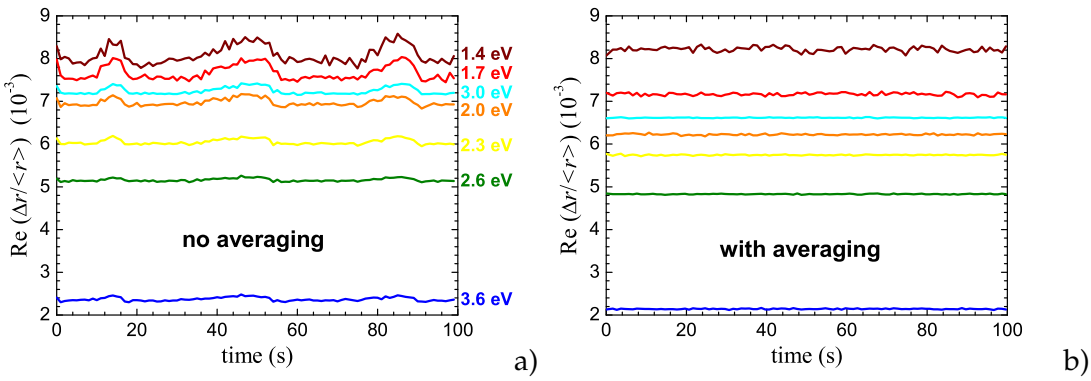

Figure 3.6: *Comparison of multichannel transients of a static surface measured without averaging (a) and with averaging (b). The temporal resolution was* 1 *s.*

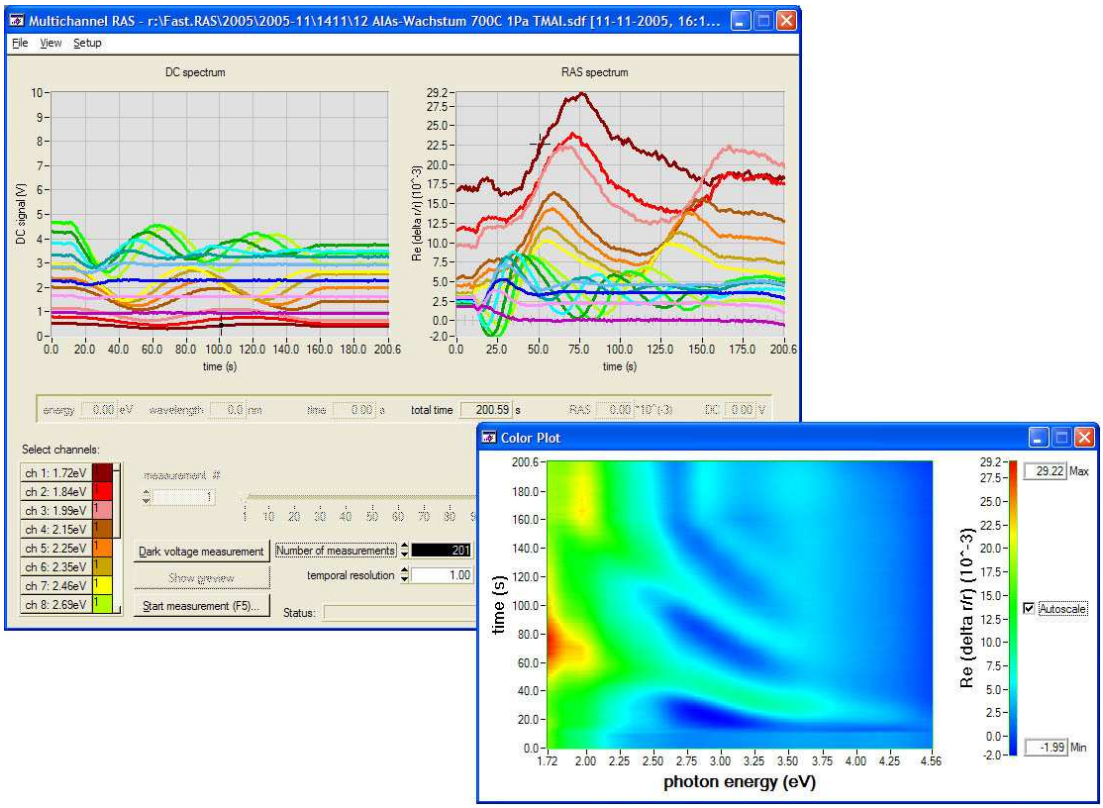

Figure 3.7: *Screenshot of the measurement software. Displayed are RAS transients taken during growth of AlAs on GaAs.*

3.6 Bessel correction

A general problem that arises in a multichannel RAS setup with a photoelastic modulator is the wavelength dependence of the PEM retardation δ_{PEM}. In scanning RAS, at

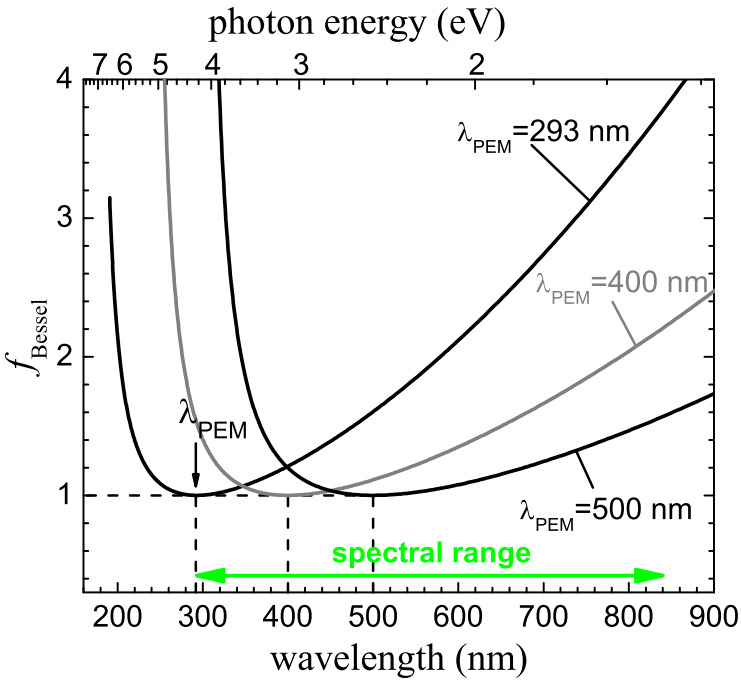

Figure 3.8: *Bessel correction factor $f_{\mathrm{Bessel}}(\lambda)$ for $Re(\Delta r/\langle r\rangle)$ as defined in (3.1) for three different values of λ_{PEM}. The curve with $\lambda_{\mathrm{PEM}} = 293\,nm$ represents the value chosen for the photomultiplier array. The typical spectral range is also given.*

every wavelength the control voltage of the PEM (V_{PEM}) is adjusted to keep the retardation at the value where $J_i(\delta_{\mathrm{PEM}}(\lambda))$ is maximum (imaginary part: $J_1(1.8423) = 0.5841$; real part: $J_2(3.0521) = 0.4862$).

For a multi-spectral detection approach, V_{PEM} must be held fixed because all channels are to be read simultaneously. Consequently, δ_{PEM} is different for all wavelengths and the maximum condition is only fulfilled for a single wavelength λ_{PEM} which in theory can be chosen anywhere in the spectral range. The RAS signal at wavelengths $\lambda \neq \lambda_{\mathrm{PEM}}$ must be corrected by a factor

$$f_{\mathrm{Bessel}}(\lambda) = \frac{J_i\Big(\delta_{\mathrm{PEM}}(\lambda_{\mathrm{PEM}})\Big)}{J_i\Big(\delta_{\mathrm{PEM}}(\lambda_{\mathrm{PEM}})\frac{\lambda_{\mathrm{PEM}}}{\lambda}\Big)} \quad , \tag{3.1}$$

which is plotted in fig. 3.8. The real part of the RAS signal is then

$$\mathrm{Re}\left(\frac{\Delta r}{\langle r\rangle}\right) = \frac{V_{\mathrm{AC2}} f_{\mathrm{Bessel}}(\lambda)}{2J_2\Big(\delta_{\mathrm{PEM}}(\lambda_{\mathrm{PEM}})\Big)V_{\mathrm{DC}}} = \frac{V_{\mathrm{AC2}}}{2J_2\Big(\delta_{\mathrm{PEM}}(\lambda_{\mathrm{PEM}})\frac{\lambda_{\mathrm{PEM}}}{\lambda}\Big)V_{\mathrm{DC}}} \quad . \tag{3.2}$$

If λ_{PEM} is chosen somewhere in the middle of the spectral range it is found that the correction does not work well for wavelengths $\lambda < \lambda_{\mathrm{PEM}}$. This probably has two reasons: firstly, the spectral width of detector channels (in units of photon energy) is larger in the UV than in the IR range, owing to the inverse relationship of wavelength

and photon energy. Secondly, a spatially nonuniform distribution of the strain $P(V_{\mathrm{PEM}})$ over the PEM's aperture leads to a larger range of phase shifts in the UV than in the IR because

$$\delta_{\mathrm{PEM}}(t) = 2\pi \frac{d}{\lambda} P(V_{\mathrm{PEM}}) \sin \omega_{\mathrm{PEM}} t \quad , \tag{3.3}$$

where d is the thickness of the modulator crystal. The best choice for λ_{PEM} was found to be the wavelength of the spectral channel with the shortest wavelength. This scheme was also used by Harrison et al. [26].

4. Benchmarking of multichannel RAS

In this section a comparison between results obtained with scanning RAS and multichannel RAS will be made and the capabilities of multichannel RAS will be demonstrated.

4.1 RAS spectra of static surfaces

The simplest benchmarking of the multichannel RAS can be made by comparing spectra of the scanning RAS to those measured simultaneously with multichannel RAS. This is shown for two static surfaces in fig. 4.1: an oxidised surface at room temperature and a reconstructed surface at growth temperature.

The agreement is fairly good because both surfaces to not have sharp spectral structures. In such cases the multichannel RAS can detect the key features of the spectra. The deviations are mainly due to the lower spectral resolution of the detector array ($\Delta\lambda = 20\,\text{nm}$) compared to the monochromator ($\Delta\lambda = 8\,\text{nm}$). This explains why the difference is larger at narrow features and steep slopes of the RAS spectra.

The values of channel 1 (lowest photon energy) must be regarded with caution because of a high noise level. This is strongly improved when using the Si diode detector array.

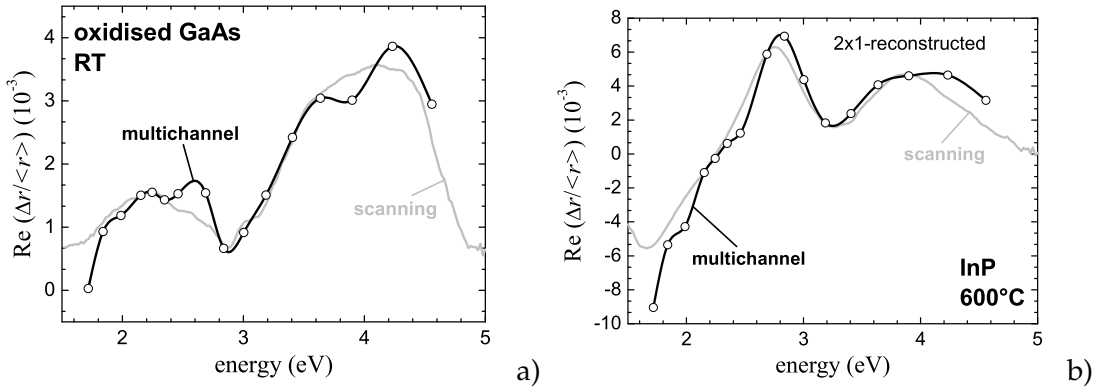

Figure 4.1: *RAS spectra of static surfaces: oxidised GaAs (001) at room temperature (a) and* (2×1)*-reconstructed InP at* $600°C$ *(b), both measured with scanning and multichannel RAS. The datapoints of the multichannel RAS are connected by splines as a guide to the eye.*

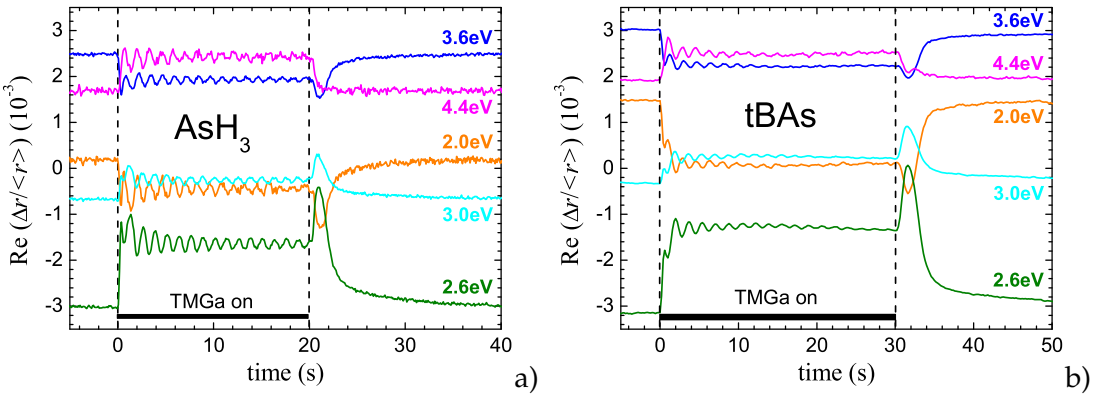

Figure 4.2: *RAS transients of GaAs growth at* 520°*C using* 100 *Pa* AsH_3 *(a) and* 2 *Pa tBAs (b).*

4.2 Monolayer oscillations during GaAs growth

To demonstrate the fast time response, GaAs was grown at low temperature (520°C) to measure monolayer growth oscillations. At this temperature GaAs grows in 2D island mode and distinctive monolayer-related oscillations should be visible in the RAS signal [27, 28].

Monolayer oscillations have also been investigated by measuring many transients at different photon energies successively with a scanning RAS [29]. The transients were set together to obtain a spectrum as a function of time. This is a very time-consuming and error-prone procedure which can be greatly facilitated by using a multichannel RAS.

Fig. 4.2a shows examples of multichannel RAS transients of monolayer oscillations taken during growth at 520°C for 20 s with p_{AsH_3} = 100 Pa and p_{TMGa} = 0.5 Pa.

In a similar experiment 2 Pa tertiary-butyl arsine (tBAs) was used as the arsenic precursor (fig. 4.2b). The SNR of the multichannel transients is comparable to that of the scanning RAS.

A direct comparison of both growth experiments reveals that the two arsenic precursors AsH_3 and tBAs produce very similar transients. The amplitude of the oscillations is larger for AsH_3. Therefore the following multichannel spectra refer to this measurement rather than the one with tBAs. The growth oscillations occur at all measured photon energies. The growth rates are 810 nm/h for arsine and 600 nm/h in the case of tBAs (values obtained from the period of the oscillations). The reduced growth rate when using tBAs is probably due to a higher surface coverage with methyl groups (from TMGa decomposition) because AsH_3 compared to tBAs produces more hydrogen radicals which can remove the methyl groups from the surface. When TMGa is switched off all transients return to their starting level via an intermediate reconstruction (switch-off peaks at 21.2 s in fig. 4.2a and 31.6 s in fig. 4.2b). This high reproducibility is an indicator for the good quality of the growing surface.

During layer-by-layer growth the surface oscillates between Ga-rich and As-rich conditions. To illustrate this behaviour fig. 4.3b shows multichannel spectra that correspond to different times during the measurement (see fig. 4.3a). Spectrum A

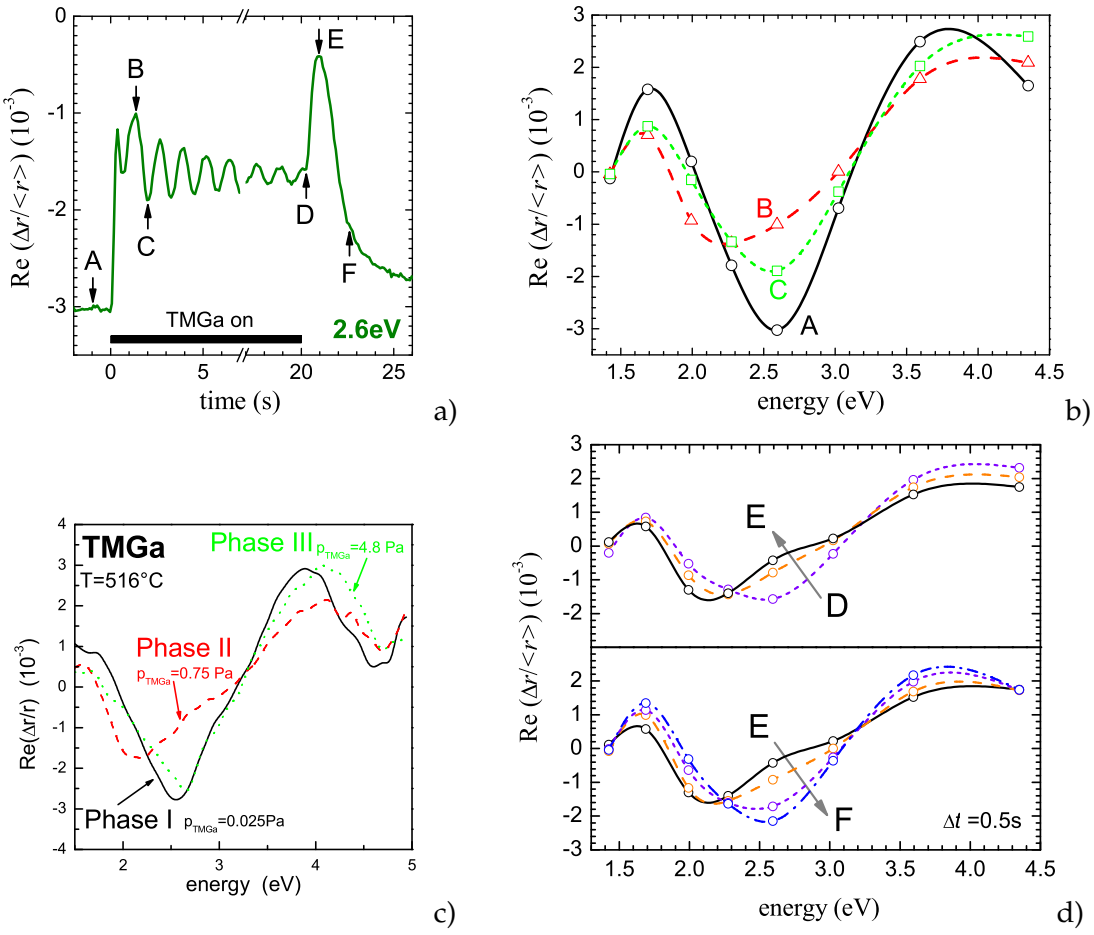

Figure 4.3: *a) Extract from fig. 4.2a: 2.6 eV transient with assigned times A-F. b) Multichannel RAS spectra before (A) and during growth (B and C). c) Typical scanning RAS spectra measured during GaAs growth (p_{AsH_3} = 120 Pa, taken from [30]). d) Multichannel RAS spectra after TMGa switch-off (D-E-F).*

refers to the pre-growth surface while spectra B and C were taken during growth, at a local maximum (B) and a local minimum (C) of the 2.6 eV transient. Comparing spectra B and C, the most outstanding difference is the shift of the spectral minimum between ~ 2.2 eV (B) and 2.6 eV (C).

For the growth of GaAs with different TMGa partial pressures at various temperatures and a constant AsH_3 partial pressure typical RAS spectra (corresponding to regions in the pressure vs. temperature phase diagram) have been observed. The first classification (phases I, II and III, corresponding to increasing Ga partial pressures) was done by Reinhardt et al. [31]. The phase I surface corresponds to a (disordered) $c(4 \times 4)$ reconstruction. Phase II is a partially Ga-dimer-covered surface. Creighton et al. [32] explained the nature of the phase III surface as being an As-rich (1×2)-CH_3 reconstruction.

Comparing the spectra of fig. 4.3b to recent work (fig. 4.3c, taken from [30]), the spectrum prior to growth (A) corresponds to phase I while the spectra during growth can be identified as phase II-like (B) and either phase I or phase III (C). To decide whether spectrum C corresponds to a phase I or phase III surface the intermediate reconstruction the surface undergoes when TMGa is switched off (D-E-F in fig. 4.3a) is examined in fig. 4.3d. Starting at the increasing slope of the switch-off peak (D), the minimum of the spectra is shifted from 2.6 eV to 2.1 eV (E) and then moves back to 2.6 eV (F). If the surface during growth would oscillate between phase II and phase I, the switch-off peak should not be present and from D the transients should return directly to their corresponding pre-growth levels (phase I). If we assume the growing surface to oscillate between phase II and phase III, the switch-off peak can be explained by the desorption of the adsorbed methyl groups, leaving a Ga-rich surface for a short time before the As-rich $c(4 \times 4)$ reconstruction is developed. This clearly shows that during growth the surface oscillates between a smooth phase III (few steps, methyl groups adsorbed) and a Ga-rich phase II surface (more steps around islands).

4.3 Growth of InAs quantum dots on GaAs

The fabrication of low-dimensional semiconductor structures has become a key research topic in recent years. By reducing the size of structures towards the order of magnitude of the de Broglie wavelength, quantum effects can be exploited in electronic devices. One example is the improvement of the properties of semiconductor lasers by incorporating quantum dots in the active region of the laser.

The realisation of such structures with conventional methods (optical lithography) is not possible and e-beam lithography is too expensive for mass production. An alternative is the self-organised growth of quantum dots: the growth of islands in the so-called *Stranski-Krastanow* growth mode. In this mode, a large lattice mismatch between substrate and QD material (e.g. InAs on GaAs) leads to a self-organised formation of islands (size: some tens of nm). After reaching a critical thickness, the QD material no longer grows in the two-dimensional mode (*Frank-van der Merwe*) but forms three-dimensional islands (*Stranski-Krastanow*).

The self-organised growth of quantum dots is a process where the capabilities of the multichannel RAS can be well demonstrated because the process cannot be easily repeated without changing or overgrowing the sample. Gupta *et al.* have studied the growth of InAs quantum dots on GaAs with conventional RAS and have published multitransient RAS measurements [33]. The transients were recorded sequentially and 18-point spectra were constructed from these data after the measurements.

Such effort is not necessary when using a multichannel RAS system. In this part I will present measurements taken during the growth of InAs quantum dots (QDs) on GaAs(001) in MOVPE.

Fig. 4.4 shows spectra recorded during the first seconds of quantum dot evolution at 480°C. The precursors were 5 Pa tBAs and 0.5 Pa TMIn. The nominal thickness of the InAs layer was 2 monolayers (corresponding to 2.0 s of TMIn exposure).

The set of spectra in fig. 4.4a shows a very rapid destruction of the $c(4 \times 4)$ reconstructed GaAs surface within fractions of a second. The peak structure is reversed

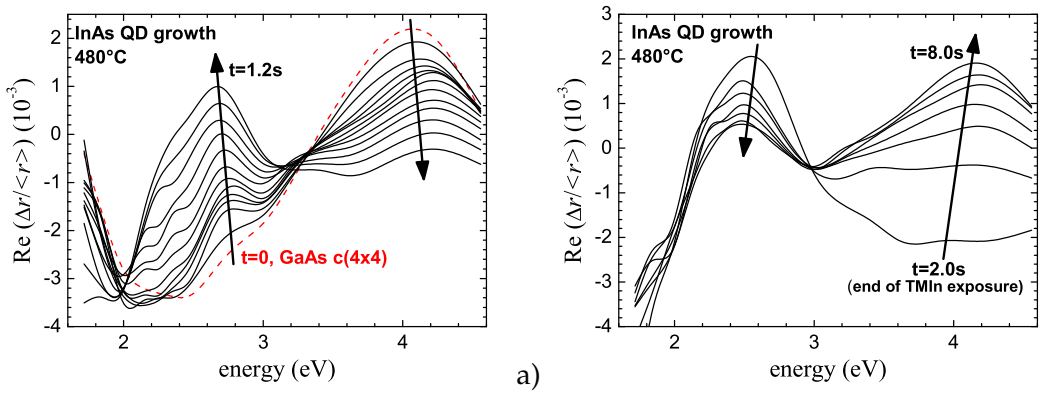

Figure 4.4: *Time-resolved RAS spectra of InAs QD growth on GaAs(001) at 480°C: a.) first 1.2 s in steps of 0.1 s, b.) range from 2 – 8 s in steps of 1 s. The nominal thickness of InAs was 2 ML (2 s exposure time). The spectra have a resolution of 16 datapoints. They are not shown for reasons of clarity.*

(emerging peak around 2.6 eV, reduced peak at 4.1 eV), leaving the anisotropy near photon energies of ≈ 3.2 eV almost unchanged.

This fast change of the $c(4 \times 4)$ spectrum, especially the inversion of the sign at 2.6 eV, is an indication for a closed (2×4)-reconstructed InAs layer: in island growth mode a fraction of the underlying $c(4 \times 4)$-reconstructed GaAs would still be visible.

After 2 s the surface does not change as rapidly as before and, within a few seconds, evolves towards a spectrum that resembles the (2×4) reconstruction of InAs. The development from a local minimum to a local maximum near 2.6 eV can (in this case) be explained by a rotation of As dimers by 90° ([34], DFT-LDA calculations). The evolution of a maximum near 4.2 eV can be explained by the formation of anisotropic InAs islands [35].

The saturation of the RAS signal in the spectral range below 3 eV for $t > 2$ s reflects the transition from 2-dimensional to 3-dimensional growth (growth beyond the critical thickness). This could be verified by simultaneous RAS/RHEED and RAS/SE measurements [35]. The 2D-3D transition can be better visualised by plotting the transient RAS signal at a fixed photon energy. This is shown for 2.6 eV in fig. 4.5 (lower graph). The transient shows a rapid increase when the indium source is switched on. The maximum at $t = 2$ s corresponds to the 2D-3D transition - a further TMIn supply (above the critical thickness) would lead to a similar transient. After the maximum, ripening processes lead to a reduction of the RAS signal.

The upper graph in fig. 4.5 is shown for comparison to the experiments of Steimetz *et al.* [36]. The characteristics of the transients are comparable but the process in the lower graph (this work) is much faster. This is due to a higher temperature and other different growth conditions (higher total pressure etc.).

The application of multichannel RAS to quantum dot growth shows that it is beneficial to be able to get a spectral information instead of single wavelength measurements. The low-energy spectral channels deliver information about the 2D-3D transition while

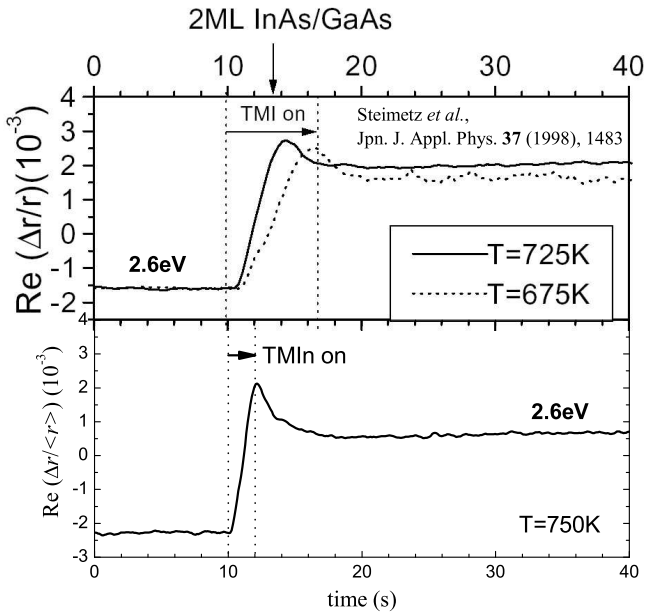

Figure 4.5: *RAS transient at 2.6 eV taken during growth of quantum dots. The upper part of the graph (taken from [36]) is shown for comparison.*

the high-energy range reflects the morphology of the surface. The different stages of quantum dot formation can be fully monitored with one measurement.

5. Determination of the doping level of III-V-semiconductors with RAS

One of the most important parameters of a semiconductor is the concentration of free carriers. Although an *intrinsic* semiconductor is an interesting material, the real power of semiconductors is realised by adding small, controlled amounts of specific impurity (dopant) atoms, thus producing an *extrinsic* semiconductor.

The technologically desired impurities are shallow acceptors and donors, having ionisation energies close to the valence and the conduction band, respectively. The smaller the difference between ionisation energy and the corresponding band edge energy is, the more carriers are available already at room temperature.

Usually the concentration of free carriers (or doping level) can only be measured *ex situ*, i.e. after growth. Technologically it would be very much desirable to measure the free carrier concentration during growth in order to vary the amount of dopant atoms if the doping is off its target value. Especially for devices with many epitaxial layers, growth could be optimised and the number of defective wafers could be reduced.

The obvious approach is to develop known *ex situ* methods for application during growth. Unfortunately, the majority of these methods needs an electric contact to the sample. This is very complicated to implement for high temperature processes and would strongly influence the growth process.

A possible alternative is to make use of the band bending (Schottky effect). This effect is used in C/V profiling to determine carrier profiles. The sample is destroyed by the measurement because of the etchant. Such a C/V measurement can also be done *in situ* by an external electric field [37]. However, the distance between electrode and sample must be very small (micron region) to reach the necessary field strength. This is complicated to handle at growth temperature and constricts growth.

The most promising methods for *in situ* doping determination are optical techniques – they are non-destructive, work in gaseous and liquid environments and do not (or only very little) influence growth.

In doped semiconductors, light with photon energy below the band gap can be scattered by the free carriers. At the *plasma edge*, the reflectivity drops steeply to almost zero ([38] p. 296ff). The energetic location of the plasma edge (typically in the range of the far and mid-infrared) depends on the free carrier concentration, which gives a possibility to determine the doping level via a reflection measurement. The result of such a measurement depends strongly on the temperature (band edge shift and thermal broadening) and is hard to perform at high temperature (emission from the sample and the sample holder/susceptor).

In situ Raman spectroscopy is a further method that makes use of a combination of many effects. On one hand, the electric field of the band bending can broaden the spectral structures. On the other hand, phonons and impurities (and plasmons at

higher doping levels) can be measured directly [39]. For *in situ* monitoring, the biggest problem is the decrease of these effects with increasing temperature.

Last but not least, it was shown already in 1987 that RAS is sensitive for the electric field induced by doping [40]. Especially at the critical points of the band structure, like the E_1 transition, a typical structure appears. This can be evaluated by subtracting the spectrum of an undoped sample.

This chapter intends to study the influence of doping on the RAS signal. A new effect that allows to determine the growth rate together with the doping level will be discussed in detail in chapter 6.

5.1 Overview of III-V dopants

The effect of doping impurities is mainly governed by the number of valence electrons. In an elemental semiconductor like Si or Ge (group IV in the periodic system), an impurity atom with 5 valence electrons will act as a donor, introducing an extra electron that is only weakly bound to the impurity atom. Atoms with 3 valence electrons will act as acceptors, creating missing bonds (holes).

These impurities form a system similar to a hydrogen atom. The binding energies of such *shallow* or *hydrogen-like* impurities are in the meV range. At room temperature, these impurities are ionised and contribute to the conductance.

In the band scheme picture, hydrogen-like donor states are situated below the conduction band while acceptor states have energies above the valence band. A donor level is defined as being neutral if filled by a conduction band electron, and positive if empty (= ionised donor). An acceptor level is neutral if empty, and negative if filled by a conduction band electron (= ionised acceptor).

Leaving the simple case of elemental group IV semiconductors, the situation becomes more complicated when going to binary systems. Here the lattice position of an impurity atom is important to determine whether it acts as a donor or as an acceptor.

The n-type dopants for III-V semiconductors are either group IV elements (C, Si, Ge, Sn) substituted on the group III sublattice or group VI elements (S, Se, Te) substituted on the group V sublattice. For p-type doping one has again two choices: group II elements (e.g. Cr, Mn, Zn) substituted on the group III sublattice or group IV (e.g. C, Ge) elements substituted on the group V sublattice. Tab. 5.1 lists the most typical dopant elements for III-V semiconductors, their respective type and ionisation energy.

	GaAs	InAs	GaP	InP	GaSb[a]	InSb
N_i/cm^{-3} (300 K)	1.8×10^6 [41]	8.6×10^{14} [41]	2.7 [41]	8.2×10^6 [41]		1.6×10^{16} [41]
Be (group II)	$p = 0.028$ eV [42]		$p = 0.0566$ eV [3]	$p = 0.03$ eV (MBE) [43]		
C (group IV)	$p = 0.02$ eV [44]		$p = 0.0543$ eV [3]	$p = 0.04$ eV [43]		
Cd (group II)	$p = 0.0347$ eV [42]	$p = 0.015$ eV [45, 46]	$p = 0.1022$ eV [3]	$p = 0.057$ eV [43]		$p \approx 0.01$ eV [43]
Cr (group II)						$p \approx 0.07$ eV [43]
Cu (group II)		$n > 0.001$ eV [43]		$p = 0.06$ eV [43]		p [43]
Ge (group IV)	$n = 0.0061$ eV [42]; $p = 0.03$ eV [44] $p = 0.0404$ eV [42]	$n > 0.001$ eV [43]; $p = 0.014$ eV [45, 46]	$n = 0.204$ eV; $p = 0.265$ eV [47, 48]	$n \approx 0.0057$ eV; $p = 0.021$ eV [43]	p [43]	p (acc. to Wafertech)
Hg (group II)				$p = 0.098$ eV [43]		
Li (group I)			P: $n = 0.091$ eV; Ga: $n = 0.061$ eV [47, 48]			
Mg (group II)			$p = 0.0599$ eV [47]	$p = 0.03$ eV (MBE) [43]		
Mn (group II)				$p = 0.27$ eV [43], usually n-type		
S (group VI)	$n \approx 0.006$ eV [44]	$n > 0.001$ eV [43]	$n = 0.107$ eV [47, 48]	$n \approx 0.0057$ eV [43]	n [43]	$n \approx 0.0007$ eV [43]
Se (group VI)	$n = 0.0059$ eV [42]	$n > 0.001$ eV [43]	$n = 0.105$ eV [47, 48]		n [43]	$n \approx 0.0007$ eV [43]
Si (group IV)	$n = 0.0058$ eV [42]; $p = 0.0345$ eV [42] $p = 0.03 - 0.22$ eV [44]	$n > 0.001$ eV [43]; $p = 0.02$ eV [45, 46]	$n = 0.085$ eV; $p = 0.210$ eV [47, 48]	$n \approx 0.0057$ eV; $p = 0.03$ eV [43]	p [43]	
Sn (group IV)	$n \approx 0.006$ eV; $p \approx 0.2$ eV [44]	$n > 0.001$ eV [43]; $p = 0.01$ eV [45, 46]	$n = 0.072$ eV [47, 48]	$n \approx 0.0057$ eV [43]		
Te (group VI)	$n \approx 0.03$ eV [44] $n = 0.0058$ eV [42]	$n > 0.001$ eV [43]	$n = 0.093$ eV [47, 48]		n [43]	$n \approx 0.0007$ eV [43]
Zn (group II)	$p \approx 0.025$ eV [44] $p = 0.0307$ eV [42]	$p = 0.01$ eV [45, 46]	$p = 0.0697$ eV	$p = 0.035$ eV [43]	p [43]	$p \approx 0.01$ eV [43]

Table 5.1: *Overview of dopant elements for III-V semiconductors and their respective ionisation energies (n and p). Also given is the intrinsic doping concentration N_i.*

[a] The dominant acceptor of undoped GaSb seems to be a native defect. This acceptor is doubly ionizable.

5.2 Doping and the internal electric field

The question that will be addressed in this section is the relationship between the doping concentration and the internal electric field. This relationship is necessary for the further treatment of the influence of the doping concentration on the RAS signal.

The Fermi level of a doped semiconductor is shifted from approximately mid-gap (semi-insulating) to a position between the energy states of the donor atoms and the conduction band edge (n-type) or between the energy states of the acceptor atoms and the valence band edge (p-type).

As was pointed out by Mönch [49], surface states fix the Fermi level of the semiconductor and consequently create a band bending in order to maintain thermodynamic equilibrium, in a similar way as Schottky barriers. Hence for this calculation the Schottky model of an abrupt interface (Schottky contact, cf. e.g. [50]) is used.

The band bending generates an electric field that decreases linearly with distance z from the interface (fig. 5.1, shown here for the surface of an n-type semiconductor):

$$E_{\text{Schottky}}(z) = \begin{cases} \sqrt{\frac{2eN\phi_0}{\epsilon_0\epsilon}}\left(1 - \frac{z}{z_d}\right) & (z \in [0, z_d]) \\ 0 & (z > z_d) \end{cases} \quad . \tag{5.1}$$

N is the carrier concentration, ϕ_0 (in units of Volts) is the surface potential barrier for electrons that determines the position of the Fermi energy E_F at the surface and z_d is the depletion width

$$z_d = \sqrt{\frac{2\epsilon_0\epsilon\phi_0}{eN}} \quad . \tag{5.2}$$

A typical value for the depletion width is e.g. $z_d \approx 300\,\text{nm}$ for GaAs with a free carrier concentration of $1 \times 10^{16}\,\text{cm}^{-3}$ at 300 K and a Fermi level pinning of $\phi_0 = 0.6\,\text{V}$. When the free carrier concentration is increased by two orders of magnitude, the depletion width is reduced by one order of magnitude ($z_d \approx 30\,\text{nm}$ for $1 \times 10^{18}\,\text{cm}^{-3}$).

5.3 Measurement of doping concentration with RAS

Since the late 1960s/ early 1970s it was known that an applied electric field changes the form of electroreflectance (ER) spectra [51, 52] (see fig. 5.2) and that the built-in electric field from doping has an influence on photoreflectance (PR) spectra [53, 54].

The RAS response of doped III-V semiconductors is also influenced by the doping-induced internal electric field, cf. sec. 5.2 and 5.4. Figure 5.3 shows this influence on the RAS spectrum of GaAs. The most prominent feature is an oscillatory structure around the E_1 and $E_1 + \Delta_1$ critical points. This characteristic influence is visible already in one of the first publications about RAS from 1985 by Aspnes ([21], GaAs).

In 1986 Berkovits *et al.* studied the influence of different doping concentrations on the reflectance anisotropy spectra of GaAs(110) and InSb(110) [55]. The biggest changes in the spectra occurred in the region of the $E_1/E_1 + \Delta_1$ critical points where an oscillatory structure was observed. The magnitude of the oscillation was found to depend on the doping level, being larger for higher concentrations. The sign of the oscillation depends on the type of doping (n or p).

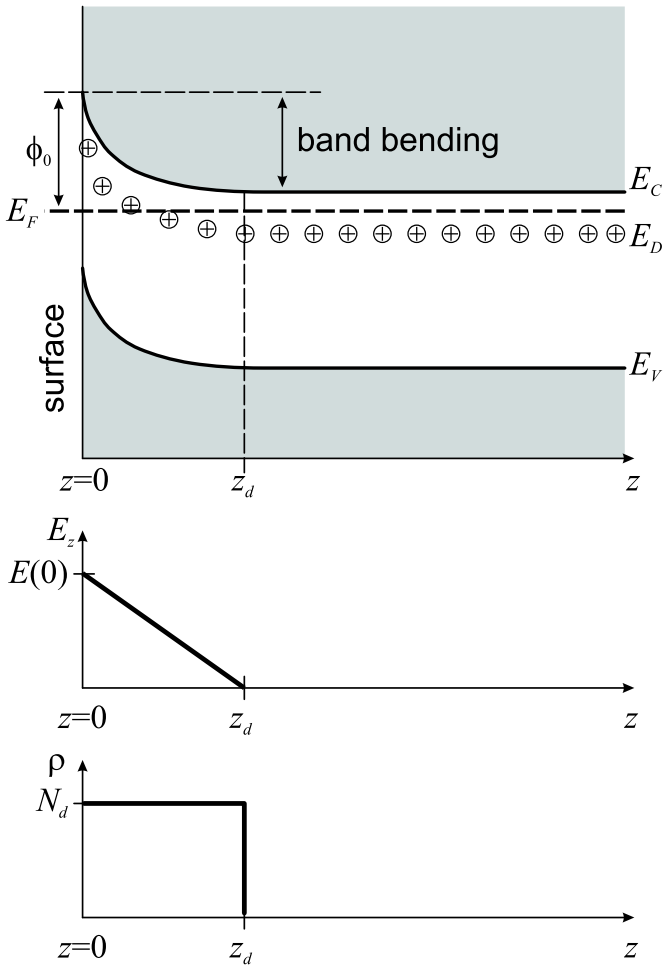

Figure 5.1: *Schottky model: Sketch of the band bending for an n-type semiconductor at the surface, the variation of the electric field E_z along the z direction and the density of free carriers ρ. E_C and E_V are the conduction- and valence band energies and E_F is the position of the Fermi level. E_D ($\oplus$) is the energy and N_d the concentration of the donors. $E(0) = \sqrt{2eN\phi_0/(\epsilon_0\epsilon)}$ as given in (5.1). ϕ_0 is the surface potential barrier for electrons. For p-type doping, the bands are bent downwards.*

They concluded that surface band bending and the resulting deformation of the crystal are the reasons for the observed spectral changes. The Fermi level is pinned by the surface states, thus generating an electric field (cf. sec. 5.2). The correctness of this assumption was demonstrated by applying a static bias to the GaAs surface through an electrolyte. The spectra with applied bias showed the same oscillatory feature.

In 1987 a study concerning the influence of doping on GaAs(001) was published by Acosta-Ortiz and Lastras-Martínez [40]. They concluded that the doping-related structure originates from the linear electro-optic effect (LEO, section 5.4) in the near-surface region. In a further work of these authors [52] a vertical shift of the spectrum

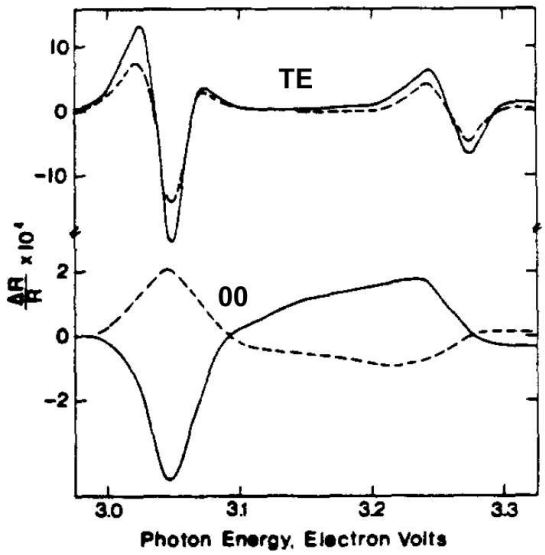

Figure 5.2: *Typical electroreflectance spectra of GaAs(110) at 79K for different orientations of the electric field (*23 *kV/cm). The figure is taken from [51].*

(cf. fig. 5.3) was also measured, but this was (probably erroneously) attributed to the imperfect alignment of the sample in the RAS apparatus (rotating sample type).

Tanaka *et al.* [56] showed for the first time *in situ* RAS measurements at growth temperature (470°C) for GaAs. In this work, a linear relationship between the integrated area of the oscillation and the doping level was established empirically. This paper is one of the most fundamental works in this field and laid the foundations for future research. However, the idea of integrating the area of the oscillatory structure was not followed further. Especially the shift of RAS spectra with doping level cannot be treated with this method.

In a work by Chen *et al.* [57] it was concluded that the LEO amplitude is proportional to the square root of the doping concentration because of the surface Fermi-level pinning. On the other hand, Kumagai *et al.* [58] found a cubic root dependence for n-type ZnSe. A similar power-law dependence was found for p-type ZnSe [59].

Sobiesierski *et al.* [60] and Kumagai *et al.* [58] derived a relation for the magnitude of the RAS changes by considering the doping-induced electric field and the penetration depth of the light (cf. sec. 5.4).

Since it is not trivial calculate or simulate RAS spectra, such studies are often evaluated without having a concise theory behind. For some systems, the principal features of the RAS spectrum (except for a shift in photon energy) could be calculated by density functional theory (DFT, cf. e.g. [61]). Schmidt *et al.* [62] calculated the influence of an electric field (doping) on the RAS spectrum using DFT. An example for the electrostatic potential and the corresponding change in electron density is given in fig. 5.4.

They concluded that especially the contributions from electronic transitions between surface-perturbed bulk states (in contrast to surface structure signatures) are

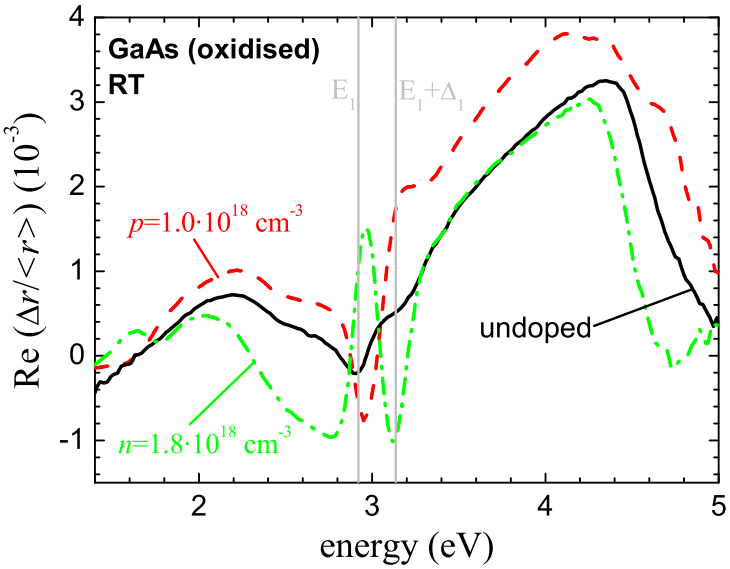

Figure 5.3: *RAS spectra of doped and undoped, oxidised GaAs at room temperature. The influence of the doping is visible as an oscillatory structure near the E_1 and $E_1 + \Delta_1$ critical points (grey vertical lines) and as an overall shift of the spectra. The sign of the oscillation and the sign of the shift depend on the type of doping (n or p). This is an indication that the observed changes are electric field-dependent.*

modified by surface electric fields via the LEO. The modifications of the RAS features, induced by the electric field, strongly depend on the reconstruction. The comparison of the DFT results (difference spectra in fig. 5.5) to experiment reveals that especially the feature at the E_1 transition is well reproduced for the $c(4 \times 4)$ and the $\beta 2(2 \times 4)$ reconstructions, although at a shifted energy position. The $E_1 + \Delta_1$ feature is not visible because spin-orbit splitting was not included in the calculation. Some other features of the $c(4 \times 4)$ difference spectrum also occur in the calculated spectrum (arrows in fig. 5.5). However, the examples shown reflect the problem that DFT model systems strongly depend on the number of atoms that can be handled numerically.

A handwaving argument for the occurence of an anisotropy due to doping is sketched in fig. 5.6: The electric field from the band bending shifts the electrons in the bonds. In this picture, the electrons from the bonds along $[1\bar{1}0]$ are shifted closer to the arsenic atoms while the electrons of the bonds along [110] are shifted closer to the gallium. This effect is responsible for the anisotropy measured in RAS.

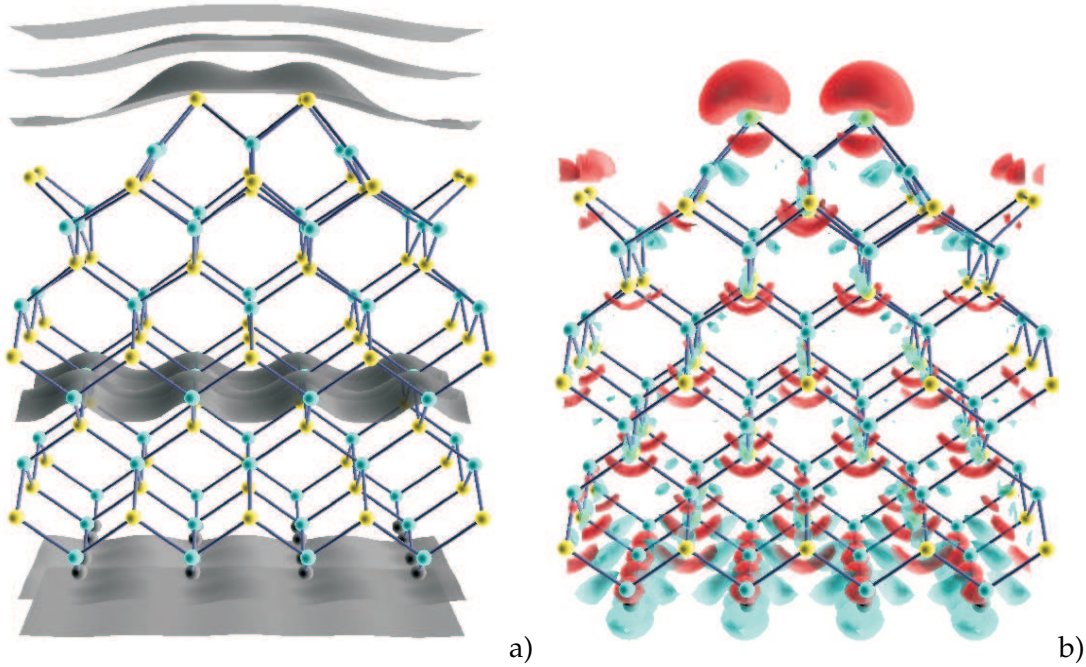

a) b)

Figure 5.4: *Electrostatic potential ρ at a GaAs (001) β2(2×4) surface (a) and the corresponding electron density* transfer *(b) induced by an electric field of* 0.15 *V/nm. The empty circles represent Ga atoms. Pictures from W.G. Schmidt (private communication and [62]).*

5.4 Doping and RAS – the linear electro-optic effect

The propagation of light in a crystal along the principal dielectric axes x_1, x_2, x_3 is fully described by the index ellipsoid:

$$\frac{x_1^2}{\hat{n}_1^2} + \frac{x_2^2}{\hat{n}_2^2} + \frac{x_3^2}{\hat{n}_3^2} = 1 \quad . \tag{5.3}$$

In the presence of an electric field, (5.3) takes the form [64]

$$\left(\frac{1}{\hat{n}^2}\right)_1 x_1^2 + \left(\frac{1}{\hat{n}^2}\right)_2 x_2^2 + \left(\frac{1}{\hat{n}^2}\right)_3 x_3^2 + 2\left(\frac{1}{\hat{n}^2}\right)_4 x_2 x_3 + 2\left(\frac{1}{\hat{n}^2}\right)_5 x_3 x_1 + 2\left(\frac{1}{\hat{n}^2}\right)_6 x_1 x_2 = 1 \quad . \tag{5.4}$$

In the general case (x_i $/\!\!/$ principal dielectric axes), the refractive indices are described by a two-dimensional matrix

$$B_{ij} := \left(\frac{1}{\epsilon}\right)_{ij} = \left(\frac{1}{\hat{n}^2}\right)_{ij} \quad , \tag{5.5}$$

the so-called optical indicatrix or index tensor. The connection to the formalism of (5.4) can be made by using a contracted notation:

$$B_{ii} = B_i, 2B_{23} = B_4, 2B_{31} = B_5, 2B_{12} = B_6 \quad . \tag{5.6}$$

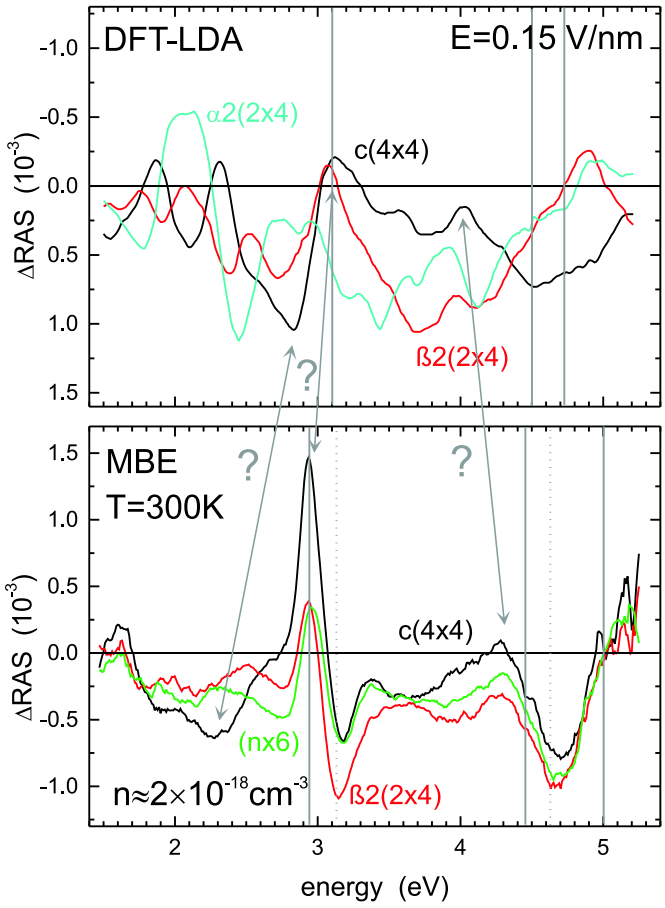

Figure 5.5: *Comparison of the DFT-LDA results from [62] (GaAs) to experiment [63]. The quantity ΔRAS is defined as the difference between the RAS spectrum with applied field (doped) and the spectrum without electric field (undoped). The band gap was corrected by a scissor operator. The solid vertical lines correspond to the E_1, E_0' and E_2 critical points. The dotted vertical lines in the lower graph mark the $E_1 + \Delta_1$ and the $E_0' + \Delta_0'$ transitions. The spin-orbit splitting was not considered in the calculation, therefore no feature corresponding to the $E_1 + \Delta_1$ transition is visible.*

The influence of the doping concentration on the RAS signal can be explained by electro-optic effects: An electric field **E** applied to a crystal without inversion symmetry changes its optical properties, i.e. its index tensor B_{ij}. Neglecting higher orders, this change can be described as

$$\Delta B_{ij} = B_{ij}(\mathbf{E}) - B_{ij}(0) = \sum_k d_{ijk} E_k + \sum_{k,l} D_{ijkl} E_k E_l \quad . \tag{5.7}$$

The first term describes the linear electro-optic (or *Pockels*) effect, the second one the quadratic electro-optic effect, also called the electro-optic *Kerr* effect. For ease of use,

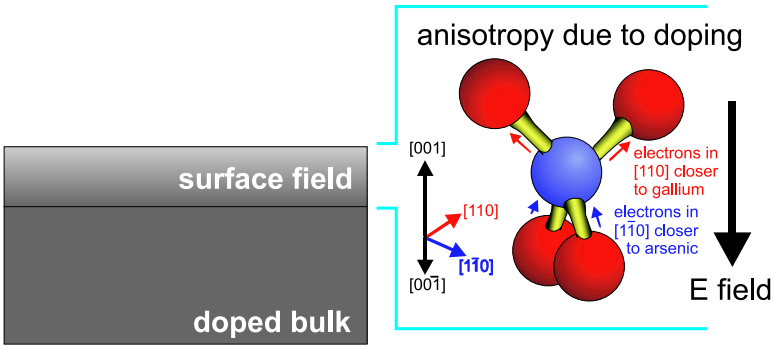

Figure 5.6: *Field-induced shift of the atoms as a handwaving explanation for the occurrence of an optical anisotropy.*

the common abbreviation LEO for the linear effect is used in this text. The orders of magnitude of both effects are $\Delta n/E \approx 10^{-11} \ldots 10^{-12}\,\mathrm{m/V}$ for the LEO[1] and $\Delta n/E^2 \approx 10^{-19}\,\mathrm{m^2/V^2}$ for the quadratic effect [10]. From these numbers it becomes clear why the quadratic effect is dominated by the LEO. This does not hold for centrosymmetric crystals where the LEO is not present due to symmetry reasons.

The LEO in the contracted notation can be written as

$$\Delta B_i = \Delta\left(\frac{1}{\hat{n}^2}\right)_i = \sum_{j=1}^{3} d_{ij} E_j \quad (i \in 1 \ldots 6), \tag{5.8}$$

where d_{ij} is the (linear) electro-optic tensor. In matrix form, (5.8) reads

$$\begin{pmatrix} \Delta B_1 \\ \Delta B_2 \\ \Delta B_3 \\ \Delta B_4 \\ \Delta B_5 \\ \Delta B_6 \end{pmatrix} = \begin{pmatrix} \Delta B_{11} \\ \Delta B_{22} \\ \Delta B_{33} \\ 2\Delta B_{23} \\ 2\Delta B_{31} \\ 2\Delta B_{12} \end{pmatrix} = \begin{pmatrix} d_{11} & d_{12} & d_{13} \\ d_{21} & d_{22} & d_{23} \\ d_{31} & d_{32} & d_{33} \\ d_{41} & d_{42} & d_{43} \\ d_{51} & d_{52} & d_{53} \\ d_{61} & d_{62} & d_{63} \end{pmatrix} \begin{pmatrix} E_1 \\ E_2 \\ E_3 \end{pmatrix} \quad . \tag{5.9}$$

Especially in cubic crystals of the $\bar{4}3m$ symmetry group (e.g. GaAs, InP, ...), which are of particular interest in this work, the electro-optic tensor has a very simple form [64]: all elements are zero, except for $d_{41} = d_{52} = d_{63}$:

$$\begin{pmatrix} 0 & 0 & 0 \\ 0 & 0 & 0 \\ 0 & 0 & 0 \\ d_{41} & 0 & 0 \\ 0 & d_{41} & 0 \\ 0 & 0 & d_{41} \end{pmatrix} \quad . \tag{5.10}$$

If we additionally assume $E_1 = E_2 = 0, E_3 \neq 0$ for the electric field, (5.9) reduces to

$$\Delta B_6 = \Delta\left(\frac{1}{\hat{n}^2}\right)_6 = d_{63} E_3 \quad . \tag{5.11}$$

[1] Order of magnitude given for typical III-V semiconductors.

Substance	λ (μm)	d_{41} (10^{-12} m/V)	Source
CdTe	1.0	4.5	[66]
GaAs	0.9	1.1	[64]
	1.06	1.51, 1.8	[66]
	10.6	1.51	[66]
GaP	0.55 – 1.3	0.76 – 1.0*	[66]
InP	1.06	1.32, 1.45	[66]
ZnS		2.0	[66]
ZnSe		2.0	[66]
ZnTe	0.59	4.51	[66]
	0.69	3.97	[66]

*Most tabulated values are around 1.0.

Table 5.2: *Low-frequency linear electro-optic coefficients d_{41} for some semiconductors of $\bar{4}3m$ symmetry. The values are given for room temperature and without sign. If no wavelength is given, the value is correct for wavelengths around 550 nm. The frequency dependence of d_{41} was fitted from literature values for ZnTe and GaP in [67].*

In the long notation (cf. equation 5.6), this can be written as

$$\Delta B_{12} = \Delta\left(\frac{1}{\hat{n}^2}\right)_{12} = \frac{1}{2} d_{123} E_3 \quad . \tag{5.12}$$

This means that an electric field along the $z-$axis in a crystal of $\bar{4}3m$ symmetry changes the optical properties along x and y, but not along z. This also means that doping (producing electric fields along the depth of the sample) should be detectable by RAS, because the optical properties along the axes parallel to the surface are changed.

The linear electro-optic coefficient d_{41} is tabulated for some fcc semiconductors in tab. 5.2. Unfortunately, these data are only known for certain wavelengths, usually below the band gap. Acosta-Ortiz has determined the linear electro-optic coefficient P_{44} of GaAs for wavelengths from 380 to 450 nm [65]. This coefficient connects the normalised change in reflectance $\Delta R/R$ (not to be confused with RAS!) to the electric field: $\Delta R/R \sim P_{44} E$. Thus the coefficient P_{44} cannot be directly compared to d_{41}, although they have the same units and are of similar order of magnitude. To connect

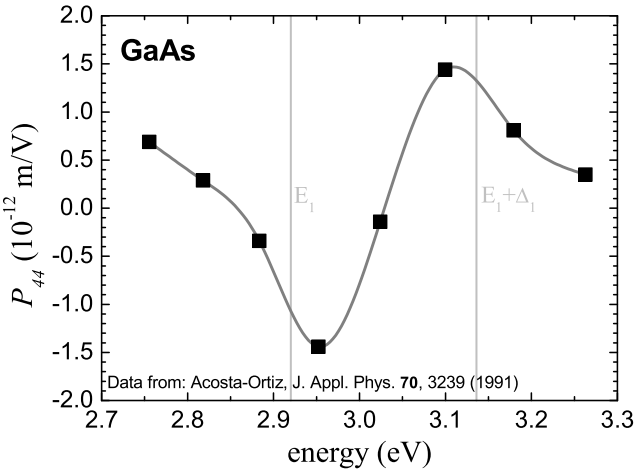

Figure 5.7: *Low-frequency linear electro-optic coefficient P_{44} of GaAs. Data are taken from [65]. A connecting spline is drawn between the data points as a guide to the eye.*

a change in the optical indicatrix with the RAS signal, one of the two orthogonal axes on the sample surface with complex reflectance r is considered:

$$\frac{1}{2}\Delta\mathrm{RAS} = \frac{r(E) - r(0)}{\langle r\rangle} = \frac{\frac{\hat{n}(E)-1}{\hat{n}(E)+1} - \frac{\hat{n}(0)-1}{\hat{n}(0)+1}}{\frac{\langle\hat{n}\rangle-1}{\langle\hat{n}\rangle+1}} \tag{5.13}$$

Since the changes in n due to the electric field are small ($\hat{n}(E) \approx \hat{n}(0) \approx \langle\hat{n}\rangle$), this expression can be further simplified to

$$\frac{1}{2}\Delta\mathrm{RAS} \approx 2\frac{\hat{n}(E) - \hat{n}(0)}{\langle\hat{n}\rangle^2 - 1} = 2\frac{\Delta\hat{n}}{\langle\hat{n}\rangle^2 - 1} \tag{5.14}$$

For the optical index tensor element from (5.12) it follows that

$$\begin{aligned} \Delta B_6 &= d_{63}E_3 \\ = \Delta B_{12} &= \frac{1}{2}d_{123}E_3 \\ &= \Delta\left(\frac{1}{\hat{n}^2}\right)_{12} = \frac{1}{\hat{n}^2(E)} - \frac{1}{\hat{n}^2(0)} \\ &= \frac{\hat{n}^2(0) - \hat{n}^2(E)}{\hat{n}^4} = \frac{(\hat{n}(0) + \hat{n}(E))(\hat{n}(0) - \hat{n}(E))}{\hat{n}^4} \\ &\approx \frac{2\hat{n}(\hat{n}(0) - \hat{n}(E))}{\hat{n}^4} = -2\frac{\Delta\hat{n}}{\hat{n}^3} \quad . \end{aligned} \tag{5.15}$$

Therefore

$$\Delta\hat{n} = -\frac{\Delta B_{12}\hat{n}^3}{2} = -\frac{d_{63}E_3\hat{n}^3}{2} \quad . \tag{5.16}$$

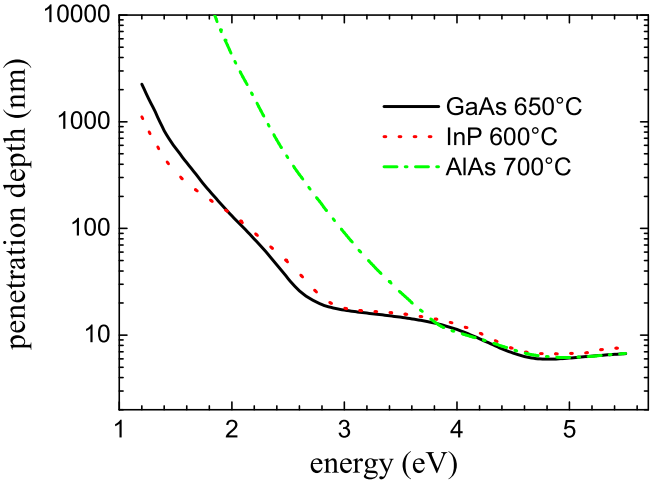

Figure 5.8: *Penetration depths for three typical III-V semiconductors at growth temperature.*

Using (5.14) we have

$$\frac{1}{2}\Delta\mathrm{RAS} \approx -\frac{\Delta B_{12}\hat{n}^3}{\hat{n}^2-1} \approx -\frac{d_{63}E_3\hat{n}^3}{\hat{n}^2-1} \quad . \tag{5.17}$$

Thus the change of the RAS signal scales linear with the electric field: $\Delta\mathrm{RAS} \sim E_3$. Changing the direction of the electric field (n- and p-doping) also inverts the effect on the RAS signal, which has been observed experimentally [40, 56, 68].

To obtain a quantitative information, i.e. to calculate the influence of the LEO on the RAS signal, it must be considered that the electric field of the probing light decreases exponentially with depth z (Beer's law):

$$E_{\mathrm{light}}(z) = \hat{E}_{\mathrm{light}} e^{-\frac{z}{z_p}} \quad , \tag{5.18}$$

where z_p is the penetration depth, the inverse of the absorption coefficient. The penetration depths of some typical III-V semiconductors at growth temperature as a function of photon energy is given in fig. 5.8. The contribution of the LEO to the RAS signal can be written as the product of the Schottky field (5.1) and a weighting factor that describes the sampling behaviour of the RAS light – the light field from (5.18). This product is called the *integrated surface field* in [60]. It does not mean that both electric fields interact directly. Integration over the sample depth gives:

$$I_{\mathrm{LEO}} = \frac{1}{z_p}\int_0^{z_d} E_{\mathrm{Schottky}}(z)E_{\mathrm{light}}(z)dz \quad . \tag{5.19}$$

The normalisation factor is required to fulfill the condition

$$\int_0^\infty e^{-\frac{z}{z_p}} dz = z_p \quad . \tag{5.20}$$

Further treatment of (5.19) yields

$$\begin{aligned} I_{\mathrm{LEO}} &= \frac{\hat{E}_{\mathrm{light}}}{z_p} \sqrt{\frac{2eN\phi_0}{\epsilon_0\epsilon}} \int_0^{z_d} \left(1 - \frac{z}{z_d}\right) e^{-\frac{z}{z_p}} dz \\ &= \frac{\hat{E}_{\mathrm{light}}}{z_p} \sqrt{\frac{2eN\phi_0}{\epsilon_0\epsilon}} z_p \left\{1 + \frac{z_p}{z_d}\left(e^{-\frac{z_d}{z_p}} - 1\right)\right\} \\ &= \hat{E}_{\mathrm{light}} \sqrt{\frac{2eN\phi_0}{\epsilon_0\epsilon}} \left\{1 + \frac{z_p}{z_d}\left(e^{-\frac{z_d}{z_p}} - 1\right)\right\} \quad . \end{aligned} \tag{5.21}$$

Case 1: Penetration depth $z_p \ll$ depletion width z_d When the penetration depth of the light is much smaller than the depletion width z_d, the light is essentially probing the constant field at the sample surface. The factor in braces in (5.21) approaches 1 as $\frac{z_p}{z_d} \to 0$. Thus

$$I_{\mathrm{LEO}} \sim \sqrt{N} \quad . \tag{5.22}$$

This formula can be used for small carrier concentrations (large z_d) or small penetration depths (e.g. at high photon energies).

Case 2: Penetration depth z_p and depletion width z_d have similar orders of magnitude In the relevant doping region the dependence of the RAS signal on the doping level is more complex than in the first case. For various RAS measurements with known doping concentration, a fit of (5.21) can be performed [63]. Fitting parameters are the Fermi level pinning ϕ_0 and a proportionality constant between ΔRAS and I_{LEO}. For measurements at growth temperatures the high-temperature dielectric function must also be known. The graph of $\Delta\mathrm{RAS}(\log N)$ is an S-shaped curve as shown in fig. 5.9. In the intermediate doping regime (typically mid-10^{16} – mid-$10^{18}\,\mathrm{cm}^{-3}$) the change of ΔRAS is proportional to the logarithm of the doping concentration.

Since the fitting of (5.21) involves too many quantities, for applications it is often sufficient to assume a linear relationship between $\log N$ and ΔRAS.

5.5 Determination of doping concentration with multichannel RAS

As was discussed in sec. 5.3, the determination of dopant concentration can be made via the LEO features near critical points of the band structure or via the observed overall shift of RAS spectra (cf. fig. 5.3). This is also possible with multichannel RAS.

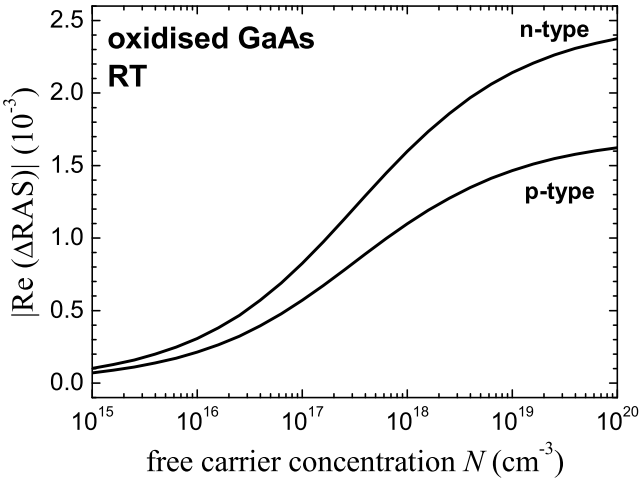

Figure 5.9: *Dependence of the change of the RAS signal on the free carrier concentration for oxidised GaAs at room temperature. The penetration depth of the light z_p was set to 20 nm (corresponds to the E_1 critical point). The fitted values for ϕ_0 and the proportionality constant were taken from [63].*

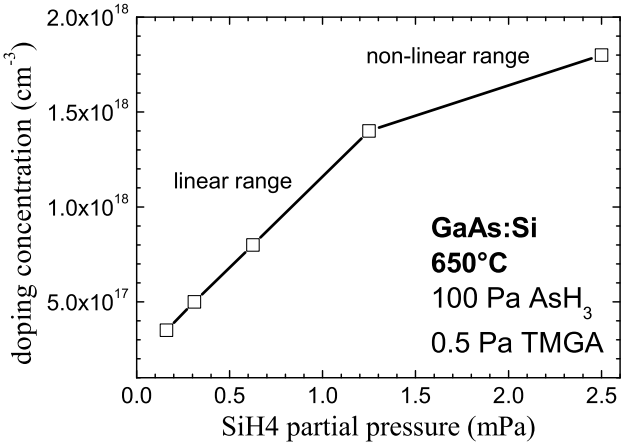

Figure 5.10: *Influence of silane partial pressure on the concentration of free carriers as determined by C-V profiling.*

Thick layers (570 nm) of GaAs:Si were grown at 650°C using 100 Pa AsH_3, 0.5 Pa TMGa and SiH_4 in the range of 0.16 – 2.5 mPa. The doping concentration was determined *ex situ* with C-V profiling. The relation between the SiH_4 partial pressure and the concentration of free carriers is shown in fig. 5.10. Up to a partial pressure of 1.25mPa (corresponding to a SiH_4/Ga ratio of 0.25%), the correlation is linear. Somewhere above this value saturation occurs – not all supplied Si can be incorporated. The spectra in fig. 5.11a were measured with multichannel RAS (8 channels) after the

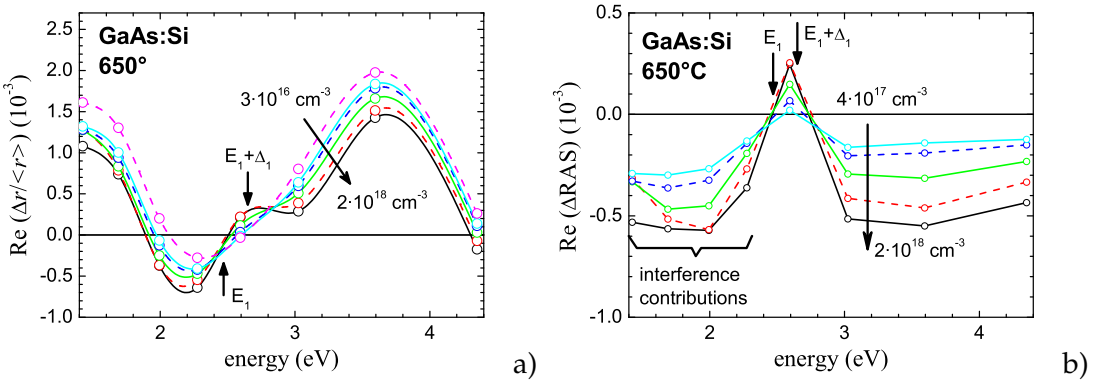

Figure 5.11: *Influence of doping of GaAs with silane at 650°C on the multichannel RAS spectra. The left graph (a) shows the spectra and the right one (b) the difference to the spectrum of the nominally undoped sample.*

growth of each layer. With increasing doping concentration, the spectra show an offset towards negative values. Additionally a derivative-like feature near the $E_1/E_1 + \Delta_1$ critical points is formed (cf. fig. 5.7). The corresponding difference spectra (spectrum of doped GaAs minus spectrum of undoped GaAs) are given in fig. 5.11b.

In both graphs of fig. 5.11 the offset of the spectra in the range $1.4 - 2\,\text{eV}$ is non-uniform and seems to be disturbed somehow. What at first was considered to be some kind of error the measurement later turned out to be a very interesting and important effect: the interference of the RAS signal at the interface between two layers of different doping concentration.

Although this effect reduces the accuracy of the offset determination (less number of channels with utilisable data), it can be employed to determine a growth rate in homoepitaxy and to determine the difference in carrier concentration. This topic is discussed in detail in sec. 6.

To analyse the influence of the free carrier concentration on the RAS spectrum, one must find a way to convert the two effects (derivative-like feature and general offset) into numbers. First, the difference to the spectrum of the nominally undoped sample is calculated. The quantity $\text{RAS}_{\text{offset}}$ is then defined as the mean value of the channels 6 and 7 of the difference spectrum (channel definition valid for the case of the 8 channel detector).

For the derivative-like feature in the vicinity of the $E_1/E_1 + \Delta_1$ critical point, the values of channel 3 and channel 6 are connected by a line and the difference between the value of channel 5 (2.6 eV) and the line is calculated and is given the name δRAS. These definitions are visualised in fig. 5.12. When using the 16 channel detector, the channel numbers in the definitions must be adapted accordingly.

The correlation of both δRAS and $\Delta\text{RAS}_{\text{offset}}$ with the doping concentration (logarithmic scale!) is given in fig. 5.13. From the linear fits in both graphs it is obvious that both δRAS and $\Delta\text{RAS}_{\text{offset}}$ scale linearly with the logarithm of the doping concentration. For the determination of the doping level during epitaxy it would be necessary

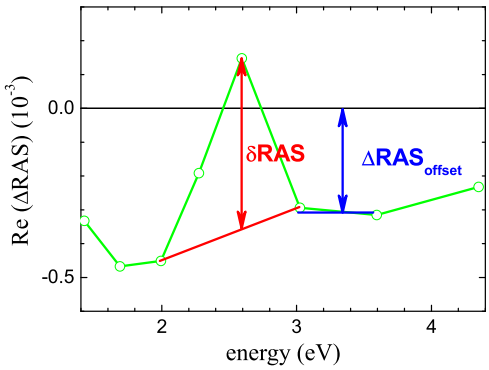

Figure 5.12: *Definition of δRAS and $\Delta RAS_{\text{offset}}$ for doping of GaAs (measured with 8 channels).*

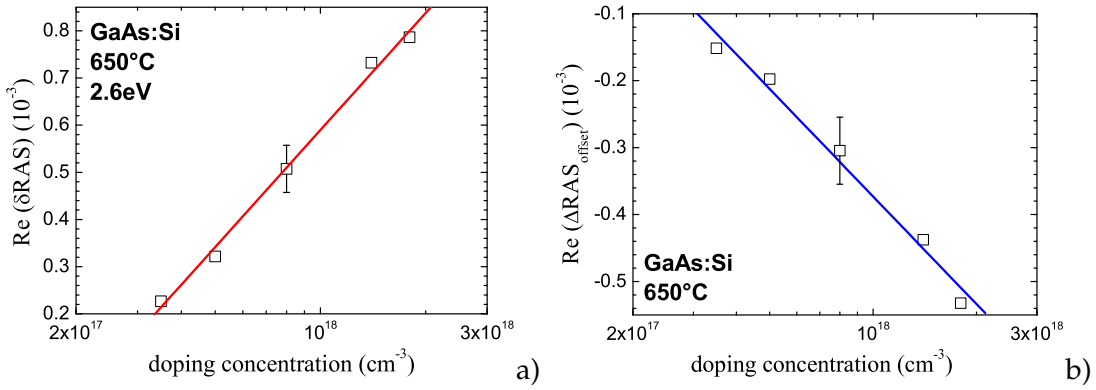

Figure 5.13: *Change of the RAS signal with the logarithm of the free carrier concentration: (a) δRAS (peak at 2.6 eV) and (b) $\Delta RAS_{\text{offset}}$. The definition of the two quantities δRAS and $\Delta RAS_{\text{offset}}$ is given in fig. 5.12. The lines represent linear fits of the data points.*

to determine the parameters of the linear function for a certain material-dopant combination (here: GaAs:Si) and for a set of growth temperatures. With such a database it would be possible to control the dopant concentration during growth with sub-second temporal resolution.

In principle, the calculation would also work without difference spectra: The feature near the $E_1/E_1+\Delta_1$ critical points could also be directly evaluated from the spectra (fig. 5.11a). This would also mean that the influence of drift on the measurement is cancelled. After calibration, only one measurement is necessary to determine the doping concentration. The drawback is that when a multichannel RAS is used, care must be taken that the corresponding spectral channels have the same sensitivity and that nonlinear effects in the signal processing are small (or at least the same for all channels).

6. Doping-induced RAS oscillations

While the influence of doping on the RAS spectrum has been thoroughly investigated before, an interesting and important effect in the temporal behaviour of the RAS signal was somehow overlooked: doping-induced thickness oscillations.

While they were first considered as an error in the multichannel RAS data (cf. section 5.5), I later realised that they can be very useful to get a thickness information in homoepitaxy. During growth of layers with different dopant concentration one observes clear oscillations in the RAS signal $\Delta r/\langle r\rangle$, but not in the reflectance signal $\langle r\rangle$. These oscillations occur at photon energies near the band gap, where the penetration depth is large.

Fig. 6.1 shows reflectance $\langle r\rangle$ (upper part) and RAS (lower part) transients recorded simultaneously (multichannel RAS) during growth of undoped GaAs on a doped GaAs:Si substrate (5×10^{18} cm^{-3}). The RAS transients show a clear oscillatory behavior

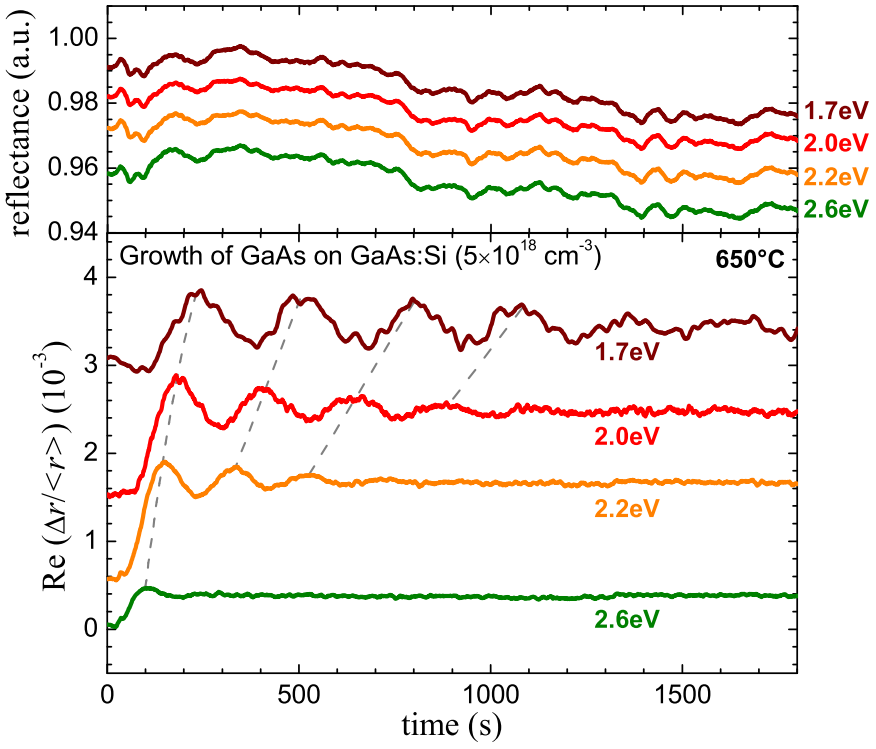

Figure 6.1: *Reflectance $\langle r\rangle$ and RAS transients recorded simultaneously during growth of GaAs on GaAs:Si (5×10^{18} cm^{-3}). The transients are shifted vertically for better visibility. The grey broken lines indicate the wavelength dependence of the oscillations.*

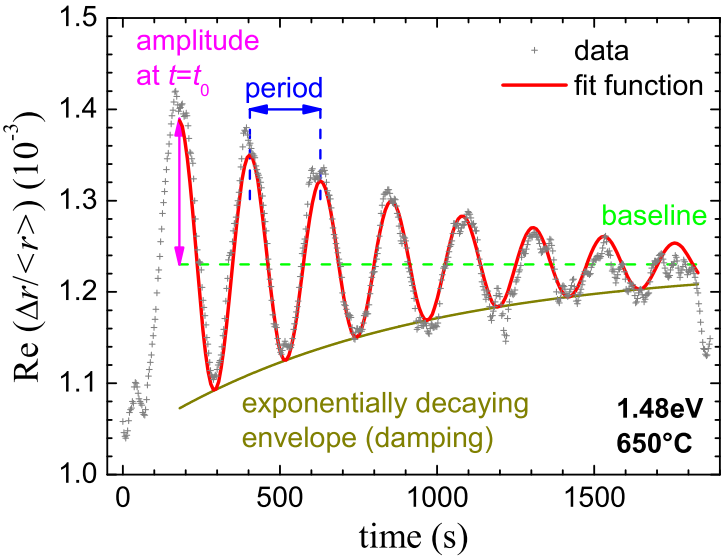

Figure 6.2: *Example for the fitting of a monolayer oscillation with (6.1). The datapoints correspond to a measurement shown in fig. 6.12 (layer 1).*

which is not visible in the reflectance signal $\langle r \rangle$. It it worth noting that the period of these oscillations is not comparable to RAS/RHEED monolayer growth oscillations [31]. These monolayer oscillations occur on a time scale of seconds. Moreover, they cannot be observed at such a high temperature.

For shorter wavelengths, corresponding to smaller penetration depths (cf. fig. 5.8) of the light, the oscillations in the RAS transients damp out faster. In this aspect, the RAS oscillations behave similarly to Fabry-Pérot interference oscillations. On the other hand, the features in the reflectance transients are similar at all photon energies and thus are most likely due to noise of the light source and small variations of the sample position or similar external effects. Therefore the oscillations in the RAS signal cannot be explained by reflectance (or DC signal) oscillations.

The RAS transients can be fitted by an exponentially damped cosine function to determine the baseline, the amplitude, the period and the damping (fig. 6.2). The fit formula was

$$\mathrm{Re}\left(\frac{\Delta r}{r}\right) = \mathrm{Amplitude} \times \exp\left(-\frac{t-t_0}{\mathrm{damping}}\right) \cos\left(\frac{2\pi(t-t_0)}{t_\mathrm{p}}\right) + \mathrm{baseline} \quad . \tag{6.1}$$

From the period t_p the growth rate G can be calculated using the equation for Fabry-Pérot interference oscillations:

$$G = \frac{\lambda}{2nt_\mathrm{p}} \tag{6.2}$$

where λ is the wavelength of the probing light and n is the refractive index of the growing layer at growth temperature. From the fitting of the three transients at 1.7, 2.0 and 2.2 eV in fig. 6.1 the growth rate was determined to 1.156, 1.141 and 1.170 μm/h,

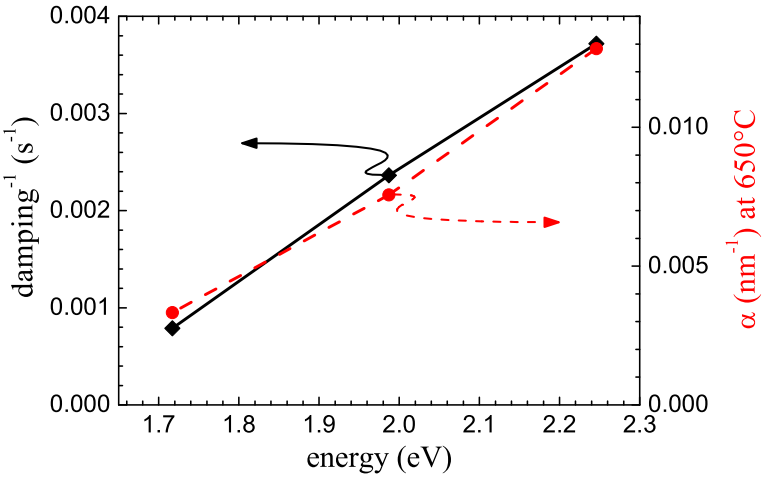

Figure 6.3: *Comparison of the inverse damping coefficient (left axis) obtained from fitting three transients (1.7, 2.0 and 2.2 eV) of fig. 6.1 to the absorption coefficient α at growth temperature (right axis).*

respectively. These values are very much similar (as expected, because it should be the same growth rate) and agree well with the growth rate obtained *ex situ* (weighing, C-V profiling) and *in situ* from monolayer growth oscillations (at lower temperature). The reciprocal damping obtained from the fit (6.1) is proportional to the absorption coefficient α at growth temperature (fig. 6.3). This is another indication that the origin of these oscillations is somewhat similar to Fabry-Pérot oscillations. This requires a thorough investigation, for which the first step is done by setting up an appropriate optical model in the following section.

6.1 Theoretical description of doping-induced thickness oscillations

Doping oscillations can be described by means of an optical four-phase model (fig. 6.4). It consists of an ambient (phase 0, air or vacuum) with refractive index $n_0 = 1$ and a growing layer (phase 1) on top of the semi-infinite substrate or buffer layer (phase 3). Between layer 1 and layer 3 a difference in doping concentration is assumed, causing an electric field (phase 2). This region is the only anisotropic layer in this model. This means that the surface anisotropy (interface between phases 0 and 1) is neglected in this model. The complex dielectric functions are written with a hat ($\hat{\epsilon}_i$) to avoid confusion with the usual writing of ϵ_1 and ϵ_2 as real and imaginary part of ϵ. The ansatz for the following calculation is taken from [69]. The RAS signal is

$$\frac{\Delta r}{r} = \frac{r_\alpha^{(4)} - r_\beta^{(4)}}{\frac{1}{2}\left(r_\alpha^{(4)} + r_\beta^{(4)}\right)}, \tag{6.3}$$

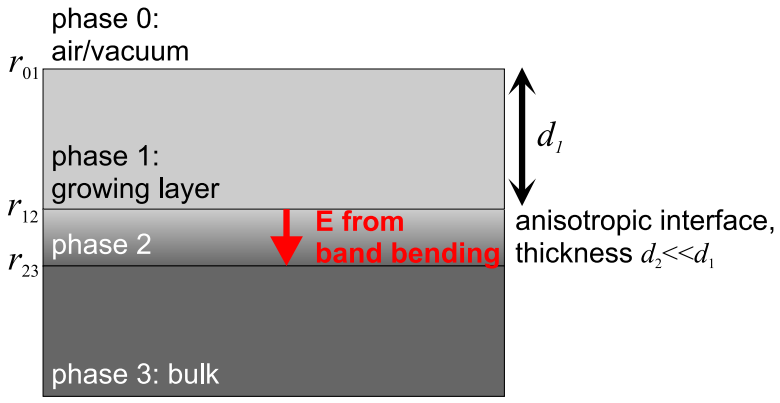

Figure 6.4: *Four-phase model for the calculation of doping oscillations. Layer 1 is the growing layer and layer 3 represents the semi-infinite bulk or buffer. Both have a different dopant concentration. The only anisotropy is induced in layer 2 by the electric field via the LEO.*

where $r_\alpha^{(4)}$ and $r_\beta^{(4)}$ are the Fresnel coefficients of the 4-phase model. The dielectric functions of the ith layer are $\hat{\epsilon}_{i\alpha}$ and $\hat{\epsilon}_{i\beta}$. For layers 0, 1 and 3, the dielectric functions along directions α and β are equal. The only anisotropic contribution comes from layer 2 where $\hat{\epsilon}_{2\alpha} \approx \hat{\epsilon}_{2\beta}$. We can thus expand the enumerator of (6.3) and keep only linear terms in $\Delta\hat{\epsilon}_2 = \hat{\epsilon}_{2\alpha} - \hat{\epsilon}_{2\beta}$:

$$r_\alpha^{(4)} - r_\beta^{(4)} = \frac{\partial r^{(4)}}{\partial \hat{\epsilon}_2} \Delta\hat{\epsilon}_2 \quad . \tag{6.4}$$

The assumption of a constant $\Delta\hat{\epsilon}_2$ is already a simplification, because the field-induced anisotropy of the dielectric function is proportional to the field, and the electric field is assumed to decrease linearly in the space-charge layer (fig. 5.1 and (5.1)).

According to [10], the Fresnel coefficient of a 4-phase model is given by (modified Airy formula)

$$r^{(4)} = \frac{r_{01} + r_{12}e^{i2\beta_1} + \left(r_{01}r_{12} + e^{i2\beta_1}\right) r_{23}e^{i2\beta_2}}{1 + r_{01}r_{12}e^{i2\beta_1} + \left(r_{12} + r_{01}e^{i2\beta_1}\right) r_{23}e^{i2\beta_2}} \quad , \tag{6.5}$$

where r_{ij} is the corresponding Fresnel coefficient for the interface between layer i and layer j. For perpendicular incidence, this can be written as

$$r_{ij} = \frac{\sqrt{\hat{\epsilon}_i} - \sqrt{\hat{\epsilon}_j}}{\sqrt{\hat{\epsilon}_i} + \sqrt{\hat{\epsilon}_j}} = \frac{\hat{n}_i - \hat{n}_j}{\hat{n}_i + \hat{n}_j} \quad . \tag{6.6}$$

The phase factors β_i are (perpendicular incidence assumed)

$$\beta_i = \frac{2\pi d_i \sqrt{\hat{\epsilon}_i}}{\lambda} = \frac{2\pi d_i \hat{n}_i}{\lambda} \quad , \tag{6.7}$$

where d_i is the layer thickness of layer i and λ is the wavelength. The derivative of $r^{(4)}$ with respect to $\hat{\epsilon}_2$ can be written as

$$\frac{\partial r^{(4)}}{\partial \hat{\epsilon}_2} = \frac{\partial r^{(4)}}{\partial r_{12}} \frac{\partial r_{12}}{\partial \hat{\epsilon}_2} + \frac{\partial r^{(4)}}{\partial r_{23}} \frac{\partial r_{23}}{\partial \hat{\epsilon}_2} + \frac{\partial r^{(4)}}{\partial \beta_2} \frac{\partial \beta_2}{\partial \hat{\epsilon}_2} \quad . \tag{6.8}$$

The calculation yields

$$\begin{aligned}\frac{\partial r^{(4)}}{\partial \hat{\epsilon}_2} =& \frac{\left(1-r_{01}^2\right)e^{i2\beta_1}}{\left(1+r_{01}r_{12}e^{i2\beta_1}+\left(r_{12}+r_{01}e^{i2\beta_1}\right)r_{23}e^{i2\beta_2}\right)^2}\times \\ &\times\left(\left(1-r_{23}^2e^{i4\beta_2}\right)\frac{\partial r_{12}}{\partial \hat{\epsilon}_2}+e^{i2\beta_2}\left(1-r_{12}^2\right)\frac{\partial r_{23}}{\partial \hat{\epsilon}_2}+2ir_{23}e^{i2\beta_2}\left(1-r_{12}^2\right)\frac{\partial \beta_2}{\partial \hat{\epsilon}_2}\right) \quad .\end{aligned} \tag{6.9}$$

The expression for $r^{(4)}$ (6.5) can be greatly simplified because the reflectance of the interfaces in the bulk is extremely small ($r_{12} \approx 0$ and $r_{23} \approx 0$):

$$r^{(4)}(r_{12} \approx 0, r_{23} \approx 0) = r_{01} \quad . \tag{6.10}$$

For the derivative (6.9) the same simplification can be applied:

$$\frac{\partial r^{(4)}}{\partial \hat{\epsilon}_2}(r_{12} \approx 0, r_{23} \approx 0) = \left(1-r_{01}^2\right)e^{i2\beta_1}\left(\frac{\partial r_{12}}{\partial \hat{\epsilon}_2}+e^{i2\beta_2}\frac{\partial r_{23}}{\partial \hat{\epsilon}_2}\right) \quad . \tag{6.11}$$

Combining (6.10) and (6.11) one obtains

$$\begin{aligned}\frac{\Delta r}{r} &= \frac{1}{r^{(4)}}\frac{\partial r^{(4)}}{\partial \hat{\epsilon}_2}\Delta\hat{\epsilon}_2 \\ &= \frac{\left(1-r_{01}^2\right)e^{i2\beta_1}}{r_{01}}\left(\frac{\partial r_{12}}{\partial \hat{\epsilon}_2}+e^{i2\beta_2}\frac{\partial r_{23}}{\partial \hat{\epsilon}_2}\right)\Delta\hat{\epsilon}_2 \\ &= \frac{\left(1-r_{01}^2\right)e^{i2\beta_1}}{r_{01}}\left(-\frac{\sqrt{\hat{\epsilon}_1}}{\sqrt{\hat{\epsilon}_2}\left(\sqrt{\hat{\epsilon}_1}+\sqrt{\hat{\epsilon}_2}\right)^2}-e^{i2\beta_2}\frac{\sqrt{\hat{\epsilon}_2}}{\sqrt{\hat{\epsilon}_3}\left(\sqrt{\hat{\epsilon}_2}+\sqrt{\hat{\epsilon}_3}\right)^2}\right)\Delta\hat{\epsilon}_2\end{aligned} \tag{6.12}$$

We can now make use of the fact that in homoepitaxy the three dielectric functions 1 − 3 of the 4 phase model are virtually identical ($\hat{\epsilon}_1 = \hat{\epsilon}_2 = \hat{\epsilon}_3$). Only $\hat{\epsilon}_1$ or $\hat{n}_1$ is used from now on.

$$\begin{aligned}\frac{\Delta r}{r} &= \frac{\left(1-r_{01}^2\right)e^{i2\beta_1}}{r_{01}}\left(-\frac{1}{4\hat{\epsilon}_1}-e^{i2\beta_2}\frac{1}{4\hat{\epsilon}_1}\right)\Delta\hat{\epsilon}_2 \\ &= -\frac{\left(1-r_{01}^2\right)e^{i2\beta_1}}{4r_{01}\hat{\epsilon}_1}\left(1+e^{i2\beta_2}\right)\Delta\hat{\epsilon}_2\end{aligned} \tag{6.13}$$

Expressing r_{01} as a function of the refractive indices (6.6) and using $\hat{n}_0 = 1, \hat{\epsilon}_1 = \hat{n}_1^2$ one obtains:

$$\frac{\Delta r}{r} = \frac{e^{i2\beta_1}}{\hat{n}_1\left(\hat{n}_1^2-1\right)}\left(1+e^{i2\beta_2}\right)\Delta\hat{\epsilon}_2 \quad . \tag{6.14}$$

The phase factors β_i can be expanded using (6.7):

$$\frac{\Delta r}{r} = \frac{1}{\hat{n}_1\left(\hat{n}_1^2-1\right)}\exp\left(\frac{i4\pi d_1\hat{n}_1}{\lambda}\right)\left(1+\exp\left(-\frac{i4\pi d_2\hat{n}_1}{\lambda}\right)\right)\Delta\hat{\epsilon}_2 \quad . \tag{6.15}$$

The minus sign in the argument of the second exponential (phase factor depending on d_2) was inserted to obtain agreement with the numerical simulations in sec. 6.2. It depends on the definition of the anisotropy axes.

We have now derived a rather simple expression for the RAS signal as a function of the thickness d_1 of the growing layer. Input parameters are the complex refractive index $\hat{n}_1$ of the material at growth temperature, the wavelength λ, the thickness of the space charge layer d_2 and the dielectric anisotropy of the space charge layer $\Delta\hat{\epsilon}_2 = \hat{\epsilon}_{2\alpha} - \hat{\epsilon}_{2\beta}$. As can be expected, the RAS signal is proportional to the dielectric anisotropy $\Delta\hat{\epsilon}_2$.

The pre-factor $\left(\hat{n}_1\left(\hat{n}_1^2 - 1\right)\right)^{-1}$ and thus the dielectric properties of the material ($\hat{n}_1 = n_1 + ik_1$) also determine the magnitude of the effect. The largest magnitude of the pre-factor is reached for n_1 close to 1 and small values of k_1.

The factor $\exp\left(\frac{i4\pi d_1 \hat{n}_1}{\lambda}\right)$ describes a damped ($\hat{n}_1$ is complex!) oscillation with period $\lambda/(2\,\mathrm{Re}(\hat{n}_1))$. The factor 2 shows that the growing layer is passed twice. A very small fraction of the light is reflected at r_{12} because of the dielectric anisotropy $\Delta\hat{\epsilon}_2$. For $\Delta\hat{\epsilon}_2 = 0$ no reflection would occur. The reflected light passes d_1 again and interferes with the incoming (polarised) light reflected at r_{01}. Fig. 6.5 illustrates this in the four-phase model.

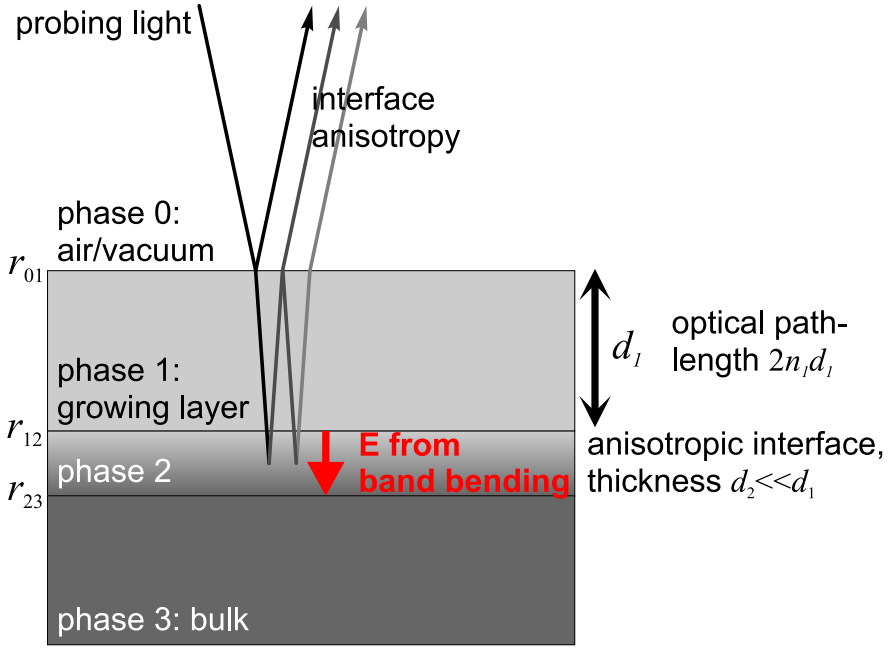

Figure 6.5: *Illustration describing the origin of doping oscillations. The reflectivity of the interface is very small, so that the reflectance modulation is usually below the detection limit of reflectometry. However, the modulation produced by the interference between the anisotropy signal of the interface and the light reflected off the surface can be measured with RAS.*

So far, the surface was assumed to be isotropic. This assumption is somewhat unrealistic because the surface might be anisotropic due to a reconstruction. If the

topmost layer of the sample is doped, there will also be a surface field inducing an anisotropy via the LEO. These influences add a certain anisotropy to the RAS signal (i.e the oscillations are superimposed on the surface anisotropy), but the amplitude of the oscillations might also be changed because the light probing the buried interfaces has already an anisotropic component. The order of magnitude of the contribution from the surface anisotropy can be estimated using (6.5). The anisotropy of r_{01} is $< 10^{-2}$. The influence on all products of r_{12} and r_{23} with r_{01} in (6.5) is therefore below 1%. This means that the surface anisotropy can be treated as an additive component, which justifies the assumption of an isotropic surface in the model. The influence of the reconstruction on the electro-optic bulk properties was studied in detail in [63].

Unfortunately, the two parameters d_2 and $\Delta\hat{\epsilon}_2$ are not known per se. The thickness d_2 can be identified with the depletion width z_d of the Schottky model (5.2) and can be calculated if the doping level N and the Fermi level pinning ϕ_0 are known. The dielectric anisotropy $\Delta\hat{\epsilon}_2$ is more complicated to determine. The change of the optical indicatrix element $\Delta B_6 = \Delta(1/\epsilon)_6$ as a function of electric field is known from (5.15). It is now necessary to go from the change of the indicatrix (inverse ϵ) to the change of ϵ (calculation without indices):

$$\Delta B = \Delta\left(\frac{1}{\epsilon}\right) = \frac{1}{\epsilon(E)} - \frac{1}{\epsilon(0)} \tag{6.16}$$

$$\Delta\left(\frac{1}{\epsilon}\right) + \frac{1}{\epsilon(0)} = \frac{1}{\epsilon(E)} \tag{6.17}$$

$$\frac{1}{\Delta\left(\frac{1}{\epsilon}\right) + \frac{1}{\epsilon(0)}} = \epsilon(E) \tag{6.18}$$

$$\frac{1}{\Delta\left(\frac{1}{\epsilon}\right) + \frac{1}{\epsilon(0)}} - \epsilon(0) = \epsilon(E) - \epsilon(0) = \Delta\epsilon \quad . \tag{6.19}$$

$$\tag{6.20}$$

With known electro-optic coefficient d_{41} we can thus calculate $\Delta\hat{\epsilon}_2$ as

$$\Delta\hat{\epsilon}_2 = \frac{1}{d_{41}\langle E\rangle + \frac{1}{\hat{\epsilon}_1}} - \hat{\epsilon}_1 \quad . \tag{6.21}$$

For the mean electric field $\langle E\rangle$ the value of E at half the depletion width is assumed (cf. fig. 5.1):

$$\langle E\rangle = \frac{1}{2}\sqrt{\frac{2eN\phi_0}{\epsilon_0\hat{\epsilon}_1}} = \sqrt{\frac{eN\phi_0}{2\epsilon_0\hat{\epsilon}_1}} \quad . \tag{6.22}$$

This simplification is only allowed for small depletion layer thickness d_2 because it neglects the variation of the dielectric anisotropy $\Delta\hat{\epsilon}_2$ over the whole depletion layer.

If the doping concentration N is determined by other methods (like Hall measurements or $C-V$ profiling), the only unknown parameter is the Fermi level pinning ϕ_0. This quantity can be obtained by fitting various values of ΔRAS (for different doping concentrations) using (5.21), as is reported in [63] for oxidised surfaces. In this work, the Fermi level pinning of oxidised GaAs samples at room temperature was 0.62 eV for

p-type and 0.64 eV for n-type material, i.e. approximately mid-gap. Other studies determined values around 0.6 – 0.7 eV (above the valence band maximum) for decapped samples [70].

For buried interfaces, as in the case of doping-induced thickness oscillations, this value might be slightly different. It will also be influenced by the high temperature during growth.

In order to compare the analytic model with measured values, we consider an example of growth at 650°C of undoped GaAs on Si-doped GaAs ($N = 5 \times 10^{18}\,\mathrm{cm}^{-3}$). This corresponds to the measurement in fig. 6.1. The growth rate of 1.2 μm/h was determined by fitting a damped oscillation to the measured transients.

Taking $\phi_0 = 0.63\,\mathrm{V}$ (which is only an assumption) and an electro-optic coefficient of $d_{41} = 1.1 \times 10^{-12}\,\mathrm{m/V}$ (cf. tab. 5.2), we calculate RAS transients for three different photon energies as shown in fig. 6.6. The calculated transients were offset in both dimensions (time and anisotropy) to match the measured curves. The decay of the mean value of the measured transients with time is due to drift effects. Considering the simplifications during the derivation of (6.15), the simplicity of the Schottky-model and the uncertainty of d_{41}, the analytic curves agree astonishingly well with the experimental results. Thus it can be concluded that (6.15) can be employed to correctly describe the effect of doping-induced thickness oscillations.

6.2 Numerical simulation of doping osillations

In order to verify (6.15), a comparison with a program for the simulation of optical multilayer systems [71] was undertaken. For testing, a system of undoped on doped GaAs at 600°C was assumed with $d_2 = 25\,\mathrm{nm}$, $E = 1.48\,\mathrm{eV}$ and a growth rate of 1.8 μm/h. For the anisotropy $\Delta\epsilon_2$ a value of $0.003 \times \epsilon(\mathrm{GaAs}, 600°\mathrm{C})$ was assumed. Fig. 6.7 shows the RAS transients (imaginary and real part) during growth of this model system together with the analytical calculation. The period lengths of both the analytic and the numerical calculation are of course the same, while the amplitudes are slightly different – the numerical calculation giving values approx. 15% smaller. The reasons for this deviation are probably the simplifications in the derivation of (6.15). Despite the deviations, the numerical simulation supports the results from the analytical calculation.

The reflectance was also calculated numerically (fig. 6.8). As expected, the modulation at first oscillation is 0.15% of the mean value of the reflectance, which is half of the anisotropy (0.3%). The order of magnitude explains why no reflectance oscillations were measured so far (except for very high doping levels, cf. [72–75]). This leads to the question if the doping oscillations are pronounced enough to be measured with spectroscopic ellipsometry. This was also simulated in AnalysR [71] assuming the same system as before. The angle of incidence was set to $\phi = 65°$. The result of the simulation is shown in fig. 6.9. The ellipsometric parameter $\tan\Psi$ varies in the fourth digit after the comma, and $\cos\Delta$ is already at the threshold of the numerical accuracy of the program – only the fifth digit after the comma changes.

Taking into account the noise level of the *in situ* ellipsometer for measurements of GaAs at 600°C it is not possible to measure the doping-related oscillations with SE.

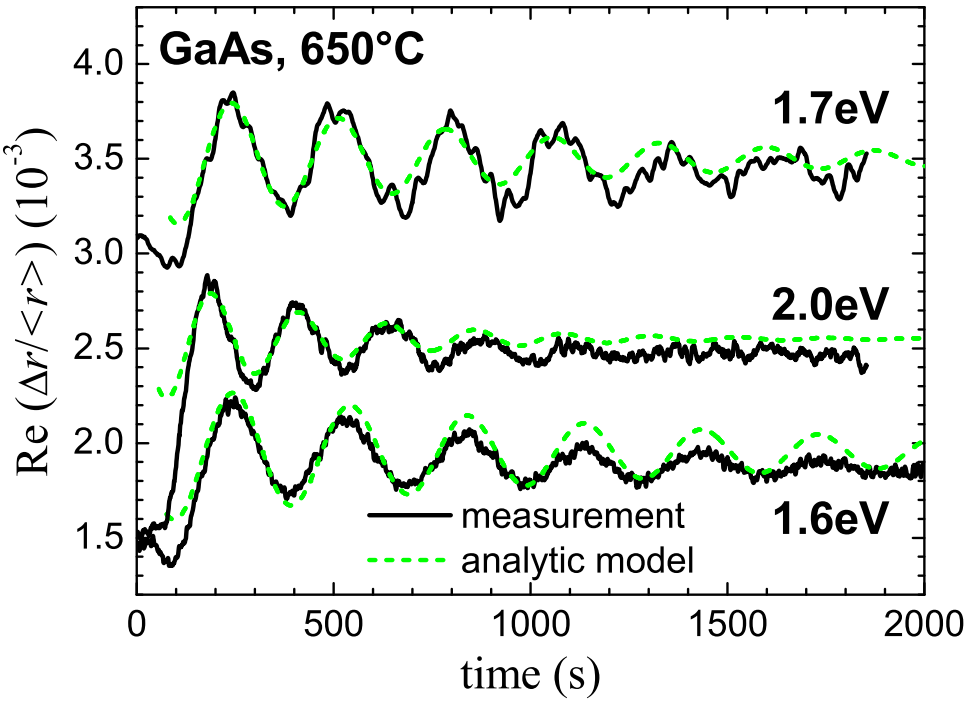

Figure 6.6: *Measured transients of the growth of undoped GaAs on a doped GaAs substrate ($N = 5 \times 10^{18}$ cm^{-3}) compared to transients computed analytically using (6.15). Since the analytic curves do not consider the surface anisotropy they were offset to match the measurement.*

With the present setup, we can only measure $\tan\Psi$ and $\cos\Delta$ with a precision of 3 digits after the comma, which is at least one order of magnitude above the required accuracy.

6.3 Doping oscillations in GaAs

In this section, two layer stacks of doped GaAs (Si-doped and Zn-doped) are studied to demonstrate the possibilities of *in situ* monitoring. The first example is a Si-doped stack with gradually decreasing doping level, the second is a Si-doped stack with alternating doping concentration.

6.3.1 GaAs:Si layer stack

Si is the most widely used and studied source for n-type doping because SiH_4 (silane) was the first doping source commonly available. It does not show any memory effects (no sticking on reactor walls) thus enabling the growth of extremely abrupt doping profiles.

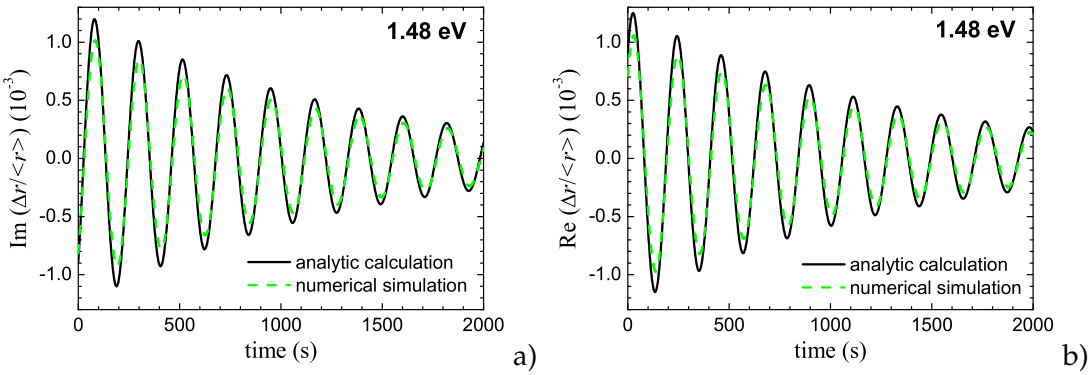

Figure 6.7: *Simulated RAS transients of the growth of undoped on doped GaAs – imaginary (a) and real part (b). The analytic curve was calculated using (6.15), the numerical results were obtained using a program (AnalysR, [71]) for the simulation of optical multilayer systems. Parameters: see text.*

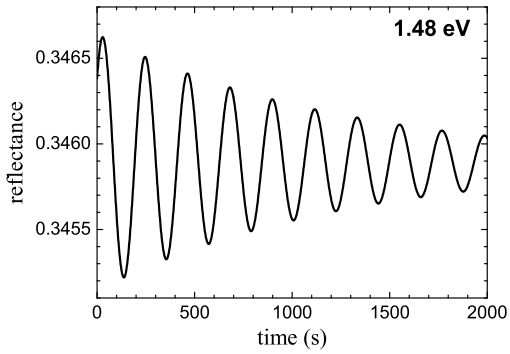

Figure 6.8: *Reflectance transient from the numerical simulation. Parameters: see text.*

This sample was grown on a Si-doped GaAs substrate ($5 \times 10^{18}\,\mathrm{cm}^{-3}$) at 650°C. Precursors were 100 Pa AsH_3 and 0.5 Pa TMGa. The first layer was nominally undoped (mid-$10^{15}\,\mathrm{cm}^{-3}$ range). The second one was doped with 2.0 mPa SiH_4, giving a doping level of $1.7 \times 10^{18}\,\mathrm{cm}^{-3}$. The SiH_4 partial pressure was further reduced in the subsequent layers. The last layer (no. 5) was undoped. The free carrier concentration was determined *ex situ* with C-V profiling.

Fig. 6.10 shows a RAS transient recorded at 1.6 eV during growth of this five-layer stack. The transients were recorded with a conventional RAS setup. The oscillation amplitude is apparently not related to the doping concentration, but related to the change in doping concentration between the layers. This can easily be recognized by comparing the amplitude during growth of the two undoped layers, no. 1 and no. 5: The amplitude of the first (undoped) layer no. 1 is much higher than that of the last

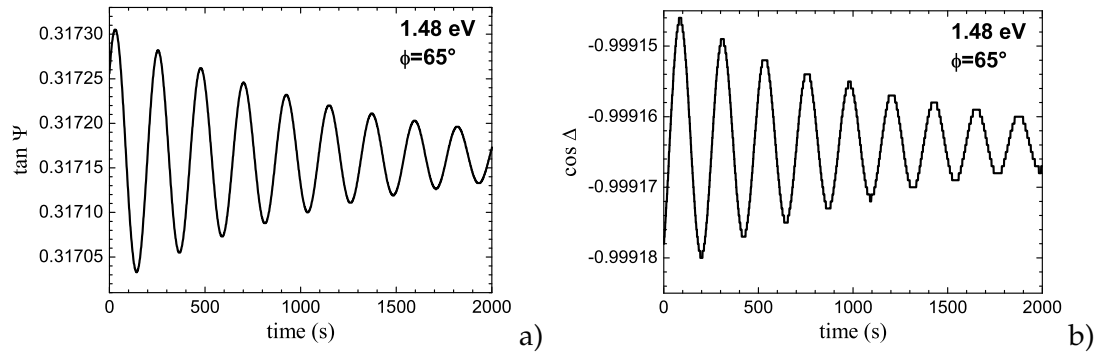

Figure 6.9: *Simulated SE transients of the growth of undoped on doped GaAs at 600°C. Parameters: see text.*

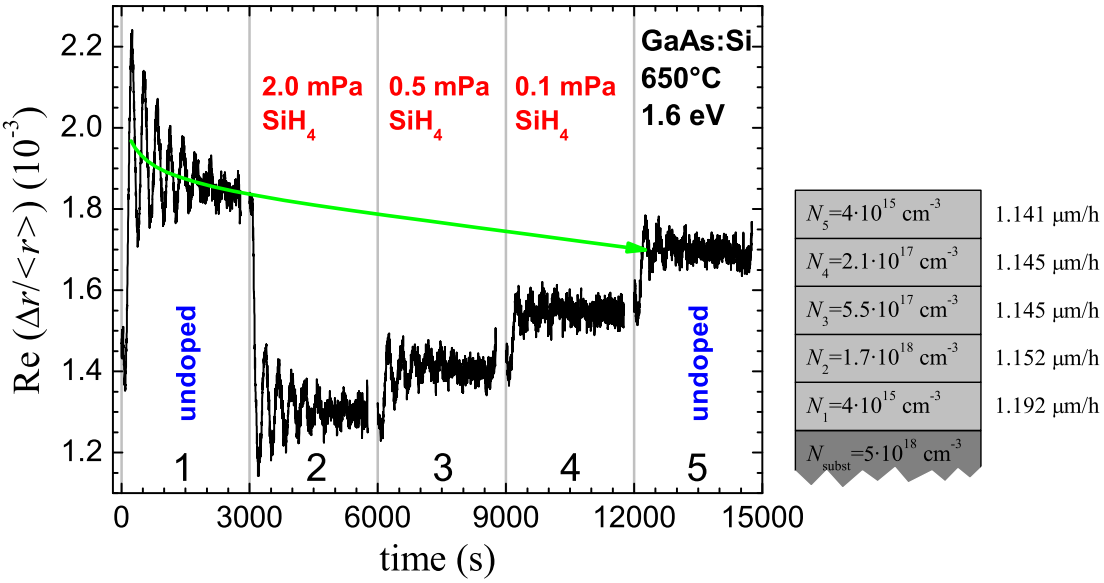

Figure 6.10: *RAS transients of a GaAs:Si/GaAs layer stack grown at 650°C using 100 Pa AsH_3 and 0.5 Pa TMGa. The substrate was Si-doped GaAs (5×10^{18} cm^{-3}). Layer 1 corresponds to the example shown in fig. 6.1.*

(also undoped) layer no. 5, because the difference in the doping concentration is higher for layer no. 1.

The baseline levels of the RAS transients is also a measure for the doping concentration. It strongly shifts between layer no. 1 and no. 2 and shows smaller steps according to the decrease of the doping level in the following layers. During the growth of the layer stack there is a drift of the RAS baseline level, indicated by the arrow in fig. 6.10, because the baseline of layer no. 5 does not reach the starting level of layer no. 1. This drift is probably due to thermal effects of the setup and its components.

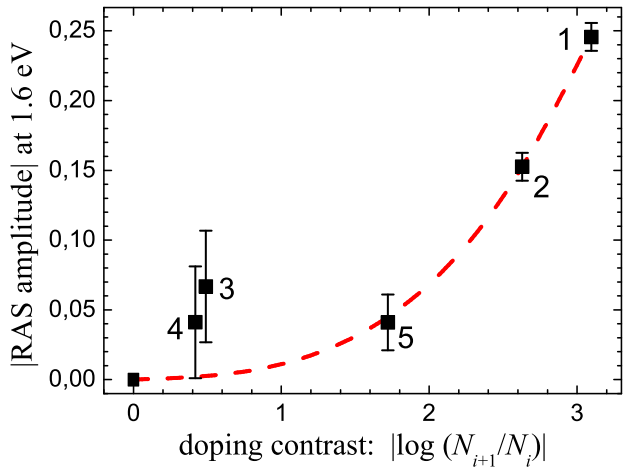

Figure 6.11: *Magnitude of the amplitude of the RAS doping-induced thickness oscillations of GaAs:Si in fig. 6.10 as a function of the absolute doping contrast $|C_{i+1}|$. The numbers in the figure correspond to the numbers of the layers in fig. 6.10. The curve is a guide to the eye. For zero doping contrast, no oscillations occur.*

The growth rate G was fitted using (6.1). With $n_{1.6\,eV}$=3.9443, values of 1.192, 1.152, 1.145, 1.145 and 1.141 μm/h were obtained (layer no. 1 to layer no. 5). The growth rate of layer no. 1 agrees with the values obtained from multichannel RAS measurements (section 6). The variation around the mean value of G is 2%. This indicates the high accuracy of this method.

To analyse the effect of doping on the amplitude of the oscillation, a quantity termed *doping contrast* C_{i+1} between layer i and layer $i+1$ is defined as

$$C_{i+1} = \log \frac{N_{i+1}}{N_i} = \log N_{i+1} - \log N_i \quad , \tag{6.23}$$

where N_i is the respective dopant concentration of layer i. The definition was chosen this way because the RAS signal change due to doping is proportional to the logarithm of the dopant concentration for moderate doping levels (section 5.4). Fig. 6.11 shows the magnitude of the oscillation amplitude as a function of the absolute value of the doping contrast $\log(N_{i+1}/N_i)$ within the GaAs:Si layer stack. The amplitude increases linearly with doping contrast C for higher doping contrasts (layers no. 1, 2, and 5) but saturates for doping contrasts below 1 (layers no. 3 and 4). A similar dependence was found for the change of RAS spectra as a function of the logarithm of the dopant concentration [63]. This indicates towards a similar origin for this effect, i.e. a band bending according to the doping contrast at the interface between the layers.

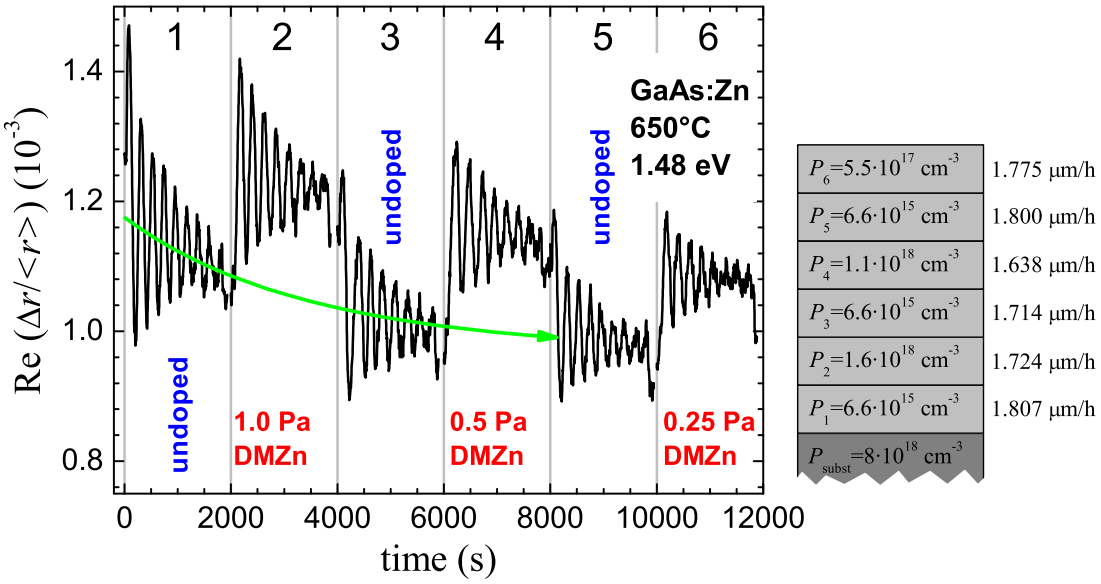

Figure 6.12: *Growth of a doped layer stack of GaAs/GaAs:Zn at* 650°*C. Shown is a RAS transient monitored at* 1.48 *eV. The partial pressures were* 100 *Pa* AsH_3 *and* 1 *Pa TEGa. The substrate was Zn-doped GaAs* (8×10^{18} cm^{-3}).

6.3.2 GaAs:Zn layer stack

Zn is the most widely used p dopant in III-V semiconductors. It has the disadvantage of diffusing at high doping levels. Common precursor molecules are DMZn (dimethylzinc, used in this work) and DEZn (diethylzinc).

The layer stack was grown on GaAs:Zn substrate ($8{\times}10^{18}$ cm^{-3}) at 650°C. Precursors were 100 Pa AsH_3 and 1.0 Pa TMGa. The layers with odd numbers (no. 1, 3, 5) were nominally undoped (mid-10^{15} cm^{-3} range) while the layers with even numbers are Zn-doped. The DMZn partial pressures range from 1.0 Pa in layer 2 to 0.25 Pa in layer 6, corresponding to doping levels between 1.6×10^{18} and 5.5×10^{17} cm^{-3} as determined by *ex situ* with C-V profiling.

In fig. 6.12 the growth of this layer stack is monitored at 1.48 eV. There are oscillations present in the first layer because of the doped substrate. As seen before for GaAs:Si, during growth of the layer stack there is a drift of the RAS baseline level of the undoped layers, as indicated by the arrow in fig. 6.12. Growth rates G of 1.807, 1.724, 1.714, 1.638, 1.800 and 1.775 μm/h were obtained from the fit (in order of growth, $n_{1.48\,eV}$=3.8738). The variation around the mean value of G is 5%.

A comparison of figs. 6.10 and 6.12 shows that the mean value of the oscillations, the baseline, correlates with the doping of the growing material: p-type doping leads to a positive and n-type doping to a negative offset. This effect has also been observed in the RAS spectra of doped samples [63].

The starting amplitude of the oscillations and the baselines of the doped layers are plotted in fig. 6.13. This shift of the baseline influences the sign of the first oscillation

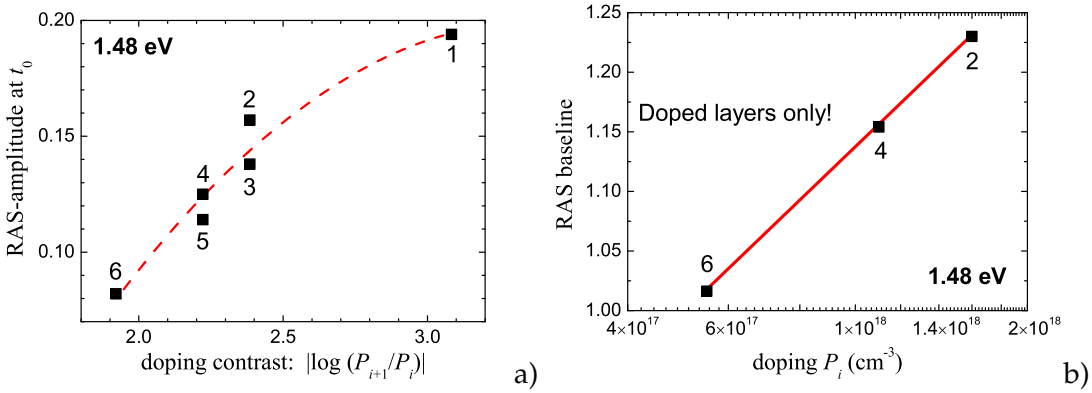

Figure 6.13: *a.) Magnitude of the amplitude of the RAS doping-induced thickness oscillations of GaAs:Zn in fig. 6.12 as a function of the absolute doping contrast $|C_{i+1}|$. The numbers in the figure correspond to the numbers of the layers in fig. 6.12. The curve is a guide to the eye. b.) RAS baselines of fig. 6.12 as a function of free carrier concentration P_i for the doped layers (no. 2, 4 and 6).*

in each layer.

6.4 Doping oscillations in InP

The influence of doping on the RAS spectrum of InP is somewhat different from what is known from GaAs. Neither an oscillatory structure nor a uniform vertical shift appear, but a change in the high-energy region ($3-5$ eV, at growth temperatures of $600-650$°C) is measured (figs. 6.14a and 6.18a).

In the difference spectra (figs. 6.14b and 6.18b) a peak emerges with increasing free carrier concentration. The centre of this peak is located around $4.3-4.6$ eV, depending on the temperature. This is also confirmed by the few works available in this field of research [76–78].

In order to attribute the energy of the doping peak to a bulk critical point, it is necessary to know the temperature dependence of the higher interband transitions of InP. Unfortunately, there are no data available for the E_0' and the E_2 critical point. Assuming a similar temperature shift as the E_0 [79] and the E_1 [7, 80, 81] critical points (-4×10^{-4} eV/K and -4.5×10^{-4} eV/K, respectively), at temperatures of $600-650$°C the E_0' critical point should be at 4.5 eV and the E_2 critical point at 4.8 eV [1]. The doping-induced peaks in figs. 6.14b and 6.18b can thus be attributed to the E_0' bulk critical point.

[1] The room temperature values are $E_0' = 4.704$ eV [82] and $E_2 = 5.04$ eV [83].

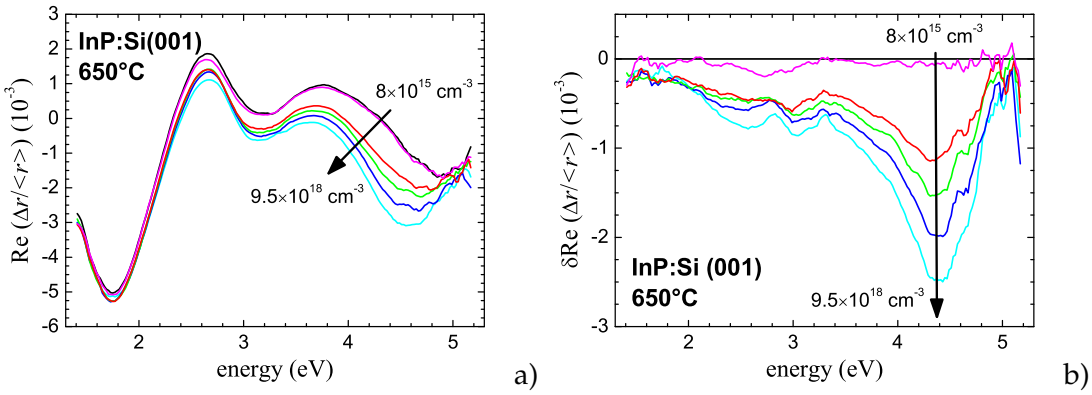

Figure 6.14: *RAS spectra of Si-doped InP at* 650°*C. Growth parameters:* 0.56 *Pa TMIn,* 200 *Pa* PH_3*. The* SiH_4 *partial pressures are* 3.1, 1.6, 0.8, 0.4 *and* 0 *mPa.*

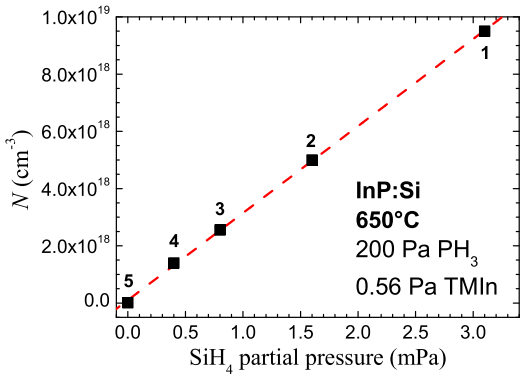

Figure 6.15: *Linear relationship between the* SiH_4 *partial pressure and the free carrier concentration of the grown layers. The numbers correspond to the layer numbers in fig. 6.16.*

6.4.1 InP:Si layer stack

After having explored the doping oscillations in GaAs, the question arises if this effect can also be observed in InP. For this reason a layer stack was grown at 650° with 200 Pa PH_3 and 0.56 Pa TMIn. Starting on a nominally undoped buffer, a highly doped layer (3.1 mPa SiH_4, 9.5×10^{18} cm^{-3}) was grown. For each new layer, the SiH_4 flow was set to half of the value of the preceding layer. The last layers were grown with 0.4 and 0 mPa SiH_4.

The RAS spectra and the difference spectra taken after the growth of each layer are shown in fig. 6.14. The free carrier concentration was determined by C-V profiling. In this range of doping concentrations it is linearly dependent from the silane partial pressure (fig. 6.15). The multichannel RAS transients taken during growth of the layer stack reveal that doping-induced thickness oscillations are also present in the indium phosphide material system (fig. 6.16). As can be also judged from the spectra in fig.

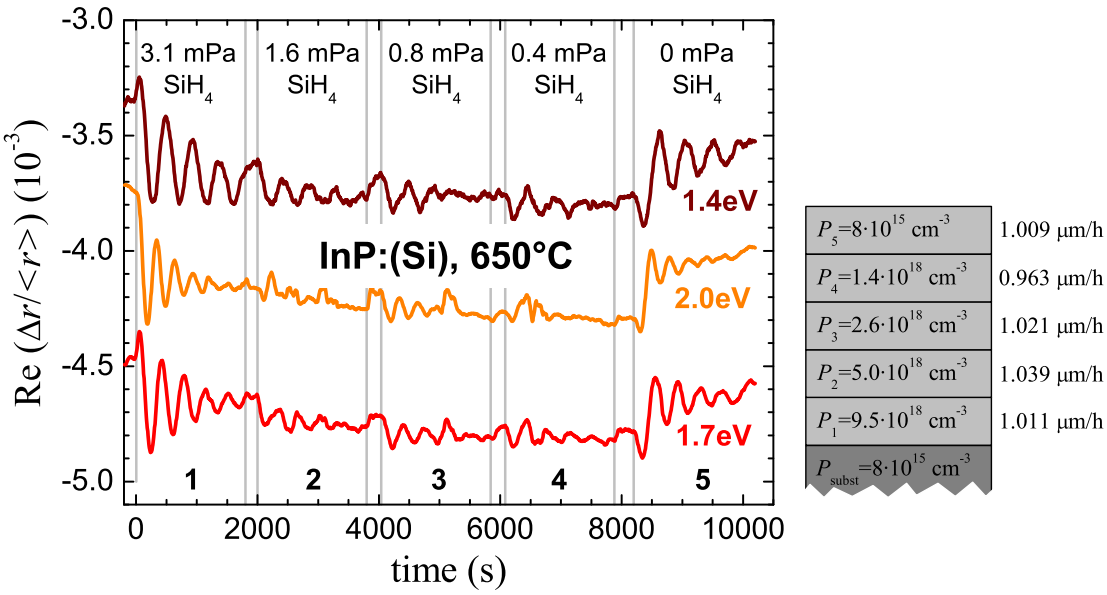

Figure 6.16: *RAS transients during growth of InP:Si on an undoped InP buffer at 650°C. The RAS spectra of the corresponding InP:Si layers are shown in fig. 6.14a. The first layer was grown on an undoped buffer – hence the oscillations.*

6.14, no shift of the baseline can be detected in the low-energy range of the monitoring energies. During growth of layers 2, 3 and 4, the oscillations are very weak and noisy because the doping contrast is small: $N_{i+1}/N_i \approx 0.5$, $\log(N_{i+1}/N_i) \approx -0.3$.

The oscillations were fitted with a damped cosine function as in sec. 6.3. The obtained growth rates are in the range of 1000 ± 40 nm/h. This agrees perfectly with the growth rate obtained from the C-V profile.

The amplitudes from the oscillation fits are plotted as a function of the absolute doping contrast for three different photon energies in fig. 6.17. The trend is the same as for GaAs: a higher doping contrast leads to a larger oscillation amplitude. The increase is very similar for different wavelengths.

6.4.2 InP:Zn layer stack

For the study of p-doping of InP with DMZn, a layer stack with increasing Zn concentration was grown. The growth temperature was 600° and the partial pressures were set to 200 Pa PH_3 and 1 Pa TMIn.

Starting on a nominally undoped buffer, the first layer was grown with 25 mPa DMZn. For each new layer the DMZn flux was doubled (50, 100, 200, 400 mPa) until reaching 800 mPa, which is almost a Zn:In ratio of 1:1. As can be judged from the (difference) spectra in fig. 6.18, there is a strong influence of the dopant flux on the RAS signal. The spectra of ΔRAS show a peak near the E_0' critical point, similar to the influence of n-type doping but with opposite sign (cf. fig. 6.14b).

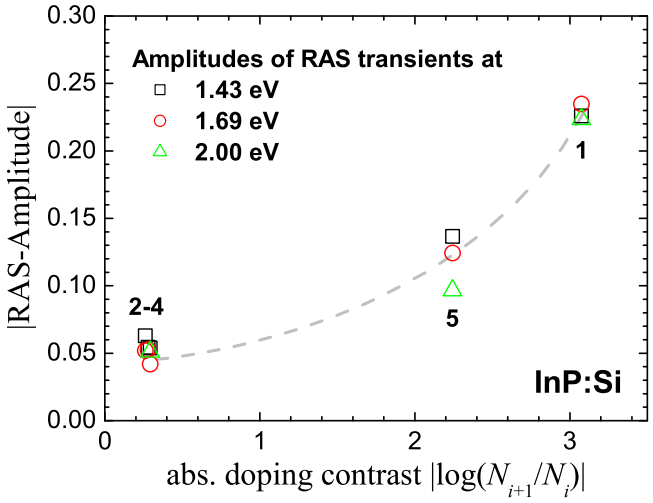

Figure 6.17: *Absolute values of the oscillation amplitudes at three different photon energies as a function of the absolute doping contrast for the growth of InP:Si. The numbers correspond to the layers in fig. 6.16.*

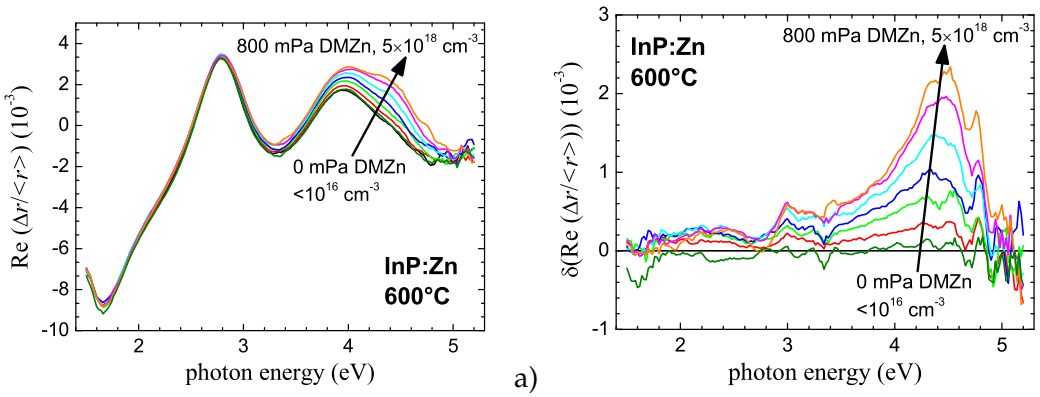

Figure 6.18: *RAS spectra (a) and difference spectra (b) of Zn-doped InP at 600°C. Growth parameters: 1 Pa TMIn, 200 Pa PH_3. The lowest DMZn partial pressure was 25 mPa and was doubled for each new layer until reaching 800 mPa. The last layer was nominally undoped.*

Despite the clear indication of dopant incorporation in the RAS spectra, the transients at photon energies near 2 eV did not show oscillations. The only exception is the topmost layer (nominally undoped) for which doping-induced oscillations were

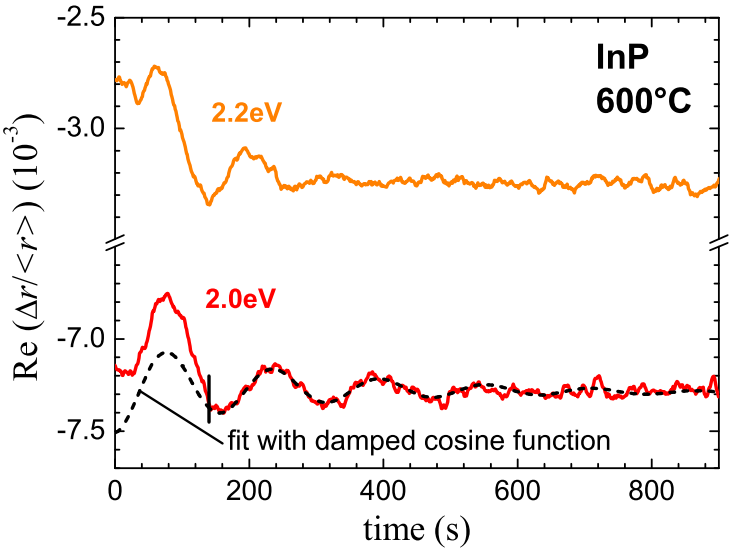

Figure 6.19: *RAS transients during growth of InP on InP:Zn at* 600°C*. The RAS spectrum of the InP:Zn layer is shown in fig. 6.18a (highest DMZn partial pressure). For the transient at* 2.0 *eV the damped cosine fit is indicated (fitting range starts at* 140 *s).*

measured (fig. 6.19). The growth rate that can be calculated from the period of the 2.0 eV transient ($n_{2.0\,eV}$=3.702) is (1.915 ± 30) μm/h.

The C-V profile of the topmost undoped layer and the two adjacent layers with the highest doping concentrations is shown in fig. 6.20. For the layers below the, the C-V measurement was not reliable. The Zn:In ratio was set to very high values. The saturation level of the free carrier concentration is already reached because the doubling of the ratio from 0.4 to 0.8 does not increase the doping level substantially.

The difficulties in reproducing the doping-induced oscillations in InP:Zn might be due to the easy diffusion of Zn in InP, making it problematic to reach abrupt steps in dopant concentration. The diffusion does not impose any problems at the surface where the interface is sharp and the electric field leads to a strong influence on the RAS spectrum (cf. fig. 6.18). At the buried interfaces, however, the smearing out of doping profile steps leads to very small electric fields because the change of dopant concentration happens on a larger distance. Hence the field-induced anisotropy is small.

The diffusion of Zn in InP has been thoroughly studied by Otsuka *et al.* [84]. They found that the solubility limit of Zn in InP is around 2×10^{18} cm^{-3} (growth at 600°C).

Zn diffuses faster than any n-type dopant in InP, which leads to displaced junction e.g. in heterobipolar transistors (HBTs).

The unintentional Zn diffusion from an adjoining p-InP layer into the active region of lasers during MOVPE growth has been reported to occur for Zn concentrations above 7×10^{17} cm^{-3} [85].

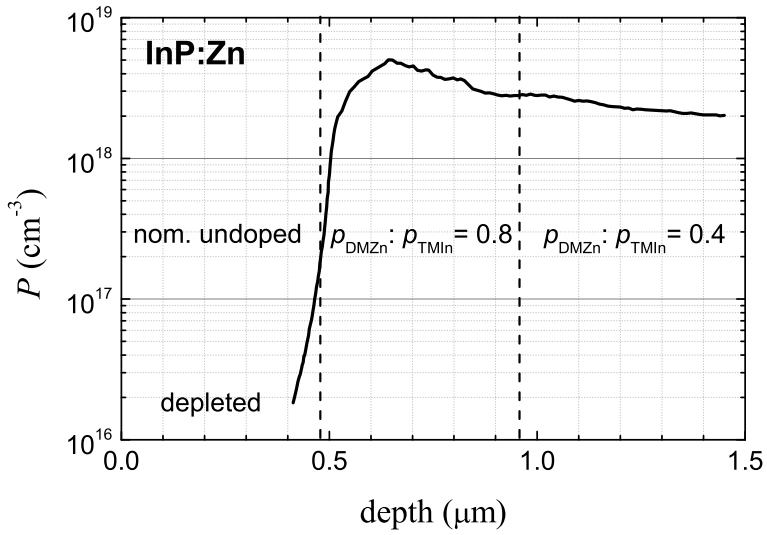

Figure 6.20: *C-V profile of the InP:Zn sample grown at 600°C. The free carrier concentration of the last two doped layers is almost the same (mid-10^{18} cm^{-3} range), although the difference in the DMZn partial pressure is a factor of 2.*

This diffusion problem could be overcome (at least for test structures) if a thin interlayer doped with Si or S was grown before the Zn-doped layer because Si and S act as a sink for Zn atoms. Blaauw *et al.* [86] proposed that diffusing Zn species are immobilised by association with ionised donor atoms, forming a neutral complex. In this manner, sharp doping profiles could be produced, allowing to measure pronounced doping oscillations.

Another reason is possibly the inappropriate doping profile of the sample: the only big step in doping concentration is the one between the top layer and the layer below.

7. Deoxidation of III-V semiconductors

The desorption of the oxide from the substrate or sample prior to epitaxial growth is of fundamental importance for the fabrication of state-of-the-art devices. The quality and morphology of the grown layers strongly depends on a smooth, defect-free starting surface.

The oxides of semiconductor surfaces have received considerable attention, being relevant in the context of semiconductor passivation and metal-insulator-semiconductor (MIS) device construction. The most thoroughly investigated semiconductor oxide is SiO_2 because it plays an important role in silicon devices due to its high stability, low diffusion coefficient, high dielectric coefficient and a low density of interface states at the Si/SiO_2 interface [87].

The oxides of III-V compounds were thoroughly studied at the beginning of the 1980s. The aim was to be able to grow defined and well controlled oxide layers not only on Si but also on III-V semiconductors. Promising applications were the passivation of the surface and the use for insulating layers in optical devices (lasers), MESFETs and MOS structures. It was found that the III-V oxides are rather complicated to handle and do not possess properties as known from silicon oxide – the main reason being that one has to deal with a mixture of many oxides and not a homogenious layer.

7.1 Ternary phase diagrams

The understanding of the oxide properties of binary semiconductors is complicated by the variety of possible oxide species that can be formed from a group III element, a group V element and oxygen.

Ternary phase diagrams (TPDs) help to decide what stoichiometric mixtures of three compounds (e.g. III-V plus oxygen) can form stable products. It is a convenient method of showing the possible reactions between the elements and compounds.

TPDs are constructed by determining or estimating the Gibbs free energy G of all possible reactions. If G is negative, then the reaction is exothermic and the products are stable (endothermic = not stable). The relative likelihood of two reactions is given by the relative values of G for the two reactions: the more negative G is, the more likely is the reaction.

In the case of oxides of III-V compounds (figs. 7.1 and 7.2), the ternary phase diagrams are constructed by putting the group III compound, the group V compound and oxygen at the apexes of an equilateral triangle. The known stable compounds are placed on lines connecting the corresponding elements. When two compounds are connected by a line (so-called *tie line*), no reactions between them can occur. On the other hand, if two compounds are not connected by a tie line, they can react.

The equilibrium interface composition of an oxidised III-V compound can be predicted by drawing a line from the III-V compound point (middle of the triangle's base

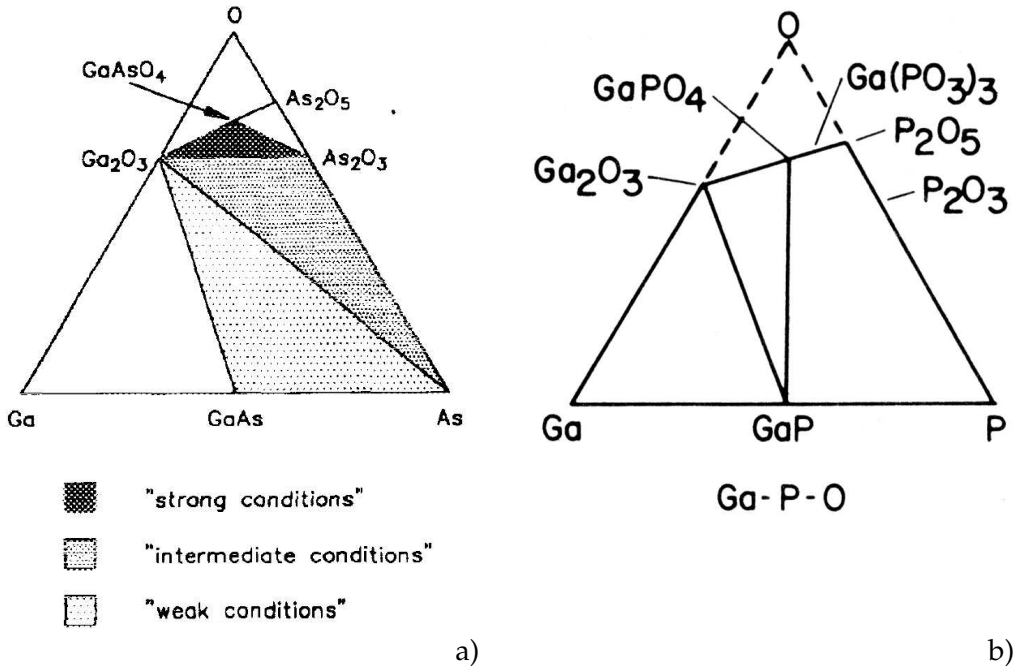

Figure 7.1: *Ternary phase diagrams of (a) GaAs (taken from [88]) and (b) GaP (from [89], after [90]).*

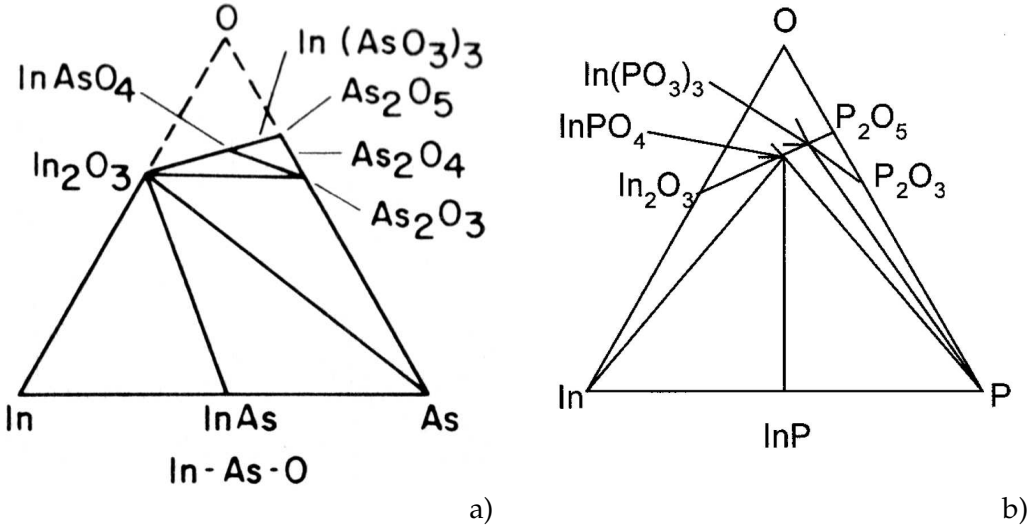

Figure 7.2: *Ternary phase diagrams of (a) InAs (from [89], after [90]) and (b) InP [91].*

in the given examples in figs. 7.1 and 7.2) to the oxygen. If tie lines are cut on the way, the compounds at the end of the tie line can appear at the interface. In the case of GaP (fig. 7.1b) these compounds are $GaPO_4$, Ga_2O_3 and P_2O_5. The elemental phosphorus itself cannot be part of the interface, in contrast to InP (cf. fig. 7.2b).

Since oxide growth is often far from equilibrium, the TPDs can only give a rough idea of possible compositions. Furthermore, they are constructed by using mostly room temperature data for the Gibbs free energy.

7.2 Evaluation of ellipsometry spectra

The major optical *in situ* technique used in this chapter is spectroscopic ellipsometry (SE, sec. 2.2). It is very sensitive for the surface morphology (roughness) and for multilayer structures (like a substrate covered by an oxide film). In this study SE will be used to determine the thickness of the oxide layer (also at temperatures above room temperature) and the roughness of the surface after deoxidation and buffer growth. This means that the dielectric function of the substrate semiconductor and the oxide must be known as a function of temperature. Regarding the bulk semicondurctor, these data are available for many binary III-V semiconductors (e.g. [92] for room temperature and [12] for high temperature data). The situation is worse for the dielectric function of the oxides: the chemical composition of the oxides is often unclear or not well defined and only few data are available for room temperature [71, 93, 94]. High temperature data are not available at all. However, as fig. 7.3 shows, the oxide spectral features are rather broad. Thus for low temperatures, the room temperature data might still be a good approximation.

In this work, a different approach is used: the high-temperature dielectric function of the oxide layer is approximated by a thin layer of roughness on the surface using the Bruggeman effective medium approximation, cf. sec. 7.2.1).

The output data of the ellipsometer used in this work are the ellipsometric angles $\tan\Psi$ and $\cos\Delta$. To calculate the effective dielectric function and to obtain layer thickness information from optical models, one needs to determine the angle of incidence ϕ_0 first. This is done by assuming a model structure of a semi-infinite bulk semiconductor with an oxide layer of some nm on top. The dielectric function of the corresponding oxide is taken from a database (see fig. 7.3). The thickness and the angle of incidence are varied by a numerical routine [71] to find the closest match of the calculated and the measured spectrum.

The influence of the oxide layer thickness and ϕ_0 on the ellipsometric angles is wavelength-dependent: For typical III-V semiconductors, an increase of ϕ_0 leads to a reduction of $\tan\Psi$ in the low-energy range of the spectrum and to an increase of $\cos\Delta$ in the high-energy range. On the other hand, an oxide layer influences the entire spectrum and leads to an increase in $\cos\Delta$ and a decrease in $\tan\Psi$. Therefore an unambiguous determination of both angle of incidence and oxide layer thickness is possible.

The SE data were evaluated in the following manner: Prior to a set of desorption experiments, a spectrum of the oxidised sample was measured (energy range 1.5−6 eV). Then a simultaneous fit of the angle of incidence ϕ_0 and the oxide layer thickness was performed with an optical multi-layer routine [71]. The computed angle of incidence was used for all subsequent measurements of this run.

Figs. 7.4 and 7.5 show examples for each material system studied. The plots show the imaginary part $\langle\epsilon_2\rangle$ of the effective dielectric function at room temperature for the

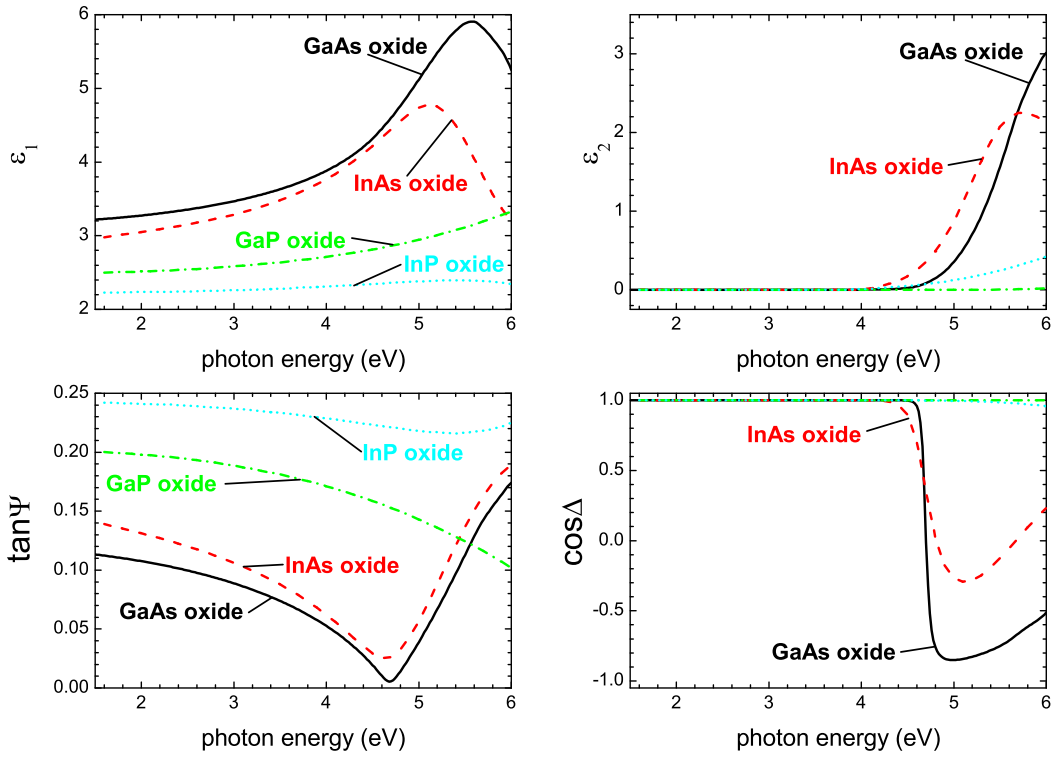

Figure 7.3: *Room temperature dielectric function and ellipsometric parameters* $\tan\Psi, \cos\Delta$ *(at 65° angle of incidence) for some binary III-V semiconductor oxides. The data are taken from the database of AnalysR [71] (GaAs oxide) and the freely available SOPRA database [94] (GaP, InAs and InP oxide).*

sample before and after thermal deoxidation in MOVPE. The samples were heated under group V overpressure to the final temperature (indicated in the graphs). Then a buffer layer was grown at 50°C below the final deoxidation temperature. The sample was then cooled to room temperature and the spectrum of the deoxidised surface was taken. In the case of GaP (fig. 7.4b) the sample was etched prior to deoxidation with 75% H_2SO_4 for 1 min at 80°C, with a solution of 75% H_2SO_4 and 30% H_2O_2 for 2 min at 80°C and with 25% H_2SO_4 for 30 s at room temperature. The details of the etching procedure are given in appendix A.2.

To determine the residual roughness in figs. 7.4 and 7.5, we define the thickness of an EMA layer (sec. 7.2.1) with a host/air ratio of 0.5/0.5 as the residual roughness. However, this value is not comparable to the rms roughness and gives only a coarse estimate.

Since an oxide layer and a layer of roughness have a similar influence on the effective dielectric function, the accuracy in the determination of the oxide layer thickness is limited on principle to approximately one monolayer.

Especially for the experiments in sec. 7.7 (deoxidation at constant temperature) it is necessary to obtain a layer thickness from single wavelength measurements (tran-

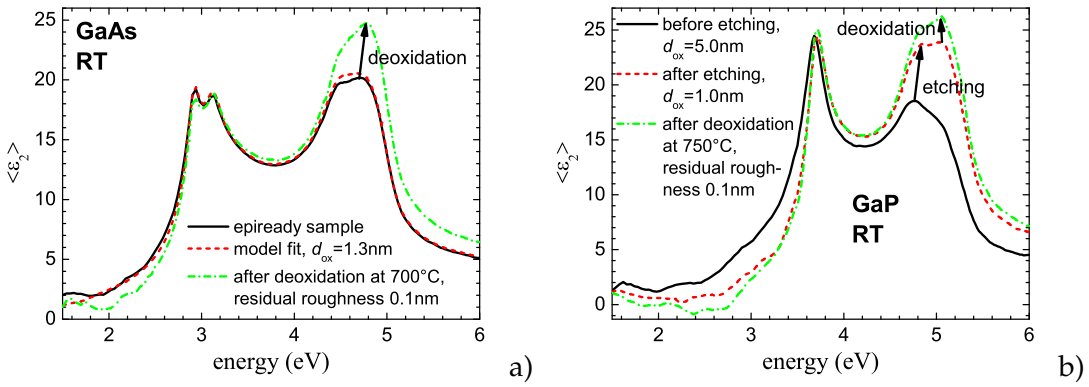

Figure 7.4: *Imaginary part of the effective dielectric function before and after the deoxidation of GaAs (a) and GaP (b). GaP was etched prior to deoxidation (see text).*

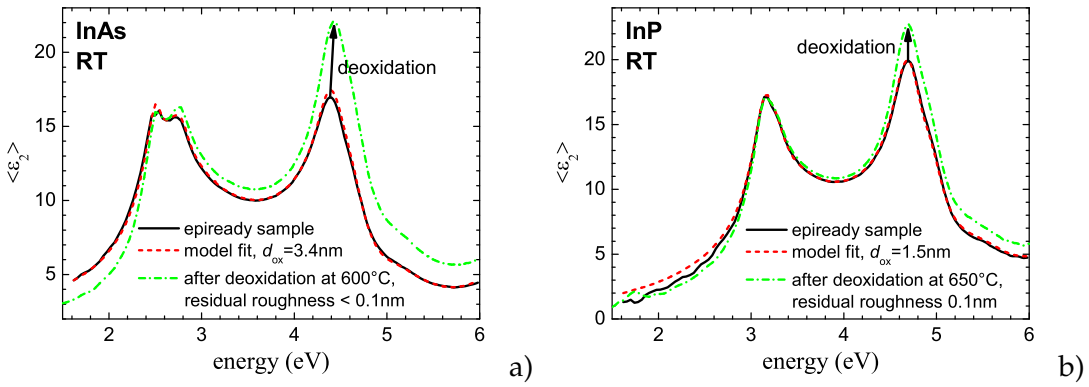

Figure 7.5: *Imaginary part of the effective dielectric function before and after the deoxidation of InAs (a) and InP (b).*

sients). For this evaluation a simulation for various thicknesses of the rough layer at this specific temperature is performed. The datapoints of the layer thickness as a function of $\langle\epsilon_2\rangle$ are then fitted with a fourth-order polynomial to obtain a formula for the conversion of $\langle\epsilon_2\rangle$ into layer thickness.

7.2.1 Effective medium approximation

While the thickness of the oxide layer at room temperature was fitted using database oxide dielectric functions, this is not possible at higher temperature where only the dispersion of the bulk III-V semiconductors are available. In this case, effective medium approximation can help to model this system despite the lacking oxide dielectric function.

Effective medium theory describes materials that are inhomogenious on a microscopic scale, i.e. the macroscopically homogenious material consists of separate

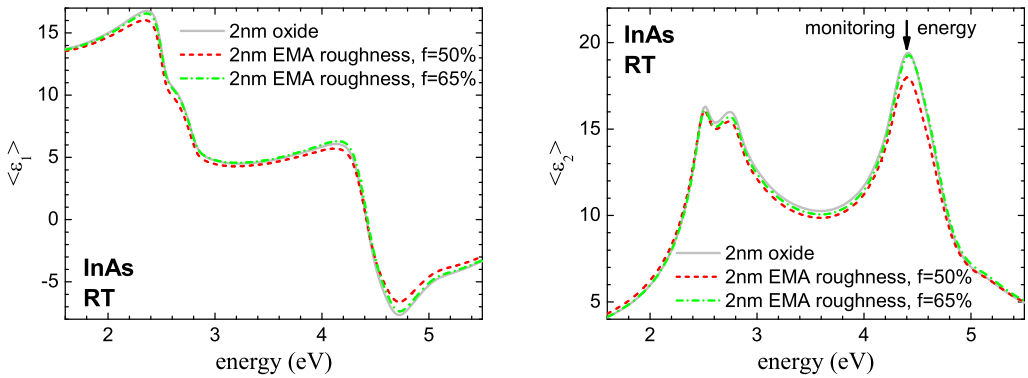

Figure 7.6: *Example of the fitting results for a* 2.0 *nm thick layer of oxide/ roughness on InAs (simulated effective dielectric function). The value of* $f = 65\%$ *gives the closest match of oxide and roughness spectra, especially at the monitoring energy of* 4.4 *eV.*

regions (small compared to the wavelength of the light) which possess their own dielectric properties. The effective medium is the equivalent homogenious material that has the same properties as the microscopically inhomogenious material. An example for this material class are voids in a closed epitaxial layer. Applications of effective medium theory with respect to ellipsometry can be found in [6]. A good overview of recent developments in effective medium theory is given in [95].

Effective medium theory applied to dielectric functions calculates an effective dielectric function $\langle\epsilon\rangle$ of given *guest* material inclusions in a so-called *host* medium. The exact formula depends inter alia on the mean shape of the inclusions.

A very simple but effective model is the Bruggeman model [96], which is often referred to as *the* Effective Medium Approximation (EMA). The Bruggeman theory treats the guest and the host material equally:

$$f\frac{\epsilon_g - \langle\epsilon\rangle}{\epsilon_g + 2\langle\epsilon\rangle} + (1-f)\frac{\epsilon_h - \langle\epsilon\rangle}{\epsilon_h + 2\langle\epsilon\rangle} = 0 \quad . \tag{7.1}$$

The parameter f defines the fraction of the guest material (ϵ_g) in the host (ϵ_h).

Solving (7.1) for $\langle\epsilon\rangle$ leads to the quadratic equation

$$\langle\epsilon\rangle = \frac{z}{2} \pm \frac{1}{2}\sqrt{z^2 + 2\epsilon_g\epsilon_h} \tag{7.2}$$

with

$$z = \frac{(3f-1)\epsilon_g + (2-3f)\epsilon_h}{2} \quad . \tag{7.3}$$

The negative solution in (7.2) is physically not relevant.

For reasons of simplicity, the effective medium composition is often set to $f = 0.5$ (e.g. for the determination of roughness).

For the simulation of oxide dielectric functions, a value of $f = 0.5$ is not the optimum value. In this work, f was determined by taking the following steps:

Substance	$d_{ox} = 0.5\,nm$	$d_{ox} = 1.0\,nm$	$d_{ox} = 2.0\,nm$	$d_{ox} = 5.0\,nm$
InAs	$f = 66\%$	$f = 66\%$	$f = 65\%$	$f = 63\%$
GaAs	$f = 47\%$	$f = 46\%$	$f = 45\%$	$f = 38\%$
InP	$f = 61\%$	$f = 61\%$	$f = 60\%$	$f = 57\%$

Table 7.1: *Fitted optimum values for the fraction f of the semiconductor (guest material) in air (host material) for several oxide layer thicknesses.*

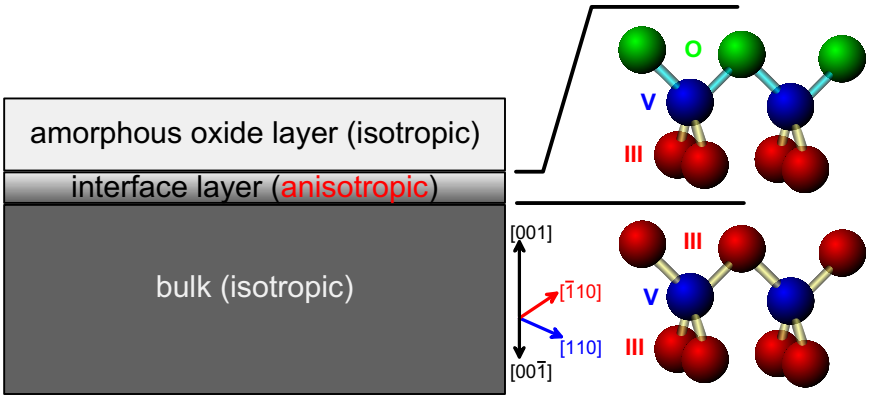

Figure 7.7: *Model of the oxidised surface of a III-V-semiconductor and the bond configuration at the interface to the oxide.*

1. Generate the effective dielectric function (at room temperature) of the respective semiconductor with an oxide layer (thickness d_{ox}) out of database values. The room temperature dielectric function of the oxide must be known.
2. Generate the effective dielectric function (RT) of the semiconductor with a layer of EMA roughness (same thickness as the oxide layer!).
3. Fit the fraction f of the EMA layer with a thin film simulation package [71]. An example is shown in fig. 7.6.
4. Verify f for different values of d_{ox}.

For the determination of f values of $d_{ox} = 0.5, 1.0, 2.0$ and $5.0\,nm$ were used. The optimum values for InAs, GaAs and InP are given in tab. 7.1. Since the oxide layers in chapter 7 are mostly below 1 nm the value of f for $d_{ox} = 0.5\,nm$ was selected for the determination of oxide layer thickness at high temperature.

7.3 RAS measurements during oxide desorption

The second optical *in situ* technique that is used for the detection of oxide desorption is RAS. The oxidised semiconductor possesses already a characteristic RAS spectrum

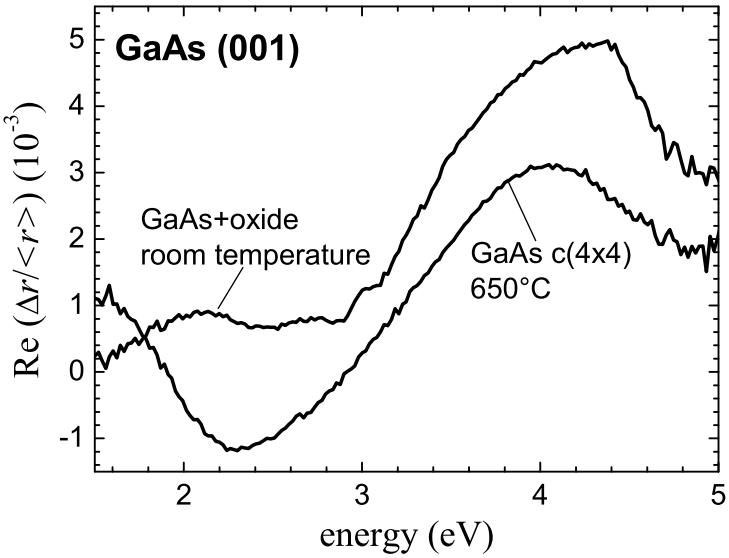

Figure 7.8: *RAS spectra of epiready GaAs (i.e. with oxide layer) and* $c(4\times4)$*-reconstructed GaAs at* $650°C$*.*

(e.g. for GaAs see fig. 7.8). The origin of the anisotropy is explained in fig. 7.7, which shows a model of an oxidised III-V-semiconductor surface. Not included in this model are possible water films or other contaminations like carbon hydrates on the topmost layer. As was found in [97], the presence of water during oxidation may lead to the formation of Ga-OH.

In the bulk, the bonds are directed alternately along the directions [110] and $[\bar{1}10]$. This means that in the first approximation the bulk is optically isotropic because the contributions from the directed bonds cancel out over many layers.

The oxide consists of two layers: a thick amorphous oxide layer and a thin interface layer. It is assumed that the amorphous oxide layer is optically isotropic on a macroscopic scale and thus does not contribute to the RAS signal [98]. It is, however, detected in by the ellipsometric measurement. In special cases it is possible that the oxide shows signs of crystallinity (cf. e.g. [99]). Furthermore, the bulk lattice may modify the otherwise amorphous oxide structure adjacent to the interface.

At the interface to the oxide, the symmetry of the point group is broken. The bonds to the oxide, e.g. the bonds between the group V-atoms and oxygen atoms, are aligned along the $[\bar{1}10]$ direction. This bond-induced anisotropy is responsible for the characteristic spectrum of the oxidised surface.The shape of the RAS spectrum of oxidised GaAs(001) and AlGaAs(001) was attributed to local field effects by Berkovits *et al.* [98].

The RAS spectrum changes drastically when the oxide layer is removed thermally and a surface reconstruction is formed. This is shown for GaAs(001) in fig. 7.8. RAS spectra of other III-V compounds can be found in sec. 7.5.

The change between the oxide RAS spectrum at room temperature and that of the reconstructed surface at high temperature can be used to study the oxide desorption

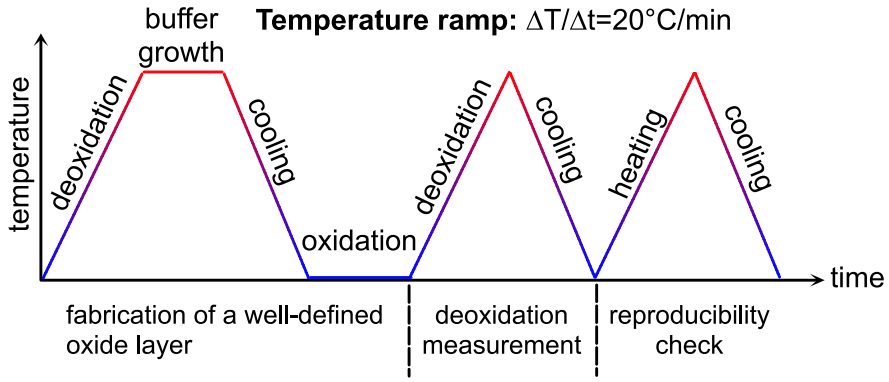

Figure 7.9: *Recipe for the deoxidation study in sec. 7.5.*

characteristics. For these measurements a multichannel RAS system (chapter 3) is especially suitable because one can circumvent the situation that the selected photon energy is not sensitive for the change between the oxide spectrum and the spectrum of the reconstruction.

7.4 Experimental overview

The deoxidation experiments in this chapter are concerned with the III-V materials GaAs, GaP, InAs and InP. Three different kinds of *in situ* experiments are described in the following sections.

The first (sec. 7.5) is a RAS-only study which involved a complex preparation of the samples. This study was carried out apart from the daily growth business because the subsequent heating/cooling steps were too time-consuming.

The second type of experiment (sec. 7.6) is very similar to the standard deoxidation procedure and can thus be used as a replacement. The only exception was that the temperature increase was limited by a programmed ramp.

The third kind of study is the oxide desorption at fixed temperature. *In situ* data were collected with SE and RAS. The purpose of this experiment was to determine the activation energy of oxide desorption for the usual III-V semiconductors.

All experiments were performed in the MOVPE system described in chapter 2. The total pressure was 100 mbar. H_2 was used as carrier gas, AsH_3, PH_3, TMGa and TMIn were used as precursors.

7.5 Deoxidation with temperature ramp – a RAS study

This section describes a set of experiments that was perfomed to compare the RAS signatures during oxide desorption of the binary III-V compounds GaAs, GaP, InAs and InP. The experimental procedure is depicted in fig. 7.9. The (001) sample wafers (epiready grade, except for GaP) were thermally deoxidised under AsH_3 or PH_3 overpressure. Then a buffer layer was grown under standard growth conditions, and after cooling to room temperature the samples were oxidised for 1 h with ambient air by

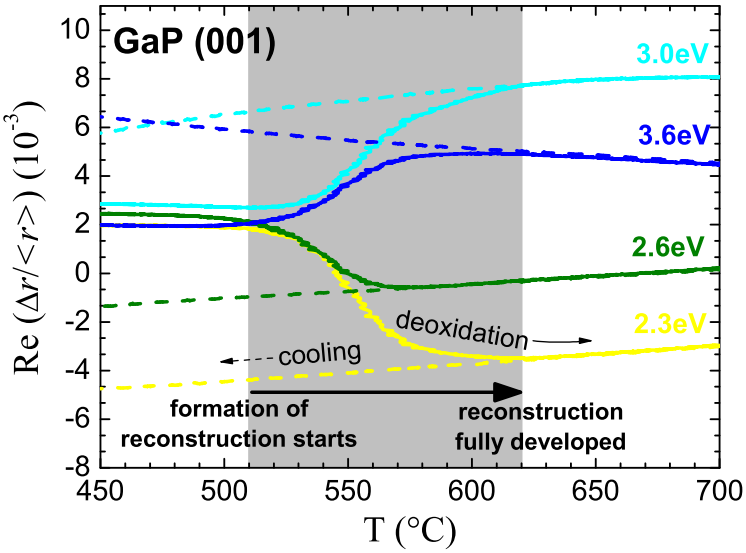

Figure 7.10: *Selected RAS transients measured during deoxidation (solid lines) and subsequent cooling (dashed lines) of GaP.*

opening the rear reactor entrance. It must be noted that this kind of oxidation is neither well-defined nor can the presence of water and other contaminants on the surface be excluded.

After this creation of a fresh oxide layer the actual RAS measurement during thermal oxide desorption was performed. The last step of heating an cooling was undertaken for verification of the reproducibility and to separate the influence of temperature on the RAS signal from the effect of oxide desorption/reconstruction formation. It was found that the transients during heating and cooling match.

Fig. 7.10 shows a typical RAS transient measurement during deoxidation and cooling of GaP(001) for the temperature range of interest. The transients taken during oxide desorption (solid lines) show a pronounced, nonlinear characteristics while the cooling transients (dashed lines) are almost linear with temperature. This approximately linear change during cooling (and heating) of the oxide-free[1] surface reflects the thermal broadening of the RAS spectra. Deviations are usually due to the spectral shift of bulk critical points with temperature.

A change of temperature may also lead to the development of a different reconstruction which is energetically more favourable. Such changes in the transients are highly nonlinear and can be easily separated from the broadening effect.

The initial oxidised surface exhibits only a small degree of anisotropy. Between 510°C and 620°C the anisotropy increases because some regions on the surface become oxide-free and the reconstruction ((2×1) symmetry) develops. This process causes the distinctive changes of the slope in the transients. The removal of the oxide (at least all

[1]Oxide-free in this context means that the surface has reached a stable state where no irreversibel changes upon heating occur. It is, however, possible that stable oxide compounds still remain on the surface.

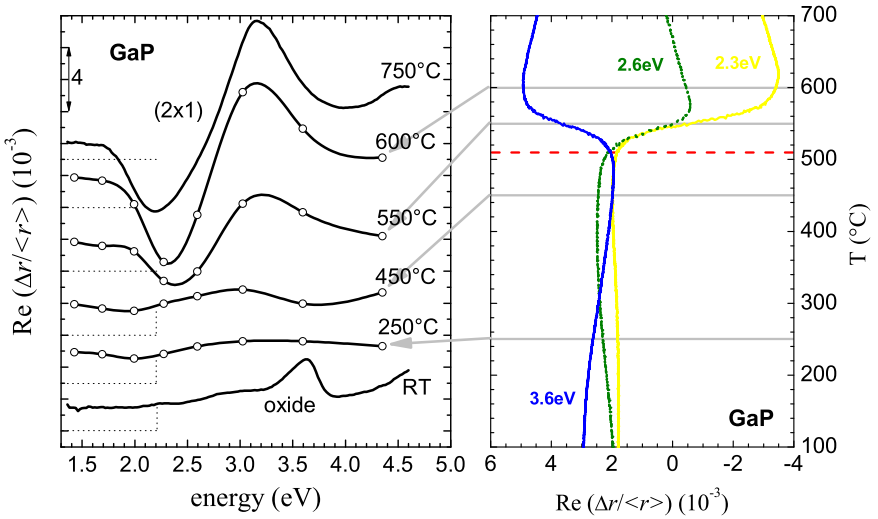

Figure 7.11: *RAS spectra (left) and corresponding transients at three selected photon energies (right) measured during deoxidation of GaP. The spectra showing data points (∘) are measured with multichannel RAS, all other spectra are scanning RAS spectra. The dashed horizontal line in the right graph marks the beginning of the formation of a reconstruction.*

oxide compounds that can be desorbed by this method) is complete at 620°C, because, above this temperature, all transients taken during deoxidation and during cooling match. The importance of measurements at different photon energies is emphasized by the transient at 2.6 eV: the deoxidation and cooling transients match already for $T > 570$°C, although the oxide desorption is still incomplete.

Fig. 7.11 shows the same process in a different way: Shown on the left side are RAS spectra taken before and after deoxidation (scanning RAS spectra, RT and 750°C) as well as multichannel RAS spectra in between. The right side shows three selected RAS transients (also shown in fig. 7.10) as a function of wafer temperature. They are plotted in an unusual way – the temperature axis is vertical. This allows for an easy visual connection of the spectra on the left and the transients on the right. The dashed horizontal line at 510°C in the transient graph marks the beginning of the formation of the (2×1) reconstruction. The transients taken during cooling are not displayed for reasons of clarity.

This experiment was repeated for GaAs (fig. 7.12), InAs (fig. 7.13) and InP (fig. 7.14). The begin and end of the reconstruction formation (corresponding to begin and end of oxide desorption) depends strongly on the semiconductor material but the shape of the transients is similar: a strong change at all photon energies (horizontal dashed line) is followed by a slower development of the reconstruction via intermediate states. This is especially pronounced in the case of InAs where the change from (2×4) to (4×2) symmetry can be measured when going from 470°C to 600°C.

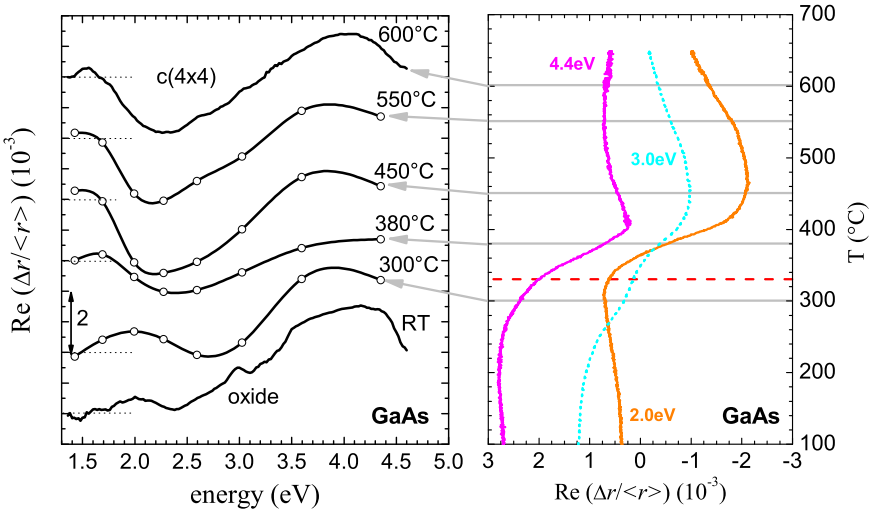

Figure 7.12: *RAS spectra and transients during deoxidation of GaAs. Refer to the caption of fig. 7.11 for an explanation of the graphs.*

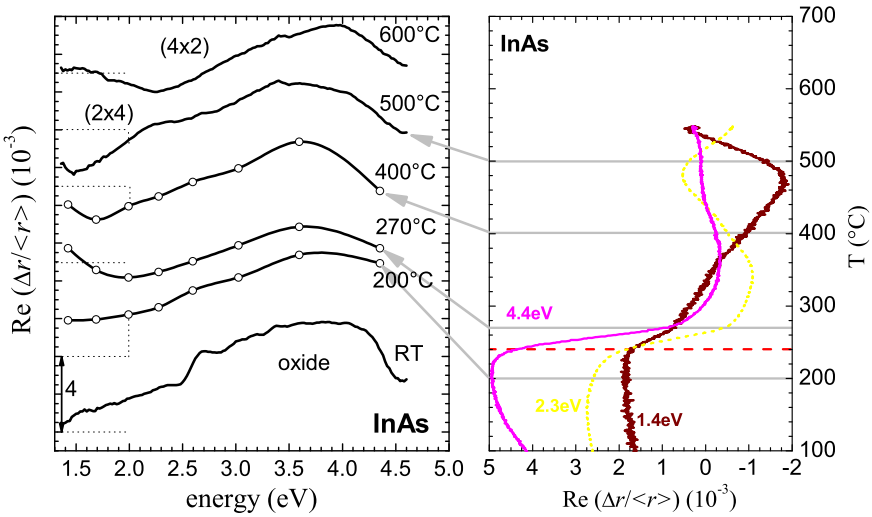

Figure 7.13: *RAS spectra and transients during deoxidation of InAs. Refer to the caption of fig. 7.11 for an explanation of the graphs.*

Taken from these experiments, the temperatures for the start and end of the development of a clean, reconstructed surface are plotted in fig. 7.15 for InAs, GaAs, InP and GaP as a function of the heat of formation Δ_{AB} (corresponds to the bond energy). The data show that there is a direct relation between the temperature and the bond energy of the semiconductor: The temperatures for the beginning of oxide desorption as well as the temperatures for reaching the final, reconstructed surface increase with bond energy of the bulk semiconductor. Regarding the chemical trends, the oxide

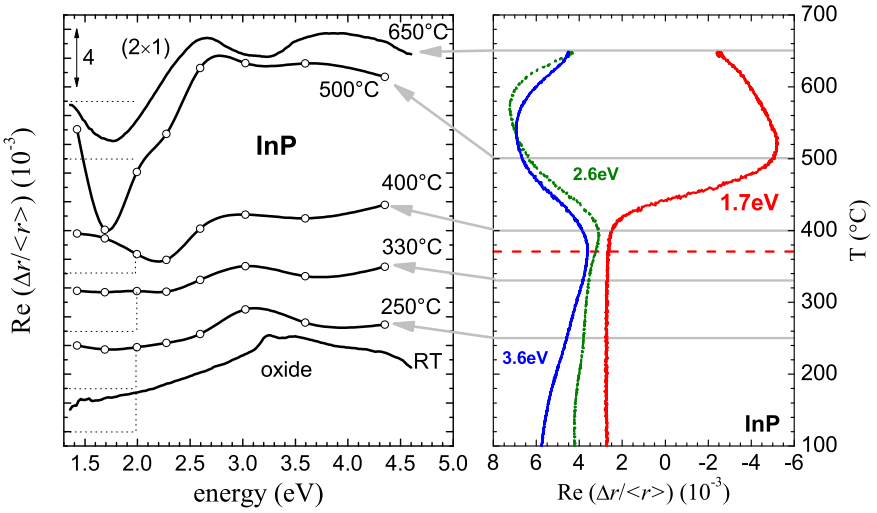

Figure 7.14: *RAS spectra and transients during deoxidation of InP. Refer to the caption of fig. 7.11 for an explanation of the graphs.*

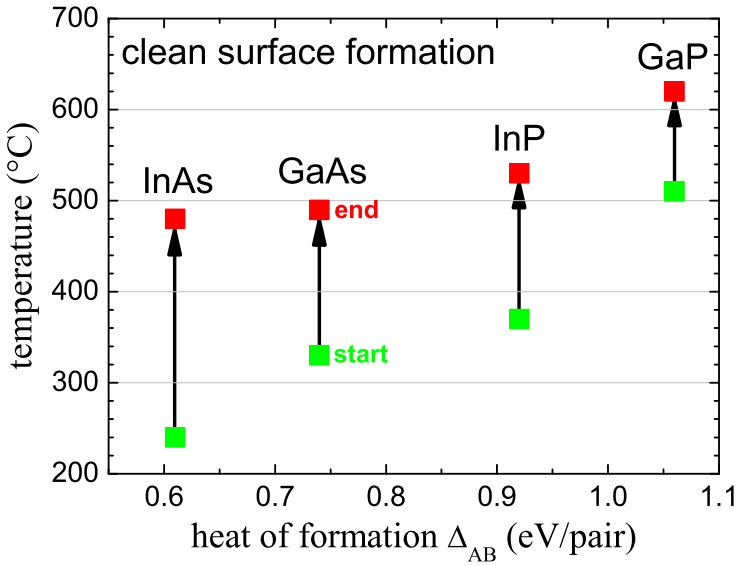

Figure 7.15: *Temperatures for begin and end of clean surface formation during deoxidation as a function of heat of formation Δ_{AB} [100] (corresponds to the bond energy).*

desorption from arsenides takes place at lower temperatures than from phosphides. The same trend holds for In and Ga compounds.

The values in fig. 7.15 are specific for the chosen preparation process (fig. 7.9) and the MOVPE machine. However, they give an estimate which temperature range is

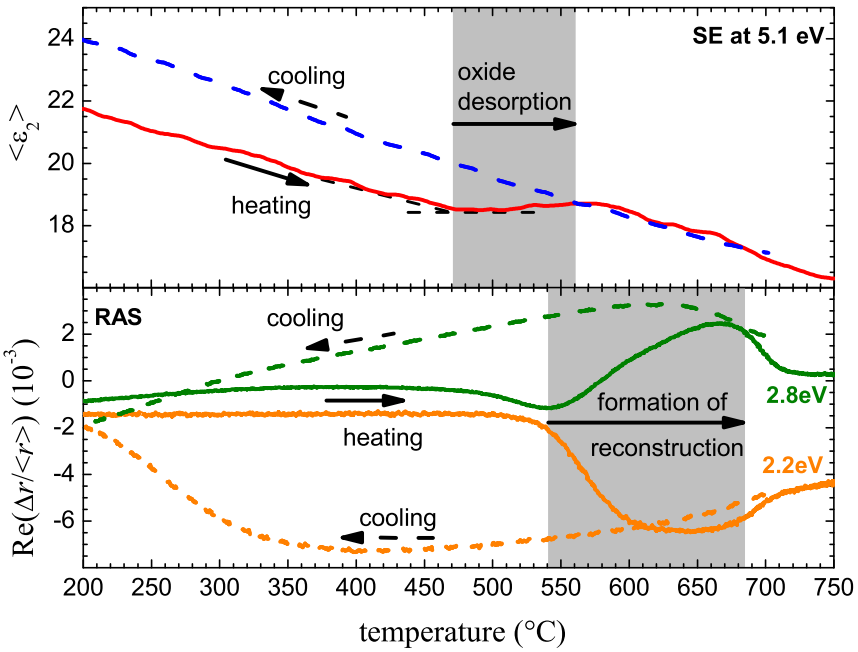

Figure 7.16: *RAS and SE signal of GaP as a function of temperature during deoxidation (heating) and subsequent cooling. The RAS transients were taken with a multichannel RAS setup [101]. During heating the temperature was ramped up with 25°C/min. At all temperatures above 200°C the PH_3 stabilization (200 Pa) was switched on.*

suitable for the deoxidation process. Moreover, the data allow a comparison between the different material systems.

7.6 Deoxidation with temperature ramp – a RAS and SE study

The oxide desorption study in the previous section was concerned with the deoxidation of a freshly created oxide layer. The experiments in this section were performed not as a separate set of experiments but prior to the growth of samples for other studies. The only exception to the deoxidation process that would otherwise have been used was that the sample heating was not set to a fixed power level. Instead, the temperature was increased with a ramp of 25°C/min to maintain a certain degree of reproducibility. The cooling after deoxidation is also an additional step that is not performed otherwise.

Additionally, the samples were monitored with SE, which allows a quantitative estimation of the oxide layer thickness.

The material systems studied were GaAs, InP and GaP. As usual, the group V precursor was switched on when reaching 200°C.

Fig. 7.16 shows an example of the SE and RAS signals during deoxidation and subsequent cooling of GaP. While all other materials were epiready wafers, epiready

GaP was not available. Therefore the GaP sample was etched as described in sec. 7.2 (see also appendix A.2) before being transferred to the MOVPE reactor.

The monitoring energy for ellipsometry was set to the energy of the E_2 critical point at room temperature. The sample was heated using a temperature ramp of 25°C/min until reaching 750°C. Then a buffer was grown at 700°C and the sample was cooled to room temperature.

During heating, $\langle \epsilon_2 \rangle$ decreases linearly with temperature until the oxide overlayer starts to reduce at 470°C. Above 560°C the oxide layer desorption is complete, because the transients during heating and cooling run parallel.

The RAS transients show a strong increase above 540°C, where the oxide layer desorption is almost complete. This indicates that certain regions of the surface are already deoxidised, at least to an extent that allows a formation of the reconstruction (inhomogenious oxide desorption). It is difficult to determine the point where the formation of the reconstruction is complete. In this example, the region 680 – 700°C is taken because the RAS transients of heating and cooling meet here.

The results of a variety of such deoxidation experiments are plotted in fig. 7.17. It includes the data from sec. 7.5. We used epi-ready substrates and wafers with an oxide layer that was freshly prepared (after deoxidation and buffer growth) by oxidation in air for 1 h. The horizontal axis denotes the heat of formation for the bulk crystal, which corresponds to the binding energy.

The typical temperature ranges that were determined for oxide desorption are 240 – 480°C for InAs, 300 – 600°C for GaAs, 370 – 530°C for InP and 470 – 680°C for GaP.

As in the example in fig. 7.16, it was found that the formation of a fully reconstructed surface as sensed by RAS occurs at substantially higher temperatures than the completion of oxide desorption as indicated by SE.

A certain trend, at least for the freshly oxidised samples, is the increase of the onset and the end of oxide desorption with the binding energy of the corresponding bulk. For GaAs and InP epi-ready wafers, the deoxidation as determined by SE is complete at 500°C and 480°C.

Knorr [8] found that the oxide desorption from GaAs as measured with SE starts at approx. 250°C and is finished at 400°C. These temperatures are by 100°C lower than determined in this work, which could be explained by the wet-chemical treatment of the samples in [8]. The temperature range for InP as determined by Knorr is 380−470°C, which is closer to the results of this work.

Meyne *et al.* [102] determined values of 500°C (GaP) and 300°C (GaAs) for the onset of oxide desoption under group V flux, but with different parameters and precursors. This agrees well with our findings, although the values for GaAs seem to vary strongly, depending on the age and manufacturer of the substrate. The oxide desorption of GaAs was also measured by Allwood *et al.* [103] with surface photoabsorption (SPA). They determined 260 – 300°C for the onset and 410 – 430°C for the completion of oxide desorption under tertiarybutylarsine (tBAS) flux using a temperature ramp rate of 40°C/min. The reason for these relatively low values might be the lower decomposition temperature of tBAs compared to AsH_3.

In a publication by Schröder *et al.* [104] the desorption temperatures of the arsenic oxides was determined to 320 – 350°C while gallium oxide requires temperatures of

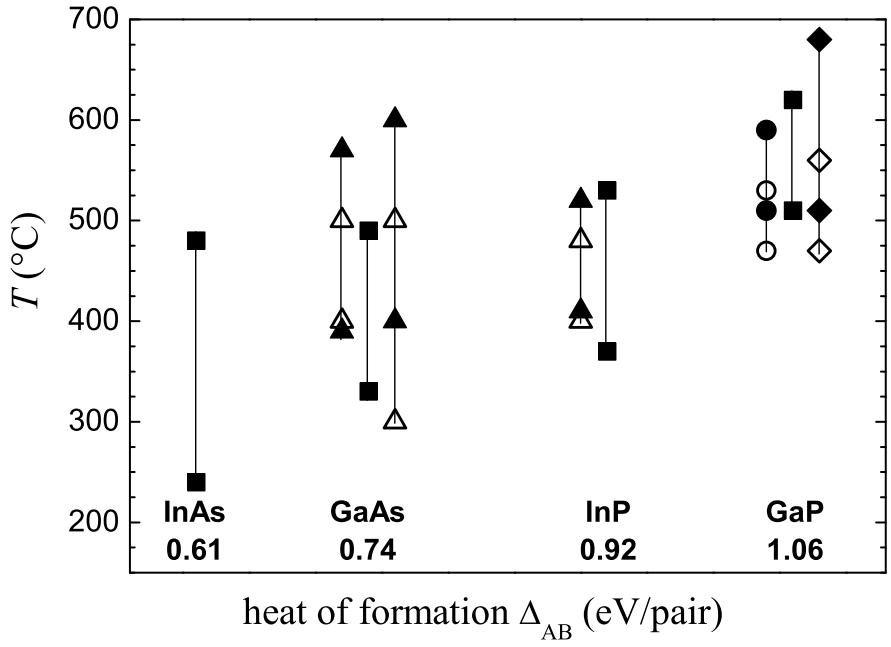

Figure 7.17: *Summary of a variety of deoxidation experiments. Shown is the start (lower symbol) and the end (upper symbol) of oxide desorption (SE, empty symbols) and formation of a reconstruction (RAS, full symbols) as a function of binding energy. The diamond symbol denotes the GaP sample from fig. 7.16 (wet-etched). The oxide layer of all other samples except for the triangles (epi-ready wafers) was prepared by oxidizing a previosly deoxidised wafer for 1 h in air. The temperature ramp during deoxidation was 25°C/min except for the measurements with square symbols (20°C/min). Group-V ambient pressures were 100 Pa AsH_3 and 200 Pa PH_3, respectively.*

~ 600°C to desorb. The relatively high temperatures for the completion of oxide desorption from epiready GaAs (around 600°C) can thus be explained by the presence of Ga-rich oxide in the layer. This value is is lower (500°C) when freshly oxidised samples are used.

7.7 Determination of activation energy

The usual way of removing the oxide layer thermally is to heat the sample with a certain (maximum) heating power until the final temperature (600 – 750°C for III-Vs) is reached. This procedure makes comparisons between different growth systems

complicated. To simplify comparison, it is better to study the oxide desorption and to determine the activation energy of the oxide desorption process.

In this part only SE data are evaluated because they allow a quantitative description of the desorption via the thickness of the oxide layer.

Oxide desorption at fixed temperature was studied for epi-ready InAs (220−300°C), GaAs (340 − 410°C) and InP (360 − 440°C) wafers. The increase of $\langle\epsilon_2\rangle$ was monitored with ellipsometry at 4.4 eV (InAs), 4.8 eV (GaAs) and 4.7 eV (InP). These photon energies correspond to the respective E_2 interband transition at room temperature and mark the points in the spectra where $\langle\epsilon_2\rangle$ reacts most sensitively to thin oxide layers or roughness (see spectra in sec. 7.2).

The oxide layer thickness was calculated from $\langle\epsilon_2\rangle$ at the corresponding E_2 energy by simulating a layer of EMA roughness (as described in sec. 7.2.1) with varying thickness and determining a fourth-order polynomial function that converts $\langle\epsilon_2\rangle$ into an oxide layer thickness.

7.7.1 InP

The oxide desorption from InP was studied at temperatures of 360, 380, 400, 420 and 440°C. The temperature was increased from room temperature to the final temperature as fast as possible and then held constant during the whole measurement. The group-V ambient (200 Pa PH_3) was not switched on until the final temperature was reached.

The oxide layer thickness decreases with time from an initial value to a final (lower) level of oxide thickness/roughness. This is shown for two of the five temperatures in fig. 7.18. The presence of phosphine promotes the reduction of the oxide layer drastically. This can be explained by surface etching by hydrogen radicals from the hydrazine source.

The next question that arises is which function must be used to describe the reduction of the oxide layer thickness correctly. It was found empirically that the best fit of the oxide desorption curves is obtained by using the dynamic law of a second-order reaction [105]:

$$d_{\mathrm{ox}}(t) = d_\infty + \frac{1}{vt + \frac{1}{d_0}} \quad . \tag{7.4}$$

The sum $d_\infty + d_0$ represents the starting layer thickness at $t = 0$. The quantity d_∞ describes the residual roughness after oxide desorption, which is typically some tenths of a nanometer. The quantity v is called desorption constant and describes the reaction velocity. The values of d_∞ and d_0 vary strongly with the age and history of the sample.

In fig. 7.18 two typical oxide desorption curves are shown. The fit with (7.4) is in good agreement to the experimental data .

The logarithm of the fitted desorption constant v is plotted as a function of inverse temperature in a so-called *Arrhenius plot* (fig. 7.19). One value of v (at 440°C) is plotted in parentheses because the oxide layer of this sample was unusually thick and the obtained desorption constant was much lower than expected for this temperature. The experiment was repeated for this temperature with a different sample. The first value was ignored in the further evaluation.

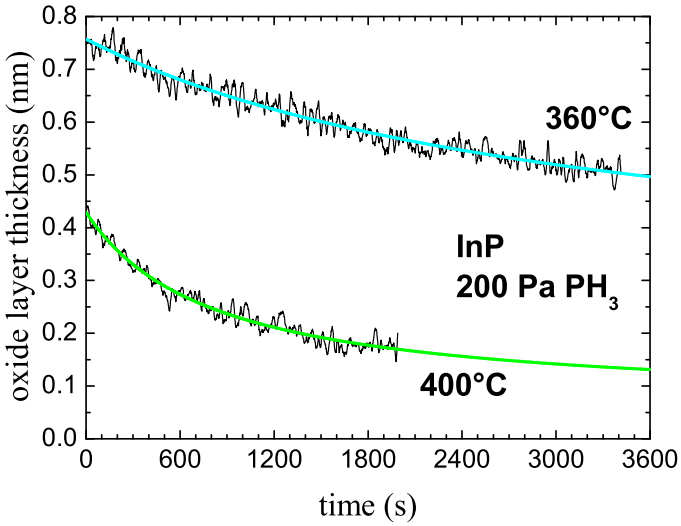

Figure 7.18: *Thermal deoxidation of InP at 360 and 400°C, plotted as oxide layer thickness versus time. The smooth curves are fits according to (7.4).*

With the exception of the dismissed value, the desorption constant increases with rising temperature. From the slope of the fitted linear function in fig. 7.19 the activation energy E_a can be calculated, because the Arrhenius equation (cf. [105]) states that

$$\ln v = \ln A - \frac{E_a}{kT} \quad . \tag{7.5}$$

A is a pre-exponential factor and k is the Boltzmann constant. The obtained result for the slope (units of J/K) must be multiplied by $1000 \times \ln 10 \times k/e = 0.1984$ to obtain the activation energy in units of eV (e is the electron's charge). The factor $\ln 10$ appears because the ordinate in fig. 7.19 has a decadic logarithmic scale.

From the slope of the Arrhenius plot in fig. 7.19 an activation energy of $E_a = 1.42 \pm 0.18\,\text{eV}$ is obtained for InP. The pre-exponential factor was determined to $A = 8.2 \pm 1.3\,\text{nm/s}$.

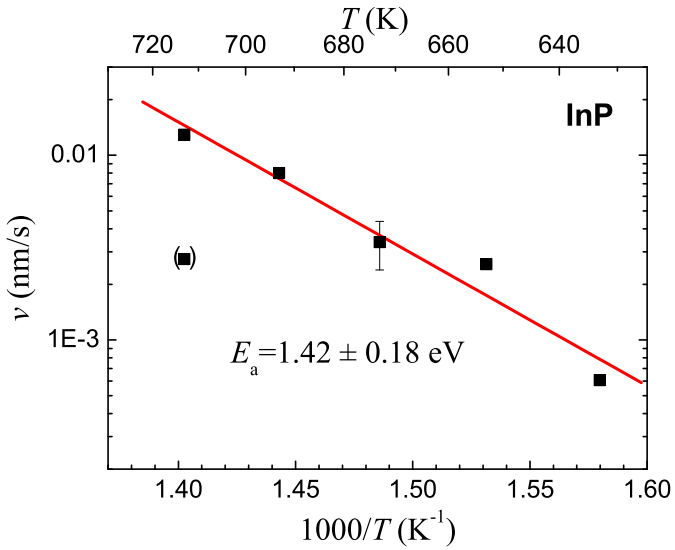

Figure 7.19: *Arrhenius plot of the thermal deoxidation of InP. The slope of the linear fit corresponds to the activation energy E_a. The value in parentheses was excluded from the fitting procedure (see text). The error of v was estimated from variations of the starting point of the desorption transients.*

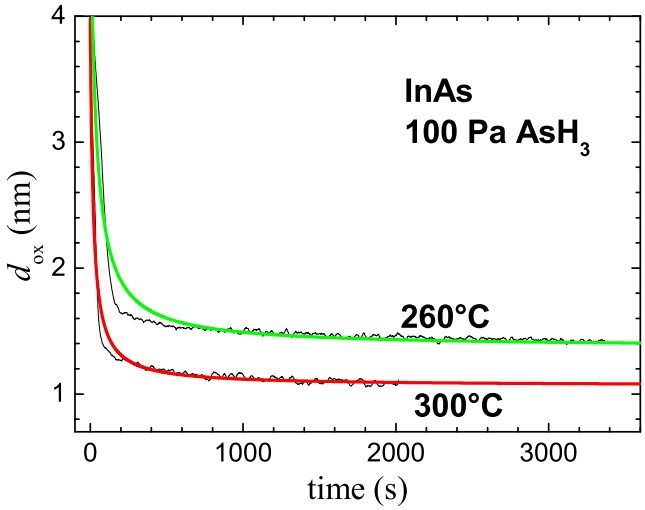

Figure 7.20: *Oxide layer thickness as a function of time for the thermal deoxidation of InAs at* 260 *and* 300°*C. The smooth curves are fit results of a second order reaction.*

7.7.2 InAs

The thermal deoxidation of InAs was studied at five different temperatures: 220, 240, 260, 280 and 300°C. The evaluation of the data follows the procedure in sec. 7.7.1. The group V ambient pressure was 100 Pa AsH_3.

Fig. 7.20 shows two typical deoxidation transients and the corresponding fit functions. It must be noted that the fit functions do not agree as well to the experimental values as in the case of InP. There are actually two processes occuring, as can be seen more clearly in the transient graph for 220°C (7.21): a first process (I) with $v_I = 0.006$ nm/s is followed by a second (II), slower one with $v_{II} = 0.003$ nm/s. At higher temperature the first, fast process leads to a very rapid initial change of the oxide thickness. The fit function (7.4) cannot describe this behaviour too well but was retained unchanged in order to allow a comparison to InP and GaAs.

The presence of two different processes could be an indication for thin film of water on the surface during phase I that modifies the desorption characteristics. In phase II (and all other experiments at higher temperatures) the water is already desorbed. A proposition to verify this assumption is to temper the sample at ≈ 200°C before performing the activation energy experiments. The two processes can also by explained by assuming different types of oxides with different desorption behaviour.

For the determination of E_a only the second process was considered. The occurence of desorption processes with different time constants in one transient measurement was also found for GaAs and is discussed in sec. 7.7.3.

The obtained desorption constants increase with temperature, as was expected. They were plotted in an Arrhenius diagram (fig. 7.22). The activation energy was

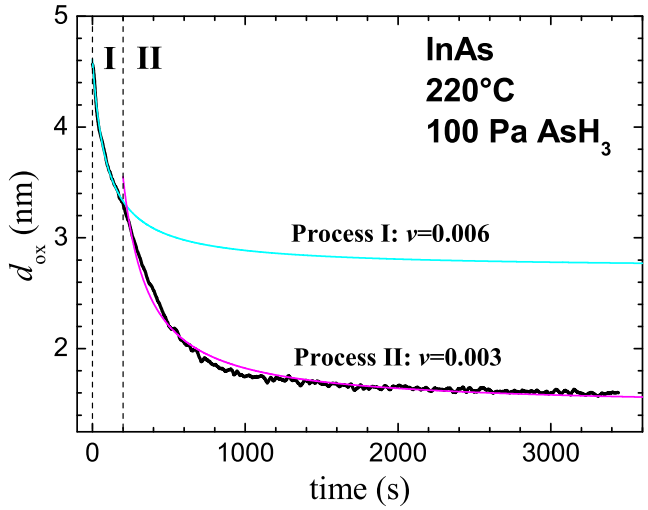

Figure 7.21: *Thermal deoxidation of InAs at 220°C. Two different processes (I and II) can be distinguished.*

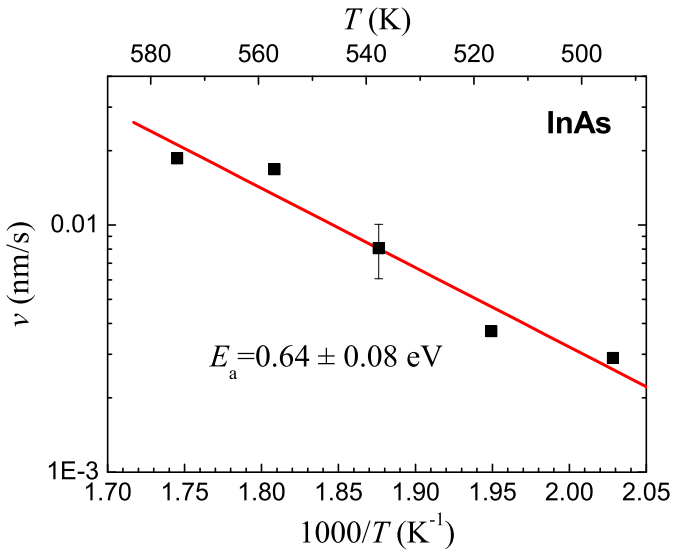

Figure 7.22: *Arrhenius plot of the thermal deoxidation of InAs.*

determined to 0.64 ± 0.08 eV. For the pre-exponential factor a value of $A = 3.9 \pm 0.8$ nm/s was calculated.

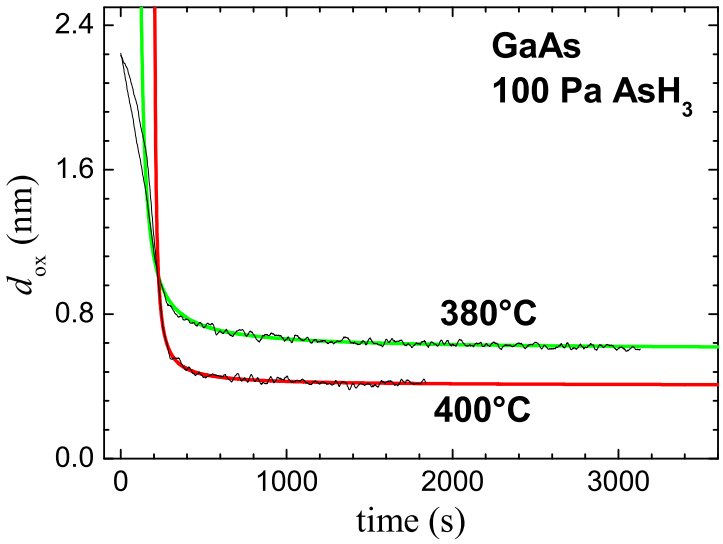

Figure 7.23: *Oxide layer thickness as a function of time for the thermal deoxidation of GaAs at 380 and 400°C. The smooth curves are fit results of a second order reaction.*

7.7.3 GaAs

The thermal oxide desorption from GaAs was studied at seven different temperatures: 320, 340, 360, 380, 390, 400 and 410°C. The arsine pressure was 100 Pa.

Two typical deoxidation transients and the corresponding fit functions are shown in fig. 7.23. While the agreement is good for the major part of the graphs, there are strong deviations at the beginning of the desorption process. This seems to be a characteristic feature of GaAs and InAs (cf. fig. 7.21).

For temperatures below 350°C, the process at the beginning (named process I) can be fitted separately with the same fit function. This is shown in figs. 7.24 and 7.25. At higher temperatures the slope of process I is very steep and an unambiguous determination of the desorption rate is difficult.

Apart from the fitted processes I and II, in fig. 7.24 a third process (before I) can be distinguished. This is maybe due to the presence of a thin water film on the surface.

It is difficult to understand the nature of the different processes. It can most probably be explained by the chemical mixture of the oxide. While there is only few literature available concerning the oxides of InAs, InP and GaP, the material system of GaAs and its oxides is covered better.

Thurmond *et al.* studied the oxidation of GaAs [88, 106] and found that the equilibrium interfacial phases consist of Ga_2O_3 and elemental amorphous As for O_2 as oxidant. Oxide phases from electrochemical and plasma oxidation may also contain As_2O_3 in the interfacial region.

McKnight *et al.* [107] investigated anodic oxides on GaAs and discovered that Ga_2O_3 is uniformly distributed in the oxide film while As_2O_3 is depleted near the

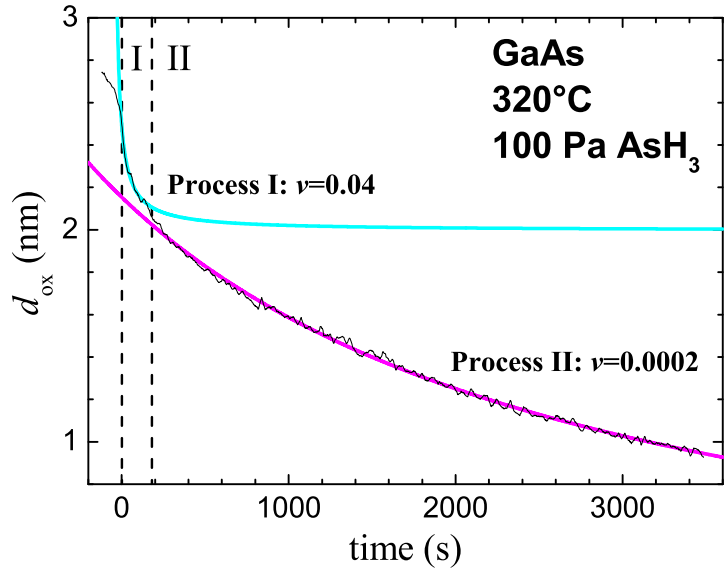

Figure 7.24: *Thermal deoxidation of GaAs at* 320° *C. Two different processes (I and II) can be distinguished.*

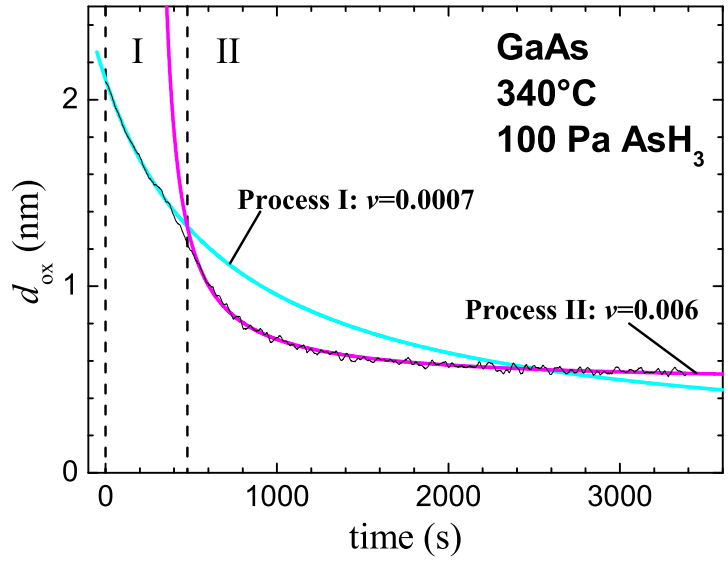

Figure 7.25: *Thermal deoxidation of GaAs at* 340° *C. Two different processes (I and II) can be distinguished.*

surface and enhanced near the interface to the bulk. Near the interface, the ratio of arsenic over oxygen even exceeds the stoichiometric ratio of 2:3.

Grunthaner *et al.* [108] examined the chemical depth profile of the GaAs/native oxide interface and found that the Ga:As ratio is 2:1 at the surface and reaches values

as high as 10:1 at the interface to the bulk. Furthermore they detected elemental As at the interface.

Schröder *et al.* [104] described the phases of GaAs oxide by a multilayer model: Ga_2O_3 and As_2O_3 mixed with $GaAsO_4$ on top. The desorption temperatures of the arsenic oxides was determined to 320 – 350°C. For oxidised gallium a temperature of 600°C was found.

The TPD of GaAs (fig. 7.1a) predicts that elemental As, Ga_2O_3, As_2O_3, $GaAsO_4$ and As_2O_5 can be expected in the oxide layer.

The literature results are sometimes contradictory but can be summarised as follows:

a.) The oxide layer consists of Ga_2O_3 and As_2O_3.

b.) Near the surface, the As concentration is reduced (more Ga_2O_3).

c.) Near the interface to the bulk, the amount of As is increased (even elemental/amorphous As?).

d.) The arsenic oxide desorbs at lower temperatures than gallium oxide.

From the order of occurrence in the oxide layer, the first process is probably the desorption of a more Ga-rich oxide. The second process could then be identified with the removal of an As-rich oxide. One would expect that process II is faster because the heat of formation of As_2O_3 is −156 kcal/mol, which is considerably lower than that of Ga_2O_3 (−257 kcal/mol) [109]. This is only the case in fig. 7.25. However, this discussion is highly speculative because the chemical structure of epiready oxide layers is a trade secret of the wafer manufacturers and no publications are available.

The obtained desorption constants of process II (which were calculated for all temperatures studied) were plotted in an Arrhenius diagram (fig. 7.26). The value obtained for 320°C was not used for the determination of the activation energy because it is one order of magnitude below the value that can be expected from the progression of the other datapoints.

An activation energy of 1.12 ± 0.2 eV is obtained for GaAs. The pre-exponential factor is $A = 7.0 \pm 1.6$ nm/s.

In [8] an activation energy of 0.8 eV was determined for GaAs oxide grown by ozonisation (O_2 and UV light).

Allwood *et al.* [110] determined the activation energy of (probably) Ga_2O_3 to 2.0 eV, but they deoxidised under H_2 flux only (no group V-precursor). This indicates that the large amount of atomic H from the hydrazine source accelerates the oxide desorption drastically.

The activation energies as well as the pre-exponential factors of (7.5) for the three semiconductors studied are listed in table 7.2. The values of E_a follow the trend of the binding energies of the substrate semiconductor material.

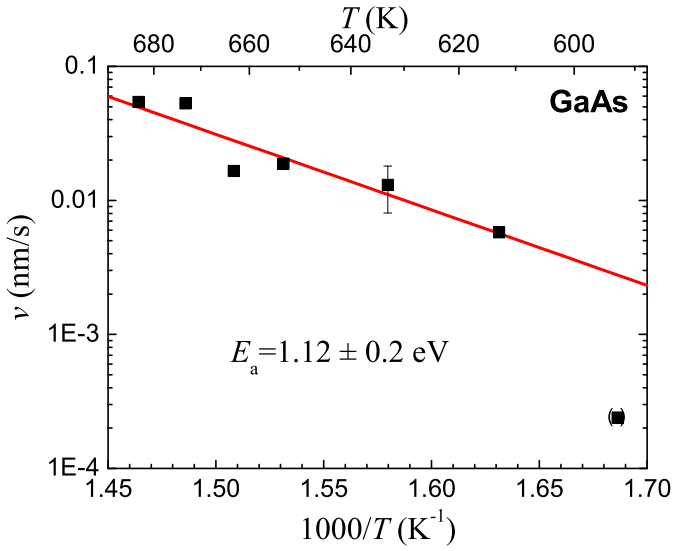

Figure 7.26: *Arrhenius plot of the thermal deoxidation of GaAs. The value in parentheses (at 320°C) was not regarded for the fit process.*

Substance	InAs	GaAs	InP
A (nm/s)	3.9	7.0	8.2
E_a (eV)	0.64	1.12	1.42
Δ_{AB} (eV/pair)	0.61	0.74	0.92
no. of processes	2	3	1

Table 7.2: *Pre-exponential factors A and activation energies E_a for the oxide desorption as determined in sec. 7.7. Shown for comparison is the binding energy Δ_{AB} of the corresponding substrate material. The last row describes the maximum number of different processes that have been observed during desorption of the respective oxide.*

8. Summary and outlook

In this work, the optical techniqes RAS and SE were applied to *in situ*-monitoring of processes during MOVPE of III-V semiconductors.

After introducing briefly the growth technique of MOVPE and the optical methods SE and RAS, different approaches for correcting systematic errors in RAS measurements were explained (so-called window correction). Furtermore, two methods for calibrating the anisotropy scale of RAS setups were presented. A calibration can be achieved by measuring the anisotropy of a birefringent material with known ordinary and extraordinary refractive index, e.g. crystalline quartz. A further possibility is to make use of the influence of the polariser's angle on the measured signal.

Multichannel RAS

To allow spectral RAS measurements at sub-second temporal resolution, the design of a multichannel RAS system was developed. A setup was built that allows standard RAS measurements (with monochromator) and multichannel detection (with spectrograph) independently and simultaneously. This is made possible by using a special analyser prism that has an extra beam output.

The multichannel detection unit is designed for the typical spectral range of 1.5 – 5 eV and has a resolution of 8 spectral channels. The setup was later upgraded to allow the measurement of 16 (out of 32) spectral channels. For this upgrade, a special 32-channel photomultiplier detector with integrated amplification was developed.

In order to measure, display and evaluate the multichannel RAS data a software was written in LabWindows.

Concerning a general problem of multi-wavelength RAS measurements, the correction of the wavelength-dependent retardation of the photoelastic modulator (PEM), a solution was proposed.

The multichannel RAS was benchmarked against high-resolution spectra of static III-V-surfaces. It was found that the key features of the spectra can be well detected, especially at high temperatures where the structures are thermally broadened.

The dynamic capabilities of the setup were tested by studying two fast processes: monolayer oscillations during growth of GaAs and the self-organised formation of InAs quantum dots on GaAs(001). From the spectra of the GaAs monolayer oscillations it could be acknowledged that the surface oscillates between an smooth As-rich surface (phase III, adsorbed methyl groups) and a Ga-rich phase II surface. The multichannel spectra taken during evolution of the InAs quantum dots revealed the formation of an InAs layer and the subsequent change from 2D to 3D growth. While the low-energy spectral channels deliver information about the 2D-3D transition, the high-energy range indicates the morphology change of the surface. The different stages of quantum dot formation could be fully monitored at high temporal resolution.

Doping and RAS

To understand the influence of the doping concentration on the RAS spectra of III-V-semiconductors, the mechanism and the order of magnitude of the linear electro-optic effect (LEO) was discussed in detail. The connection between the internal electric field and the concentration of free carriers could be made by the Schottky model of an abrupt interface. A comprehensive derivation for the relationship between the change of the RAS signal and the free carrier concentration was given. The possibility of measuring the doping concentration by multichannel RAS in real time was demonstrated for Si-doped GaAs.

Reported for the first time was the effect of damped RAS oscillations in GaAs and InP induced by a change of the doping concentration during growth. The period and the damping of the oscillations corresponds to that of the well-known Fabry-Pérot reflectance oscillations (FPOs) measured during heteroepitaxial growth. In contrast to FPOs, the oscillation cannot be detected in reflectance.

The growth rate determined from these oscillations was found to correspond to the growth rate measured *ex situ* and *in situ* at lower temperatures. The magnitude of the oscillations depends on the change of doping concentration (doping contrast) while the sign shows the direction of the change of dopant concentration (from higher to lower or vice versa). The effect was demonstrated for GaAs:Si, GaAs:Zn, InP:Si and InP:Zn. A theoretical model for the calculation of these oscillations was derived and tested by comparing to measurements and numerical thin-film simulations. It was found that the oscillations can be described by a four-layer model with one anisotropic layer.

These growth oscillations are the only optical method to measure a homoepitaxial growth rate at temperatures above 550°C *in situ*. It is expected that this effect will find its application in the *in situ* control of device growth. To go one step further, it is also possible to achieve *in situ* doping profiling with RAS by combining the determination of the doping concentration and the growth rate measurement.

Oxide desorption

To understand the process of oxide desorption from InAs, InP, GaAs and GaP in MOVPE prior to growth, several experiments were performed to study the temperature behaviour of the desorption process and to determine the activation energy.

The thickness of the oxide layer at high temperatures was approximated by using the Bruggeman model of a rough surface with a guest/host fraction that was determined separately for each semiconductor material.

During deoxidation, the RAS signal showed the development from the distinctive spectrum of an oxidised surface towards that of the corresponding reconstruction. SE was employed to determine the thickness of the oxide layer and the residual roughness. It was found that the SE signal reaches steady conditions (except for the influence of temperature) before the formation of the reconstruction as sensed by RAS is complete.

Typical temperature ranges for oxide desorption in MOVPE were determined to 240 – 480°C (InAs), 300 – 600°C (GaAs), 370 – 530°C (InP) and 470 – 680°C (GaP). These values roughly follow the trend of the binding energies of the substrate material.

By performing oxide desorption experiments at various fixed temperatures, the activation energy for thermal oxide desorption under group V ambient could be determined for InAs (0.64 eV), GaAs (1.12 eV) and InP (1.42 eV).

Understanding the processes during desorption and formation of III-V semiconductor oxides is a research goal that is far from being achieved yet. Most publications in this field (with this work being no exception) cover only few aspects of the whole picture. A comprehensive study covering aspects of morphology, oxide bonding structure, chemical composition and the influence of different (pre-)treatments of the surface not only for GaAs but also other III-V semiconductors is necessary.

9. Zusammenfassung

Diese Arbeit beschreibt die Anwendung von optischen *in situ*-Meßtechniken (Reflexions-Anisotropie-Spektroskopie, RAS, und spektroskopische Ellipsometrie, SE) auf Prozesse, die beim Wachstum von III-V-Halbleitern wie GaAs, InP, InAs und GaP in der metallorganischen Gasphasenepitaxie (MOVPE) von Bedeutung sind. Besonderes Augenmerk liegt dabei auf der Bestimmung der Konzentration der freien Ladungsträger (Dotierung) und der Untersuchung des thermischen Desorptionsverhaltens der III-V-Oxide.

Ein großer Teil der Arbeit befasst sich mit der Entwicklung und dem Aufbau einer Mehrkanal-RAS, mit der die Messung von RAS-Spektren in Sekundenbruchteilen möglich wird. Anhand von Benchmark-Messungen wurde gezeigt, daß die spektrale Auflösung für die Anwendung in der Epitaxie hinreichend genau ist.

Zur Demonstration der Messung von Spektren mit hoher Zeitauflösung wurden RAS-Monolagenoszillationen beim Wachstum von GaAs untersucht und gezeigt, daß die Oberfläche periodisch zwischen einer relativ glatten, mit Methylgruppen belegten Oberfläche (Typ III) und einer gestuften, galliumreichen Oberfläche (Typ II) oszilliert. Desweiteren wurde ein nichtreversibler Prozeß, das Wachstum von InAs-Quantenpunkten auf GaAs, untersucht. Hier wurde gezeigt, daß die Mehrkanal-RAS geeignet ist, um sowohl den 2D-3D-Übergang als auch die anschließende Morphologieänderung der Oberfläche mit hoher Zeitauflösung zu detektieren.

Für die Messung der Dotierung wurde der Zusammenhang zwischen dem durch die Dotierung erzeugten internen elektrischen Feld und der gemessenen Anisotropie untersucht (linearer elektro-optischer Effekt). Es wurde gezeigt, daß die Dotierungsbestimmung mit Mehrkanal-RAS möglich ist.

Erstmals wurde zudem ein Effekt beschrieben, der während des Wachstums von aufeinanderfolgenden, unterschiedlich dotierten Schichten von z.B. GaAs oder InP auftritt: das RAS-Signal oszilliert ähnlich wie bei den aus der Reflektometrie bekannten Fabry-Pérot-Oszillationen. Diese Oszillationen können ausgenutzt werden, um *in situ* eine Wachstumsrate in der Homoepitaxie zu bestimmen, was sonst nur in einem stark eingeschränkten Wachstumsparameterbereich und nur über kurze Zeit möglich ist (Monolagensozillationen). Zusammen mit der Dotierungsbestimmung kann dieser Effekt benutzt werden, um *in situ* ein Dotierprofil zu erstellen. Zum Verständnis des Effekts der sogenannten Dotierungsoszillationen wurde eine theoretische Beschreibung entwickelt.

Zur Untersuchung der thermischen Desorption der III-V-Oxide in der MOVPE wurden mehrere Versuchsreihen durchgeführt. Dabei wurden (bei konstanter Temperaturzunahme) Temperaturen bestimmt, bei denen die Ausbildung einer rekonstruierten Oberfläche einsetzt bzw. abgeschlossen ist (RAS) bzw. die Reduktion der Oxidschichtdicke einsetzt und abgeschlossen ist (SE). Diese Temperaturen korrelieren mit der Bindungsenergie des entsprechenden III-V-Halbleiters. Es wurde außerdem herausgefunden, daß die Ausbildung der Rekonstruktion erst deutlich nach dem Zeit-

punkt abgeschlossen ist, bei dem in den SE-Transienten bereits keine Änderungen mehr sichtbar sind.

Die Aktivierungsenergie der Oxiddesorption für InAs, GaAs und InP wurde mit SE zu 0,64 eV, 1,12 eV und 1,42 eV bestimmt. Auch die Aktivierungsenergie steigt mit der Bindungsenergie des entsprechenden Volumenhalbleiters an.

10. Acknowledgements

To the success of this work a large number of people have contributed. I would like to use this space to express my gratitude to them.

First of all, I would like to thank Prof. Wolfgang Richter for supervising this work, for pushing discussions and giving useful hints. I am grateful to Prof. Norbert Esser for his willingness to referee this work. Dr. Markus Pristovsek I would like to thank for his help as well as his support and interest in this work.

Dr. Florian Poser and Stefan Weeke did many MOVPE runs for my experiments – thank you. Thanks also go to Engelbert Eder for building large parts of the electronics of the multichannel RAS. I would also like to mention Christof Maerker for all the daily help (and the inevitable discussions about transcendental topics) and the workshop of the institute for building mechanic parts for the multichannel RAS. I appreciate the help of Dr. Martin Zorn at the FBH who did the C-V measurements and was open for discussions about the doping oscillations. I also want to thank Dr. Thomas Zettler who pushed the idea of building a multichannel RAS.

I am grateful to Dr. Christoph Cobet, Dr. Kolja Haberland and Dr. Karsten Fleischer for their numerous help and discussions concerning (*in situ*) optics. Dr. Torsten Schmidtling has always been a treasue trove for solving technical problems. He was always ready to help – thank you. I want to thank Dr. Patrick Vogt for proof-reading the manuscript and being a valuable source of information, discussions and fun. I would also like to mention Claudia Hinrichs and Angela Berner, the administrative backbone of the group. Many thanks go to Dr. Karsten Fleischer, Dr. Florian Poser, Raimund Kremzow and Martin Leyer for sharing the ups and downs of maintaining a computer network. Dr. Massimo Drago I want to thank for bringing Italy and Germany closer together. He has always been a help and a source of fruitful discussions, not solely about physics.

The good atmosphere in the workgroup was one reason for me to join it for my diploma thesis, a decision I never regretted. Thanks to all the unmentioned members!

I also appreciate the interest and help of my fellow students and friends Dr. Alexander Rack, Frank Kallmeyer and Sebastian Raasch.

I would like to thank my parents for supporting my studies at the TU and in Glasgow. Finally I want to say thanks to my fiancée Christine for all her loving support through the years.

A. Appendix

A.1 Conversion between different RAS systems

The first RAS systems built [15, 16, 21] were not able to measure $\Delta r/r$ (r: complex amplitude reflectance) but only $\Delta R/R$ (R: intensity reflectance, real) because they used a rotating sample and only one polarising prism. Between the real part of $\Delta r/r$ and $\Delta R/R$ a conversion can be made, which is useful to know when comparing RAS spectra of different systems. The relation between intensity and amplitude reflectance is

$$R = |r|^2 = \mathrm{Re}(r)^2 + \mathrm{Im}(r)^2 \quad . \tag{A.1}$$

We consider the real part of $\Delta r/r$ and multiply with the complex conjugate of the denominator:

$$\mathrm{Re}\left(\frac{\Delta r}{r}\right) = \mathrm{Re}\left(2\frac{r_a - r_b}{r_a + r_b}\right) \tag{A.2}$$

$$= \mathrm{Re}\left(2\frac{(r_a - r_b)(r_a^* + r_b^*)}{(r_a + r_b)(r_a^* + r_b^*)}\right) \tag{A.3}$$

$$= \mathrm{Re}\left(2\frac{|r_a|^2 - |r_b|^2)}{|r_a|^2 + |r_b|^2 + r_a r_b^* + r_b r_a^*)}\right) \quad . \tag{A.4}$$

Taking into account that $r_a \approx r_b$, in all the sum terms we can set the two quantities equal:

$$\mathrm{Re}\left(\frac{\Delta r}{r}\right) \approx \mathrm{Re}\left(2\frac{|r_a|^2 - |r_b|^2)}{|r_a|^2 + |r_b|^2 + |r_a|^2 + |r_b|^2}\right) = \mathrm{Re}\left(2\frac{|r_a|^2 - |r_b|^2)}{2|r_a|^2 + 2|r_b|^2}\right) \quad . \tag{A.5}$$

The fraction inside the parentheses is now a real number, so the operator Re can be omitted:

$$\mathrm{Re}\left(\frac{\Delta r}{r}\right) \approx 2\frac{|r_a|^2 - |r_b|^2}{2|r_a|^2 + 2|r_b|^2} = \frac{|r_a|^2 - |r_b|^2}{|r_a|^2 + |r_b|^2} \tag{A.6}$$

$$= \frac{R_a - R_b}{R_a + R_b} = \frac{1}{2}\frac{\Delta R}{R} \tag{A.7}$$

Thus the RAS signal calculated from intensity reflectance is approximately twice the real part of the amplitude reflectance RAS signal:

$$\frac{\Delta R}{R} \approx 2\,\mathrm{Re}\left(\frac{\Delta r}{r}\right) \quad . \tag{A.8}$$

The error that is made with this simplification is very small for typical orders of magnitude of the RAS signal. For RAS units around 10 (10×10^{-3}) the difference is $\approx 0.005\%$ (fig. A.1). Even for a huge anisotropy of 100 units the error is only 0.5%.

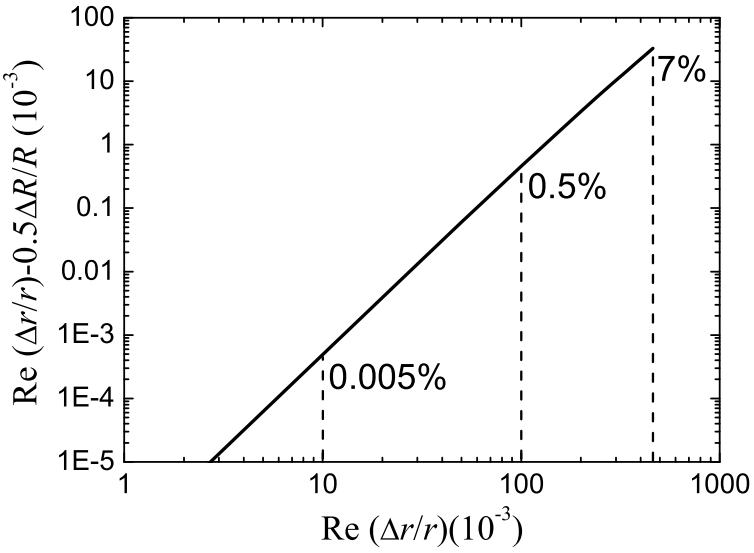

Figure A.1: *Difference between* $\mathrm{Re}(\Delta r/r)$ *and* $0.5\Delta R/R$ *as a function of* $\mathrm{Re}(\Delta r/r)$. *The values were generated assuming* $r_b = 0.5 + 0.5i$, $\mathrm{Im}(r_a) = 0.5$ *and* $\mathrm{Re}(r_a) \in \{0.5 \ldots 1\}$.

A.2 Standard etching recipes

The following recipes were used (if necessary) for the etching of the substrates.

- 3× rinsing in acetone (degreasing)
- 3× rinsing in isopropanole (solubilises acetone, accustoms the sample to water)
- 2 min rinsing in ultrapure water
-

GaAs	GaP	InP
1 min 75% H_2SO_4	1 min 75% H_2SO_4 $T = 80°C$	1 min 75% H_2SO_4
2 min 75% H_2SO_4 + 30% H_2O_2	2 min 75% H_2SO_4 + 30% H_2O_2 $T = 80°C$	10 min 75% H_2SO_4 + 30% H_2O_2
30 s 25% H_2SO_4	30 s 25% H_2SO_4	30 s 25% H_2SO_4

- 2 min rinsing in ultrapure water
- dry-blowing with nitrogen

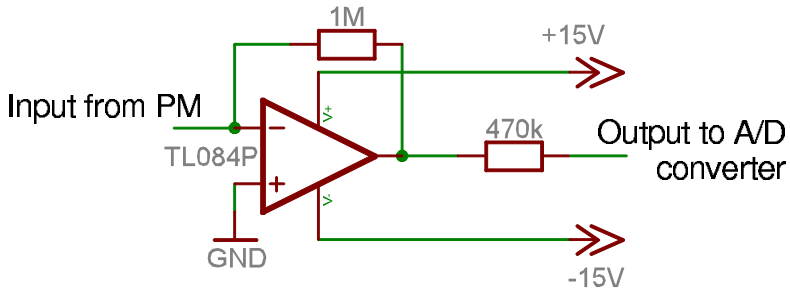

Figure A.2: *Circuit for the amplification of the photomultiplier signal. Only one channel is shown.*

A.3 Photomultiplier sensor head

The challenge in building this compact sensor head was to fit all components (photomultiplier tube, high voltage power supply, amplifiers for 32 channels) onto one PCB of Euro format (160 × 100 mm). This allows to keep the signal wires simple (no sophisticated screening required, output signals in the range of volts).

The high voltage for the photomultiplier tube (Hamamatsu H7260-04) is generated by a compact power supply C7410 also available from Hamamatsu. The position of the switch (JP4 in fig. A.3) determines whether the high voltage is set by a potentiometer (JP5) or by an external voltage (0 – 5 V). The whole sensor head requires a voltage of ±15 V (JP3).

The current delivered by the photomultiplier must be converted into a voltage. This is the task of the circuit in fig. A.2. The feedback resistor (1 MΩ) determines the amplification factor. The IC *TL084P* incorporates four single op-amps, i.e. four channels can be processed by one chip. The complete electronics uses 8 of these ICs.

After conversion and amplification, the signal of all 32 channels are available at two pinhead connectors: JP1 for the odd channels 1 – 31 and JP2 for all even channels (2 – 32).

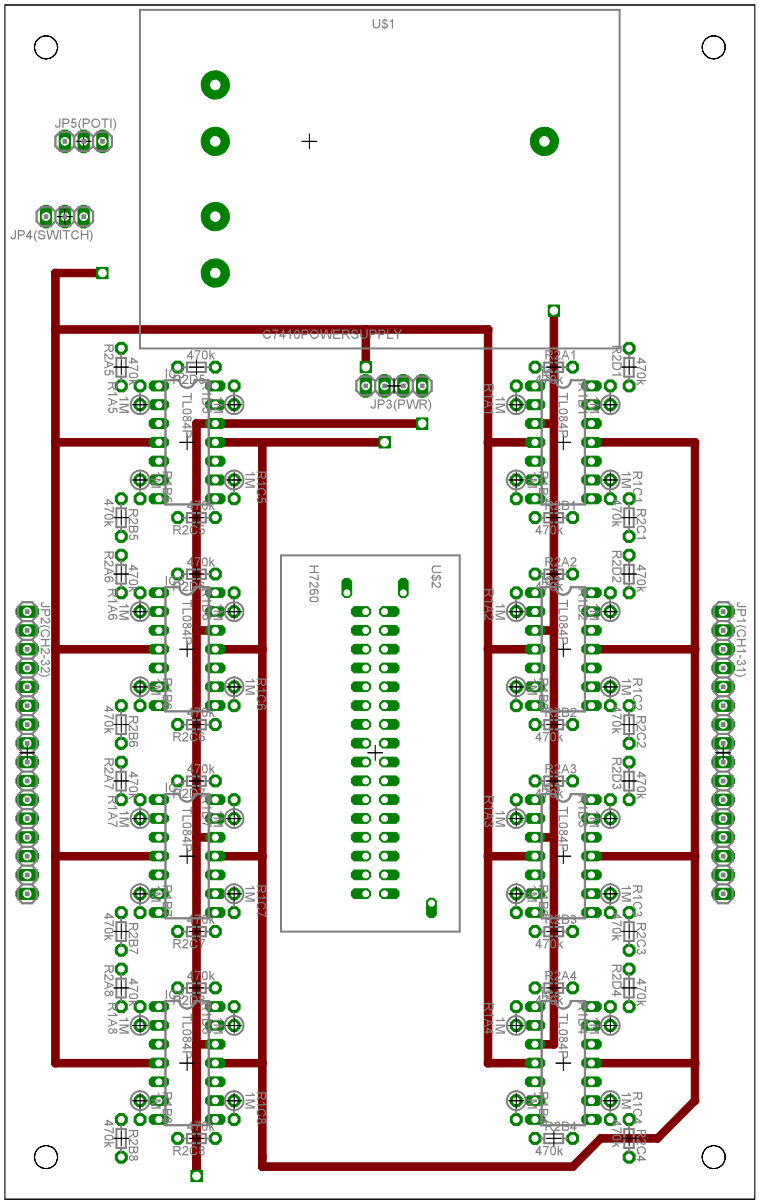

Figure A.3: *Component side of the PCB with components. Dimensions:* 160 × 100 *mm (Euro format).*

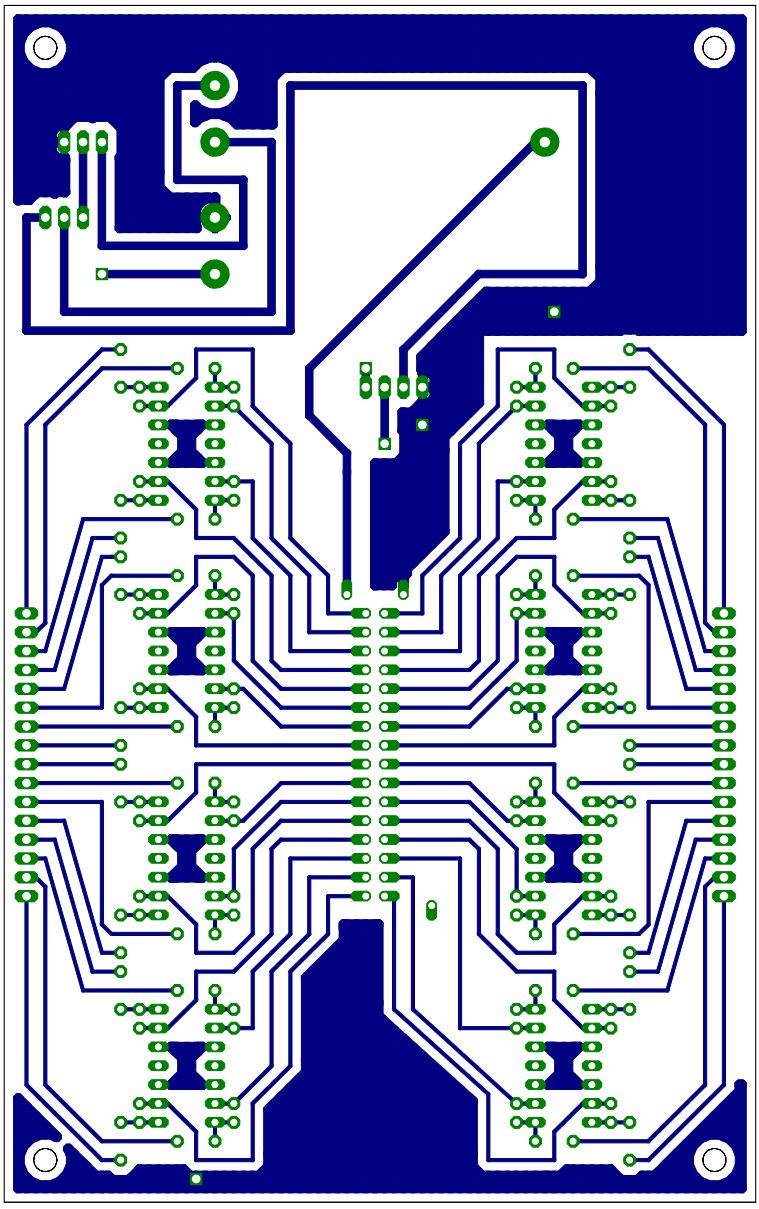

Figure A.4: *Back side of the PCB, viewed from component side (such that the holes are congruent with fig. A.3).*

A.4 Publications and conference contributions

A.4.1 Publications

1. V. Hoffmann, F. Poser, Ch. Kaspari, S. Weeke, M. Pristovsek and W. Richter: *Nitrogen-arsenic exchange processes and investigation of the nitrided GaAs surfaces in MOVPE*, J. Appl. Phys. **272**, p. 30 (2004)

2. Ch. Kaspari, M. Pristovsek and W. Richter: *A fast reflectance anisotropy spectrometer for in situ growth monitoring*, phys. stat. sol. b **242**, p. 2561 (2005)

3. Ch. Kaspari, M. Pristovsek and W. Richter: *Homoepitaxial growth rate measurement using in situ Reflectance Anisotropy Spectroscopy*, J. Cryst. Growth *(in print)*

A.4.2 Conference contributions

1. Ch. Kaspari, F. Poser, J.-T. Zettler und W. Richter: *In situ-Untersuchung von Oberflächenprozessen während der MOVPE mittels FTIR-Spektroskopie*, Frühjahrstagung des AKF der DPG, 11. – 15. 3. 2002, Regensburg, Germany

2. Ch. Kaspari, F. Poser, S. Weeke und W. Richter: *Untersuchung der Precursor-Zerlegung in der MOVPE mittels Infrarot-Fourierspektroskopie*, 17. Workshop des DGKK-Arbeitskreises „Epitaxie von III-V-Halbleitern“, 12./13. 12. 2002, Magdeburg, Germany

3. Ch. Kaspari, F. Poser, S. Weeke and W. Richter: *Investigation of Precursor Decomposition in MOVPE using Fourier Transform Infrared Spectrometry*, Frühjahrstagung des AKF der DPG, 24. – 28. 3. 2003, Dresden, Germany

4. U.W. Pohl, I. Kaiander, Ch. Kaspari, S. Weeke, R. L. Sellin, J.-T. Zettler , D. Bimberg and W. Richter: *Real-time control of quantum dot laser growth by reflectance anisotropy spectroscopy*, EWMOVPE X, 8. – 11. 6. 2003, Lecce, Italy

5. Ch. Kaspari, F. Poser, S. Weeke and W. Richter: *Real-time growth monitoring using multichannel-RAS*, Frühjahrstagung des AKF der DPG, 8. – 12. 3. 2004, Regensburg, Germany

6. Ch. Kaspari, F. Poser, S. Weeke, M. Pristovsek and W. Richter: *Real-time RAS during III-V-MOVPE using a multichannel approach*, ICMOVPE XII, 30. 5. – 4. 6. 2004, Hawaii, USA

7. Ch. Kaspari, M. Pristovsek, S. Weeke and W. Richter: *Deoxidation study of III-V-semiconductors in MOVPE*, 19. Workshop des DGKK-Arbeitskreises „Epitaxie von III-V-Halbleitern“, 9./10. 12. 2004, Freiburg, Germany

8. Ch. Kaspari, S. Weeke, F. Poser, M. Pristovsek and W. Richter: *Multichannel RAS - a versatile means for fast in situ-measurements*, Frühjahrstagung der DPG, 4. – 9. 3. 2005, Berlin, Germany

9. Ch. Kaspari, M. Pristovsek, S. Weeke and W. Richter: *A multichannel RAS setup for fast in situ-measurements*, EWMOVPE XI, 5. – 8. 6. 2005, Lausanne, Switzerland

10. Ch. Kaspari, M. Pristovsek, T. Zettler, M. Zorn and W. Richter: *Homoepitaxial growth rate measurement through in situ Reflectance Anisotropy Spectroscopy*, ICMOVPE XIII, 22. – 26. 5. 2006, Miyazaki, Japan

11. Ch. Kaspari, M. Pristovsek, A. Oestereich and W. Richter: *Deoxidation and Oxidation of III-V-semiconductors in MOVPE*, ICMOVPE XIII, 22. – 26. 5. 2006, Miyazaki, Japan

12. Ch. Kaspari, M. Pristovsek, S. Weeke and W. Richter: *In situ monitoring with multichannel RAS*, International Symposium „Semiconductor Nanostructures“, 7./8. 9. 2006, Berlin, Germany

Bibliography

[1] Walter Miederer, Günther Ziegler, and Richard Dötzer, *Verfahren zum tiegelfreien Herstellen von Galliumarsenidstäben aus Galliumalkylen und Arsenverbindungen bei niedrigen Temperaturen*, Patentschrift No. DE000001176102B, Deutsches Patentamt, 1962/1965.

[2] H. M. Manasevit, *Single-Crystal Gallium Arsenide on Insulating Substrates*, *Appl. Phys. Lett.* **12**, 156 (1968).

[3] Gerald B. Stringfellow, *Organometallic Vapor-Phase Epitaxy: Theory and Practice*, Academic Press, Inc., 2nd edition, 1999.

[4] M. A. Herman, W. Richter, and H. Sitter, *Epitaxy - physical principles and technical implementation*, Springer-Verlag, 2004.

[5] Kolja Haberland, *In situ studies during metal-organic vapor phase epitaxy with respect to III-V device growth*, PhD thesis, TU Berlin, 2002.

[6] G. Bauer and W. Richter, editors, *Optical Characterization of Epitaxial Semiconductor Layers*, Springer-Verlag, 1996.

[7] Martin Zorn, *Optical in-situ studies and on-line growth control of binary and ternary III-V semiconductors with respect to the (001) surface*, PhD thesis, TU Berlin, 1999.

[8] Kerstin Knorr, *Untersuchungen von Grenzflächenprozessen bei der metallorganischen Gasphasenepitaxie von III-V-Halbleitern*, PhD thesis, TU Berlin, 1997.

[9] R. M. A. Azzam and N. M. Bashara, *Ellipsometry and Polarized Light*, Elsevier Science B.V., 1977.

[10] Max Born and Emil Wolf, *Principles of Optics*, Cambridge University Press, 7th edition, 1999.

[11] Jörg-Thomas Zettler, *Characterization of Epitaxial Semiconductor Growth by Reflectance Anisotropy Spectroscopy and Ellipsometry*, *Prog. Crystal Growth and Charact.* **35**, 27 (1997).

[12] Thomas Trepk, *The Dielectric Function of III-V Semiconductors at High Temperatures*, PhD thesis, TU Berlin, 2005.

[13] D. E. Aspnes, J. P. Harbison, A. A. Studna, and L. T. Florez, *Reflectance-difference spectroscopy system for real-time measurements of crystal growth*, *Appl. Phys. Lett.* **52**, 957 (1988).

[14] D. E. Aspnes, J. P. Harbison, A. A. Studna, and L. T. Florez, *Application of reflectance difference spectroscopy to molecular-beam epitaxy of GaAs and AlAs*, *J. Vac. Sci. Technol. A* **6**, 1327 (1988).

[15] D. E. Aspnes and A. A. Studna, *Anisotropies in the Above-Band-Gap Optical Spectra of Cubic Semiconductors*, *Phys. Rev. Lett.* **54**, 1956 (1985).

[16] V. L. Berkovits, L. F. Ivantsov, V. A. Kiselev, I. V. Makarenko, T. A. Minashvili, and V. I. Safarov, *Polarization spectra of optical transitions at a clean GaAs (110) surface*, *JETP Lett.* **41**, 551 (1985).

[17] Edward D. Palik, editor, *Handbook of Optical Constants of Solids*, Academic Press, Inc., 1985.

[18] Manuel Cardona, F. H. Pollak, and K. L. Shaklee, *Electroreflectance in semiconductors*, In *J. Phys. Soc. Japan 215: Proceedings of the International Conference on the Physics of Semiconductors*, volume 215, page 89, 1966.

[19] R. M. A. Azzam, *PIE: perpendicular-incidence ellipsometry-application to the determination of the optical properties of uniaxial and biaxial absorbing crystals*, *Opt. Commun.* **19**, 122 (1976).

[20] R. M. A. Azzam, *Perpendicular-incidence photometric ellipsometry (PIPE) of surfaces with arbitrary anisotropy*, *J. Optics* **12**, 317 (1981).

[21] D. E. Aspnes, *Above-bandgap optical anisotropies in cubic semiconductors: A visible-near ultraviolet probe of surfaces*, *J. Vac. Sci. Technol. B* **3**, 1498 (1985).

[22] P. Weightman, D. S. Martin, R. J. Cole, and T. Farrell, *Reflection anisotropy spectroscopy*, *Rep. Prog. Phys.* **68**, 1251 (2005).

[23] Z. Sobiesierski, D. I. Westwood, and C. C. Matthai, *Aspects of reflectance anisotropy spectroscopy from semiconductor surfaces*, *J. Phys: Condens. Matter* **10**, 1 (1998).

[24] B. Drévillon, J. Y. Parey, M. Stchakovsky, R. Benferhat, Y. Josserand, and B. Schlayen, *Design of a new in situ spectroscopic phase modulated ellipsometer*, In *Multichamber and In-Situ Processing of Electronic Materials, Proc. SPIE*, volume 1188, pages 174–184, 1989.

[25] O. Acher and B. Drévillon, *A reflectance anisotropy spectrometer for real-time measurements*, *Rev. Sci. Instrum.* **63**, 5332 (1992).

[26] P. Harrison, T. Farrell, A. Maunder, C. I. Smith, and P. Weightman, *A rapid reflectance anisotropy spectrometer*, *Meas. Sci. Technol.* **12**, 2185 (2001).

[27] M. Zorn, J. Jönsson, W. Richter, J.-T. Zettler, and K. Ploska, *Anisotropic Reflectance from Semiconductor Surfaces for in-situ Monitoring in epitaxial growth systems*, *phys. stat. sol. (a)* **152**, 23 (1995).

[28] K. Ploska, J.-T. Zettler, W. Richter, J. Jönsson, F. Reinhardt, J. Rumberg, M. Pristovsek, M. Zorn, D. Westwood, and R. H. Williams, *Surface processes before and during growth of GaAs (001)*, *J. Cryst. Growth* **145**, 44 (1994).

[29] J.-T. Zettler, J. Rumberg, K. Ploska, K. Stahrenberg, M. Pristovsek, W. Richter, M. Wassermeier, P. Schützendübe, J. Behrend, and L. Däweritz, *Reflectance Anisotropy Oscillations during MOCVD and MBE Growth of GaAs(001), phys. stat. sol. (a)* **152**, 35 (1995).

[30] M. Pristovsek, M. Zorn, and M. Weyers, *In situ study of GaAs growth mechanisms using tri-methyl gallium and tri-ethyl gallium precursors in metal-organic vapour phase epitaxy*, *J. Cryst. Growth* **262**, 78 (2004).

[31] F. Reinhardt, J. Jönsson, M. Zorn, W. Richter, K. Ploska, J. Rumberg, and P. Kurpas, *Monolayer growth oscillations and surface structure of GaAs(001) during metalorganic vapor phase epitaxy growth*, *J. Vac. Sci. Technol. B* **12**, 2541 (1994).

[32] J. R. Creighton and K. C. Baucom, *Reflectance-difference spectroscopy of adsorbate-covered GaAs(001) surfaces: a combined surface science and in-situ OMVPE study*, *Surf. Sci.* **409**, 372 (1998).

[33] J. A. Gupta, S. P. Watkins, R. Arès, and G. Soerensen, *MOVPE growth of single monolayers of InAs in GaAs studied by time-resolved reflectance difference spectroscopy*, *J. Cryst. Growth* **195**, 205 (1998).

[34] A. I. Shkrebtii, N. Esser, W. Richter, W. G. Schmidt, F. Bechstedt, A. Kley, B. O. Fimland, and R. Del Sole, *Reflectance Anisotropy of GaAs(100): theory and experiment*, *Phys. Rev. Lett.* **81**, 721 (1998).

[35] Elisabeth Steimetz, *In-situ Wachstumsuntersuchungen zur selbstorganisierten Ausbildung von InAs-Quantenpunkten auf GaAs(001)-Oberflächen*, PhD thesis, TU Berlin, 2002.

[36] Elisabeth Steimetz, Wolfgang Richter, Frank Schienle, Daniel Fischer, Michael Klein, and Jörg-Thomas Zettler, *The Effect of Different Group V Precursors on the Evolution of Quantum Dots Monitored by Optical In Situ Measurements*, *Jpn. J. Appl. Phys.* **37**, 1483 (1998).

[37] M. Mutoh, N. Tsurumi, and H. Hasegawa, *Effects of initial surface reconstruction on silicon interface control layer based passivation of (001) GaAs surfaces studied in an ultrahigh-vacuum multichamber system*, *Jpn. J. Appl. Phys. Part 1* **38** (1999).

[38] Peter Y. Yu and Manuel Cardona, *Fundamentals of Semiconductors*, Springer Verlag, 2nd edition, 1999.

[39] Andreas Schneider, *In situ- und online-Raman-Spektroskopie zur Analyse von Halbleiterheterostrukturen aus ZnS_xSe_{1-x} und Gruppe-III-Nitriden*, PhD thesis, TU Chemnitz, 2000.

[40] S. E. Acosta-Ortiz and A. Lastras-Martínez, *Measurements of above-bandgap optical anisotropies in the (001) surface of GaAs*, *Solid State Comm.* **64**, 809 (1987).

[41] Rolf Enderlein and Andreas Schenk, *Grundlagen der Halbleiterphysik*, Akademie Verlag, Berlin, 1991.

[42] Donald A. Neamen, *Semiconductor Physics and Devices*, Irwin, 2nd edition, 1997.

[43] *New Semiconductor Materials - Characteristics and Properties*, URL http://www.ioffe.ru/SVA/.

[44] A. G. Milnes, *Deep Impurities in Semiconductors*, John Wiley and Sons, New York, 1973.

[45] M. I. Guseva, N. V. Zotova, A. V. Koval, and D. N. Nasledov, *Sov. Phys. Semicond.* **8**, 34 (1974).

[46] M. I. Guseva, N. V. Zotova, A. V. Koval, and D. N. Nasledov, *Sov. Phys. Semicond.* **8**, 1323 (1975).

[47] P. J. Dean, In J. McCaldin and G. Somorjai, editors, *Progress in Solid State Chemistry*, volume 8. Pergamon Press, New York, 1973.

[48] A. A. Kopylov and A. N. Pikhtin, *Solid State Comm.* **26**, 735 (1978).

[49] W. Mönch, *Chemisorption-induced Defects at Interfaces on Compound Semiconductors*, *Surf. Sci.* **132**, 92 (1983).

[50] Harald Ibach and Hans Lüth, *Festkörperphysik*, Springer Verlag Berlin, 2nd edition, 1988.

[51] D. S. Kyser and V. Rehn, *Piezoelectric effects in electroreflectance*, *Solid State Comm.* **8**, 1437 (1970).

[52] S. E. Acosta-Ortiz and A. Lastras-Martínez, *Electro-optic effects in the optical anisotropies of (001) GaAs*, *Phys. Rev. B* **40**, 1426 (1989).

[53] J. L. Shay, *Photoreflectance Line Shape at the Fundamental Edge in Ultrapure GaAs*, *Phys. Rev. B* **2**, 803 (1970).

[54] Ali Badakhshan, R. Glosser, and S. Lambert, *Correlation between the photoreflectance response at E_1 and carrier concentration in $n-$ and $p-$GaAs*, *J. Appl. Phys.* **69**, 2525 (1990).

[55] V. L. Berkovits, I. V. Makarenko, T. A. Minashvili, and V. I. Safarov, *Anisotropy of the optical reflection of cubic semiconductors due to surface band bending*, *Soviet Physics – Semiconductors* **20**, 654 (1986).

[56] H. Tanaka, E. Colas, I. Kamiya, D. E. Aspnes, and R. Bhat, *In situ determination of free-carrier concentrations by reflectance difference spectroscopy*, *Appl. Phys. Lett.* **59**, 3443 (1991).

[57] Y. H. Chen, Z. Yang, R. G. Li, Y. Q. Wang, and Z. G. Wang, *Reflectance-difference spectroscopy study of the Fermi-level position of low-temperature-grown GaAs*, *Phys. Rev. B* **55**, R7379 (1997).

[58] N. Kumagai, T. Yasuda, T. Hanada, and T. Yao, *In situ measurement of carrier concentration in n-ZnSe by reflectance difference spectroscopy (RDS)*, *J. Cryst. Growth* **214/215**, 547 (2000).

[59] Chen-Guo Jin, Tetsuji Yasuda, Kozo Kimura, Akihiro Ohtake, Li-Hsin Kuo, Tai-Hong Wang, Shiro Miwa, Takafumi Yao, and Kazunobu Tanaka, *Non-Contact and Non-Destructive Measurement of Carrier Concentration of Nitrogen-Doped ZnSe by Reflectance Difference Spectroscopy*, *Jpn. J. Appl. Phys.* **36**, 6638 (1997).

[60] Z. Sobiesierski, D. I. Westwood, and M. Elliott, *Reflectance anisotropy spectra from Si δ-doped GaAs(001): Correlation of linear electro-optic effect with integrated surface field*, *Phys. Rev. B* **56**, 15277 (1997).

[61] Udo Scherz, *Quantenmechanik*, Teubner Verlag, 1999.

[62] W. G. Schmidt, F. Bechstedt, W. Lu, and J. Bernholc, *Interplay of surface reconstruction and surface electric fields in the optical anisotropy of GaAs(001)*, *Phys. Rev. B* **66**, 085334 (2002).

[63] M. Pristovsek, S. Tsukamoto, B. Han, J.-T. Zettler, and W. Richter, *Influence of the reconstruction of GaAs (001) on the electro-optical bulk properties*, *J. Cryst. Growth* **248**, 254 (2003).

[64] Amnon Yariv, *Introduction to optical electronics*, Holt, Rinehart and Winston, 2nd edition, 1976.

[65] S. E. Acosta-Ortiz, *Above-band-gap linear electro-optic coefficients of GaAs*, *J. Appl. Phys.* **70**, 3239 (1991).

[66] W. R. Cook jr., D. F. Nelson, and K. Vedan, *Landolt-Börnstein: High Frequency Properties of Dielectric Crystals – Volume III/30, Subvolume A: Piezooptic and Electrooptic Coefficients and Nonlinear Dielectric Susceptibilities*, Springer Verlag, 1996.

[67] S. Casalbuoni, H. Schlarb, B. Schmidt, B. Steffen, P. Schmüser, and A. Winter, *Numerical Studies on the Electro-Optic Sampling of Relativistic Electron Bunches*, In *Proceedings of the Particle Accelerator Conference, Knoxville/USA*, 2005.

[68] Markus Pristovsek, S. Tsukamoto, N. Koguchi, Bing Han, Kolja Haberland, Jörg-Thomas Zettler, Wolfgang Richter, Martin Zorn, and Markus Weyers, *In-situ Determination of the Carrier Concentration of (001) GaAs by Reflectance Anisotropy Spectroscopy*, *phys. stat. sol. (a)* **188**, 1423 (2001).

[69] T.U. Kampen, U. Rossow, M. Schumann, S. Park, and D.R.T. Zahn, *Reflectance anisotropy spectroscopy of the growth of perylene-3,4,9,10-tetracarboxylic dianhydride on chalcogen passivated GaAs(001) surfaces*, *J. Vac. Sci. Technol. B* **18**, 2077 (2000).

[70] W. Chen, M. Dumas, D. Mao, and A. Kahn, *Work function, electron affinity, and band bending at decapped GaAs(100) surfaces*, *J. Vac. Sci. Technol. B* **10**, 1886 (1992).

[71] *AnalysR – Software for the analysis of ellipsometric and photometric thin-film measurements*, Laytec GmbH, 2002, URL http://www.laytec.de.

[72] A. Rebey, L. Béji, B. El Jani, and P. Gibart, *Optical monitoring of the growth rate reduction by CCl_4 during metalorganic vapour-phase epitaxy deposition of carbon doped GaAs*, *J. Cryst. Growth* **191**, 734 (1998).

[73] T. B. Joyce, T. J. Bullough, and T. Farrell, *Optical monitoring of the growth of heavily doped GaAs by chemical beam epitaxy and of the in situ etching of GaAs using CBr_4*, *Appl. Phys. Lett.* **65**, 2193 (1994).

[74] T. B. Joyce, T. J. Bullough, and S. P. Westwater, *In-situ monitoring of carbon doped GaAs and of periodic carbon doped GaAs/AlAs structures grown by chemical beam epitaxy*, *J. Cryst. Growth* **146**, 394 (1995).

[75] T. B. Joyce, S. P. Westwater, P. J. Goodhew, and R. E. Pritchard, *Growth of carbon-doped GaAs, AlGaAs and InGaAs by chemical beam epitaxy and the application of in-situ monitoring*, *J. Cryst. Growth* **164**, 371 (1996).

[76] K. Knorr, A. Rumberg, M. Zorn, C. Meyne, T. Trepk, J.-T. Zettler, W. Richter, P. Kurpas, and M. Weyers, *Real-time monitoring of P-based semiconductor growth by linear-optical spectroscopy*, In *Proceedings of 8th International Conference on Indium Phosphide and Related Materials*, pages 590–593. IEEE, New York, 1996.

[77] P. Kurpas, M. Sato, A. Knauer, and M. Weyers, *On-line growth monitoring of InP-based device structures by reflectance anisotropy spectroscopy*, *J. Electron. Mat.* **26**, 1154 (1997).

[78] M. Arens, P. Kurpas, P. Ressel, and M. Weyers, *Real-time growth monitoring of InGaAs/InP-HBT structures with reflectance anisotropy spectroscopy*, *Thin Solid Films* **313-314**, 609 (1998).

[79] Z. Hang, H. Shen, and F. H. Pollak, *Temperature dependence of the E_0 and $E_0 + \Delta_0$ gaps of InP up to 600° C*, *Solid State Comm.* **73**, 15 (1990).

[80] M. Zorn, T. Trepk, J.-T. Zettler, C. Meyne, K. Knorr, T. Wethkamp, W. Richter, B. Junno, M. Miller, and L. Samuelson, *On the temperature dependence of the InP(001) bulk and surface dielectric function*, In *Proceedings of 8th International Conference on Indium Phosphide and Related Materials*, pages 586–589. IEEE, New York, 1996.

[81] M. Zorn, T. Trepk, J.-T. Zettler, B. Junno, C. Meyne, K. Knorr, T. Wethkamp, M. Klein, M. Miller, W. Richter, and L. Samuelson, *Temperature dependence of the InP(001) bulk and surface dielectric function*, *Appl. Phys. A* **65**, 333 (1997).

[82] C. M. Herzinger, P. G. Snyder, B. Johs, and J. A. Woollam, *J. Appl. Phys.* **77**, 1715 (1995).

[83] M. Cardona, K. L. Shaklee, and F. H. Pollak, *Phys. Rev.* **154**, 696 (1967).

[84] N. Otsuka, M. Kito, M. Ishino, Y. Matsui, and F. Toujou, *Control of double diffusion front unintentionally penetrated from a Zn doped InP layer during metalorganic vapor phase epitaxy*, *J. Appl. Phys.* **84**, 4239 (1998).

[85] N. Otsuka, M. Kito, Y. Mori, M. Ishino, and Y. Matsui, *New structure by selective regrowth in multi-quantum well laser diodes performed by low pressure metalorganic vapor phase epitaxy*, *J. Cryst. Growth* **145**, 866 (1994).

[86] C. Blaauw, F. R. Shepherd, and D. Eger, *Secondary ion mass spectrometry and electrical characterization of Zn diffusion in n-type InP*, *J. Appl. Phys.* **66**, 605 (1989).

[87] Winfried Mönch, *Semiconductor Surfaces and Interfaces*, Springer Verlag Berlin, 2nd edition, 1995.

[88] C. D. Thurmond, G. P. Schwartz, G. W. Kammlott, and B. Schwartz, *GaAs Oxidation and the Ga-As-O Equilibrium Phase Diagram*, *J. Electrochem. Soc.* **127**, 1366 (1980).

[89] In Carl W. Wilmsen, editor, *Physics and Chemistry of III-V Compound Semiconductor Interfaces*. Plenum Press, New York, 1985.

[90] G. P. Schwartz, *Analysis of Native Oxide Films and Oxide-Substrate Reactions on III-V Semiconductors Using Thermochemical Phase Diagrams*, *Thin Solid Films* **103**, 3 (1983).

[91] G. P. Schwartz, W. A. Sunder, and J. E. Griffiths, *The In-P-O Phase Diagram: Construction and Applications*, *J. Electrochem. Soc.* **129**, 1361 (1982).

[92] D. E. Aspnes and A. A. Studna, *Dielectric functions and optical parameters of Si, Ge, GaP, GaAs, GaSb, InP, InAs, and InSb from 1.5 to 6.0 eV*, *Phys. Rev. B* **27**, 985 (1983).

[93] Stefan Zollner, *Model dielectric functions for native oxides on compound semiconductors*, *Appl. Phys. Lett.* **63**, 2523 (1993).

[94] *SOPRA n & k database with 278 materials*, URL `http://www.sopra-sa.com/fichiers/Database.zip`.

[95] David Stroud, *The effective medium approximations: Some recent developments*, *Superlattices and Microstructures* **23**, 567 (1998).

[96] D. A. G. Bruggeman, *Berechnung verschiedener physikalischer Konstanten von heterogenen Substanzen*, *Ann. Phys. (Leipzig)* **24**, 636 (1935).

[97] Martin Beerbom, *Hochaufgelöste Photoelektronenspektroskopie zur Untersuchung naßchemischer und elektrochemischer Prozeßschritte an GaAs-Oberflächen*, PhD thesis, TU Darmstadt, Shaker Verlag Aachen, 2002.

[98] V. L. Berkovits, A. B. Gordeeva, and V. A. Kosobukin, *Local-field effects in reflectance anisotropy spectra of oxidized (001) GaAs and AlGaAs surfaces*, *Surf. Sci.* **119**, 647 (2001).

[99] M. Passlack, J. K. Abrokwah, Z. Yu, R. Droopad, C. Overgaard, and H. Kawayoshi, *Thermally induced oxide crystallinity and interface destruction in Ga_2O_3–GaAs structures*, *Appl. Phys. Lett.* **82**, 1691 (2003).

[100] J. A. Van Vechten, *A simple man's view of the thermochemistry of semiconductors*, In T. S. Moss and S. P. Keller, editors, *Handbook on Semiconductors, Vol. 3: Materials, Properties and Preparation*. North-Holland Publishing Company, 1980.

[101] Christian Kaspari, Markus Pristovsek, and Wolfgang Richter, *A fast reflectance anisotropy spectrometer for in situ growth monitoring*, *phys. stat. sol. (b)* **242**, 2561 (2005).

[102] C. Meyne, M. Gensch, S. Peters, U. W. Pohl, J.-T. Zettler, and W. Richter, *In situ monitoring of ZnS/GaP and ZnSe/GaAs metalorganic vapor phase epitaxy using reflectance anisotropy spectroscopy and spectroscopic ellipsometry*, *Thin Solid Films* **364**, 12 (2000).

[103] D. A. Allwood, N. J. Mason, and P. J. Walker, *In situ characterisation of III-V substrate oxide desorption by surface photoabsorption in MOVPE*, *Materials Science and Engineering B* **66**, 83 (1999).

[104] F. Schröder, W. Storm, M. Altebockwinkel, L. Wiedmann, and A. Benninghoven, *Analysis of passivating oxide and surface contaminants on GaAs (100) by temperature-dependent and angle-resolved x-ray photoelectron spectroscopy, and time-of-flight secondary ion mass spectrometry*, *J. Vac. Sci. Technol. B* **10**, 1291 (1992).

[105] P. W. Atkins, *Physical Chemistry*, Oxford University Press, 3rd edition, 1986.

[106] G. P. Schwartz, C. D. Thurmond, G. W. Kammlott, and B. Schwartz, *Summary Abstract: GaAs Oxidation and the Ga-As-O Equilibrium Phase Diagram*, *J. Vac. Sci. Technol.* **17**, 958 (1980).

[107] S. W. McKnight, E. D. Palik, and T. N. Bhar, *Cathodoluminescence studies of anodic oxides on GaAs*, *J. Vac. Sci. Technol.* **17**, 967 (1980).

[108] P. J. Grunthaner, R. P. Vasquez, and F. J. Grunthaner, *Chemical depth profiles of the GaAs/native oxide interface*, *J. Vac. Sci. Technol.* **17**, 1045 (1980).

[109] O. Kubaschewski and E. U. Evans, *Metallurgical Thermodynamics, Vol. 1 of Series "Metal Physics and Phys. Metallurgy"*, Pergamon Press, New York, 1958.

[110] D. A. Allwood, R. T. Carline, N. J. Mason, C. Pickering, B. K. Tanner, and P. J. Walker, *Characterization of oxide layers on GaAs substrates*, *Thin Solid Films* **364**, 33 (2000).